Turning InP nanocrystals up to ^{11}:

Coinage Metal Cation Exchange in InP Nanocrystals

Forrest Walker Eagle

A dissertation

submitted in partial fulfillment of the

requirements for the degree of

Doctor of Philosophy

University of Washington

2024

Reading Committee:

Brandi Cossiart, Chair

Alexandra Velian

Dianne Xiao

Program Authorized to Offer Degree:

Chemistry

University of Washington

Abstract

Turning InP up to 11*:

Coinage Metal Cation Exchange in InP Nanocrystals

Forrest Walker Eagle

Chair of the Supervisory Committee:

Brandi Cossairt

Department of Chemistry

Cation exchange is a powerful method to expand the versatility and properties of a semiconductor nanocrystal. By tuning the amount of exogenous cation a spectrum of new materials can be accessed, including doped nanoparticles, alloyed nanocrystals, and even fully exchanged nanomaterials that may be challenging or impossible to create via traditional synthetic methods. This thesis focuses on the cation exchange of coinage metal (Cu, Ag, Au) cations in InP nanomaterials. Chapter 1 will provide an introduction to core concepts and background related to quantum dots, clusters, and dopant-dependent properties. In chapter 2, we will discuss the development of a new methodology to dope InP quantum dots with Cu^+ ions, and the effect that surface treatments have upon the photophysics of these Cu^+:InP nanocrystals. In chapter 3,

electron transfer to molecular acceptors from undoped and coinage metal (Cu, Ag) doped InP quantum dots is investigated, finding that the long lived photoexcited states imparted by doping QDs greatly enhance the likelihood of electron transfer. In chapter 4, coinage metals (Cu, Ag, Au) are exchanged into atomically precise $In_{37}P_{20}(O_2CC_{13}H_{27})_{51}$ magic sized clusters (MSCs). The exchange of cations in the InP lattice can be tuned either creating doped InP-MSCs, or driven to completion, creating coinage metal-phosphide clusters. These materials have distinct spectroscopic and structural characteristics, and can serve as precursors for forming larger nanoparticles, including previously unreported materials.

TABLE OF CONTENTS

LIST OF FIGURES

LIST OF TABLES

ACKNOWLEDGEMENTS

I want to acknowledge that to without a great many people, this could not be possible. I am a firm believer that you are an accumulation of the people around you and the people who have helped me become who I am today and accomplish what I have cannot be thanked enough.

To start, I have to thank my advisor, Brandi Cossairt. Without her guidance I would have truly been lost. Brandi has taught me so much over the last 5 years; more than just science, Brandi has shown me time and time again that the true key to success is to go above and beyond what others do – if you think that something is worth doing, you should do it to the best of your ability.

I also want to thank my committee members for their guidance. Alexandra, Julie, and Dianne for their impact on me as a scientist. I have always felt welcome at UW and I believe that a huge part of that is the great community of chemists that has been established by you all. I can speak to any of you at a conference and seminar and know that you will have valuable feedback and input for almost any project.

I would be remiss if I did not thank my lab mates. Michael Enright and Beth Mundy have my eternal gratitude for teaching how to be an inorganic chemist. As for 311: Samantha Harvey, you have become one of my closest collaborators, and often times the only sense of reason in the office. Soren and Grant, I cannot describe the liveliness you two brought back into lab, especially after COVID. Your positive attitudes and enthusiasm for chemistry were infectious and helped me push to the end.

I want to briefly thank some of my friends for always making my time in grad school always worthwhile.

Since day one Justin Pothoof has been in my corner – he is not only one of my very dearest friends but one of the best people I know. Justin has always been someone that I can chat science with, commiserate about failed experiments, or practice talks with. He also has been a constant companion whether getting coffee, trying restaurants, watching movies, going on spontaneous trips to Vancouver or our many nights spent at random dive bars in Seattle.

Christopher Yin has become one of my closest friends over the last 3 years. From activities as varied as trolling the ID for dumplings and watching movies to going to shows at Barbossa and moshing, Chris has been an amazing friend that is always down for an adventure. Chris has also been a fantastic backpacking buddy for those times that I have absolutely needed to leave Seattle for a short break, and I will always look fondly upon our wandering in the woods.

Doreen Fadaeiforghan and Lucas Wilson have been incredible friends, with all of us supporting each other through our graduate studies. I will always look forward to Sounders games with the squad, having long days at our pool that turn in to impromptu dinner parties, and commiserating about our lawyer wives.

Diego Novoa has been a good friend since undergrad and been a great source of support, especially during difficult times. Despite being separated by 750+ miles of the West Coast we have been able to see each other many times and he has been a fantastic support during grad school. Whether talking about music, going for hikes, or general hooligan activities, Deegs has always been there.

I want to thank my mentors during undergraduate studies, Professors Aimee Morris and Michael Grubb. You two showed me that the world of chemistry extended far beyond my wildest imagination. You both tolerated my many hours spent in your offices, constantly asking questions of "What about this? Or this?" and for that I will be forever grateful. Michael, you made me realize that chemistry and physics are the song that encompasses all creation and I'll always appreciate that.

I have to acknowledge that without the support of my family, I never would have found the drive to pursue a PhD. I want to thank my mother, my father, and my brothers for their constant support in following my dreams. I can never express how deeply grateful I am to each of them for all their encouragement and love despite the great distance between us. I must thank my grandmother, Fredette, and my aunt Tabitha, for their constant support and for inspiring my curiosity from a young age. The walks I took with the two of them in the woods of Viriginia inspired me to learn more about the world around me. Seeing them both so excited about the world around them and being so willing to teach about their corner of the world deeply influenced my great desire to always be learning.

However, the most influential person for these last 5 years has to be my wife, Valerie. You have been the greatest support that I have ever known. Without your patience and love I am certain that there would have been many times that I would have given up. You are so wildly brilliant, and I think you deserve an honorary PhD for listening to me practice my many talks throughout gradate school. On top of it all, you managed to graduate from law school before me – you are truly so incredible and I am so grateful that I get to support and be supported by you.

Finally, Kiwi, I'm grateful to have had you to practice to when no one else was awake. Taking you for walks always helped me sort through complex thoughts and think of new things while you sniffed about.

DEDICATION

I dedicate this thesis to my wife Valerie.

1 INTRODUCTION

1.1 A BRIEF INTRODUCTION TO COLLOIDAL NANOCRYSTALS AND CLUSTERS

Colloidal nanocrystals are ordered materials with one dimension being less than 100 nanometers that are accessed and processed in solution. Although colloidal nanocrystals have been used since antiquity,[1] research on nanoparticles has exploded in recent decades, with tens of thousands of research articles published yearly.[2] We will continue to focus on a specific subclass of colloidal nanoparticles, semiconductors, also known as quantum dots (QDs). These quantum dots have been used in myriad applications, including solar energy,[3] catalysis,[4–6] medical imaging,[7,8] and display technologies.[9,10]

While the larger nanoparticles have some degree of heterogeneity to them, molecular-like analogues known as magic sized clusters have also been isolated.[11] These species are not only atomically precise, but they also serve as important intermediates in the synthesis of many larger quantum dots or nanoparticles.[12,13] While these smaller analogues have drastically different optical and electronic properties from their larger counterparts, their inherent monodispersity makes them powerful platforms for studying many structural and mechanistic aspects of colloidal nanocrystal chemistry, such as cation exchange induced transformations[14,15] or surface-ligand interactions.[16,17]

1.2 CATION EXCHANGE AND DOPING IN SEMICONDUCTOR NANOCRYSTALS

The intentional doping of semiconductors with impurity atoms is a versatile strategy to access novel properties at the heart of modern optoelectronics and microelectronics. Similar to

bulk systems, semiconducting nanocrystals can also be doped, inducing new properties. Classically, doping in semiconductors is generally considered p or n type, with the addition of extra holes or electrons, respectively. However, for other materials, such as phosphors and scintillators, atoms (often rare earth elements) can be added in low concentrations to sensitize materials for desired luminescent properties. In nanocrystals, doping can be thought of as a partial cation exchange reaction; a processes in which some or all of original metal cations are replaced with a different metal cation. These doping procedures not only allow for control of over the nanocrystal's electronic properties, similar to bulk semiconductor systems, but often time lead to new optical properties, similar to materials specifically sensitized for luminescent features.

Nanostructures are an especially promising platform for cation exchange reactions due to their ultrasmall crystallite sizes. Due to these sizes, the surface area is much larger than in traditional bulk materials, allowing for a higher concentration of sites that cations can diffuse in the lattice. Due to the small size of the nanocrystals most metals can diffuse through the entire lattice, rather than being concentrated at a layer ranging up to a few nanometers below the surface.[18] Additionally, due the to the ligand stabilization of colloidal nanoparticles, a multitude of ligands can used to tune the intensity of cation exchange via hard-soft acid-base (HSAB) principles.[19–21] The cation exchange process can be broken into two main components, a thermodynamic portion, and a kinetic portion. The thermodynamic portion of these reactions covers factors such as association and dissociation energies, solvation and desolvation energies, and hard-soft acid-base (HSAB) predictions. These factors influence the *identity* of the cation exchange products and reactants – what cations can reasonably be predicted to replace others in an existing lattice, with tabulated values for a wide range having been calculated.[22]

On the other hand, kinetic factors mostly focus upon the mechanisms and structural conversion by which cation exchange occurs, such as solid-state diffusion via vacancies and solid state diffusion via interstitials. These factors influence the *rate* of the cation exchange process, which in turn influences the resultant structure of the material. This can be especially important in species with hindered kinetic factors (such as mismatch of initial and final lattices), potentially leading to nanoparticles with only partial cation exchange occurring.[23] Of particular curiosity, is that nanoscale materials can also have cooperative cation exchange reactions. In these reactions cation exchange does not occur via a constant replacement of cations, but instead reaches critical doping concentration and then rapidly uptakes a large amount of added cation and rapidly transforms to the product.[24–27]

The synthetic versatility of cation exchange has not only lead to the development of a range of doped materials,[28–31] but can be pushed to the formation of alloyed materials,[32–35] complex heterostructures,[36–40] and even metastable materials.[41–45] A brief visual summary of the cation exchange reaction landscape is provided below in **Figure 1.1**.

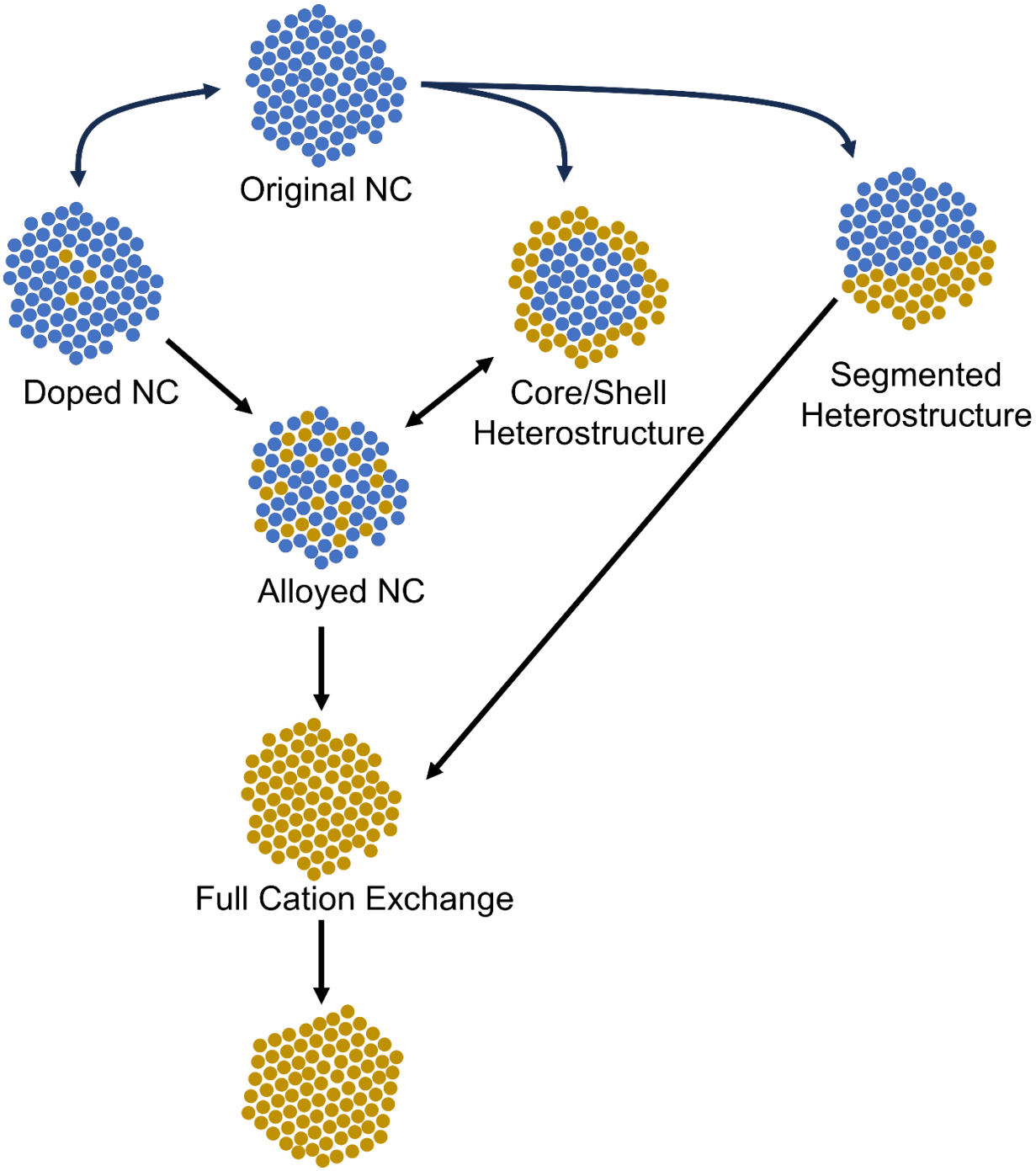

Figure 1.1. Cartoon schematic of the complex reaction landscape of cation exchange reactions of nanocrystals.

1.3 Coinage metal Dopant induced properties and Photophysics

1.3.1 Luminescent Properties of coinage metal doped quantum dots

Upon the introduction of dopants, multiple new properties can arise in the doped nanocrystals. Perhaps the most common reason for doping a quantum dot is to introduce new luminescent properties. In undoped materials, photoexcitation generates a bound electron-hole pair known as an exciton. This exciton may relax to the ground state either non-radiatively or via electron-hole recombination, leading to the generation of a band-edge photon (Figure 1.2A). However, when dopants are introduced into the semiconductor, new electronic states in the material's band gap are introduced, in turn leading to new optical properties. Perhaps the best examples of these are dopants such as Cu, Mn, and the lanthanide series (Figure 1.2B-D, respectively).[28,46] We will continue to focus on Cu and to a lesser extent, Ag, dopants.

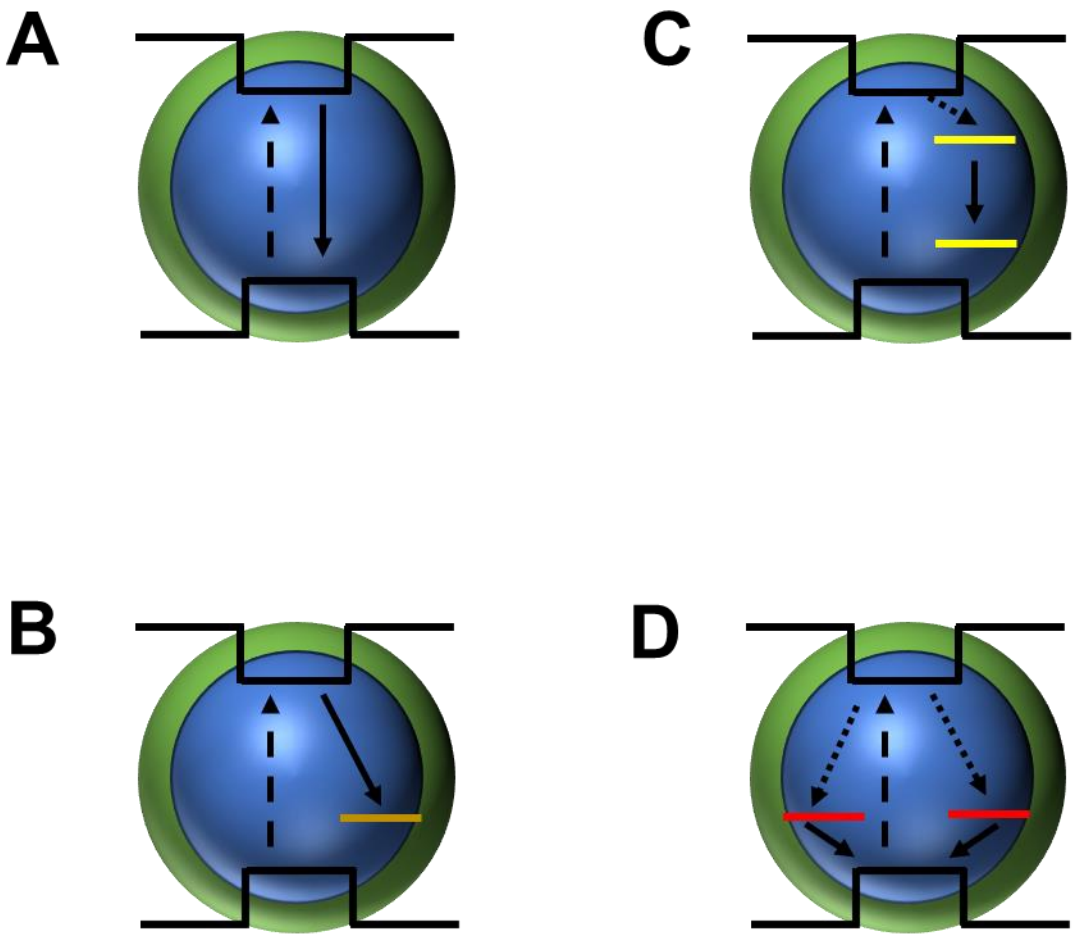

Figure 1.2. Cartoon schematic of the excitation (dashed arrow) and band edge luminescence (solid arrow) of undoped quantum dots. B) Cartoon schematic of the excitation (dashed arrow) and $ML_{CB}CT$ emission of Cu^{+} doped quantum dots. C)) Cartoon schematic of the excitation (dashed arrow), followed by transfer to a Mn^{2+} dopant (dotted arrow) and Mn2+ emission (solid arrow). D) Cartoon schematic of the excitation (dashed arrow) followed by tranfer to a Yb^{3+} dopant (dotted arrow) and Yb^{3+} emission (solid arrow).

When Cu^{+} is introduced into semiconducting materials a new mid-gap state is also introduced. The energy level of the Cu^{+} dopant is pinned to vacuum, making the new doped emission readily tunable by tuning the size of the starting nanocrystal.[47] Upon photoexcitation,

the electron is again promoted to the conduction band; however, now the hole rapidly localizes to the Cu^{+} dopant forming a Cu^{2+} state known as the metal-to-ligand (conduction band) charge transfer excited state ($ML_{CB}CT$).[48,49] This rapid localization leads to a distortion of the lattice and a reduction in the wavefunction overlap of the electron and now Cu-bound hole. This in turn leads to an increase in the charge separated state, easily observed by transient photoluminescence or absorption studies, as well as a broad luminescence profile.

Similar to Cu^{+} doped materials, Ag^{+} doped materials can have a broad, highly Stokes-shifted luminescent feature as well as shown in **Figure 1.2A**.[50,51] However, unlike copper doped materials, the mid-gap state introduced by silver dopants is lower in energy, leading to a photoluminescence feature that is blue shifted in comparison to copper induced PL. Additionally, photoexcitation leads to hole trapping that is more delocalized, in turn leading to shorter excited state lifetimes (Figure 1.2B).[50,52,53]

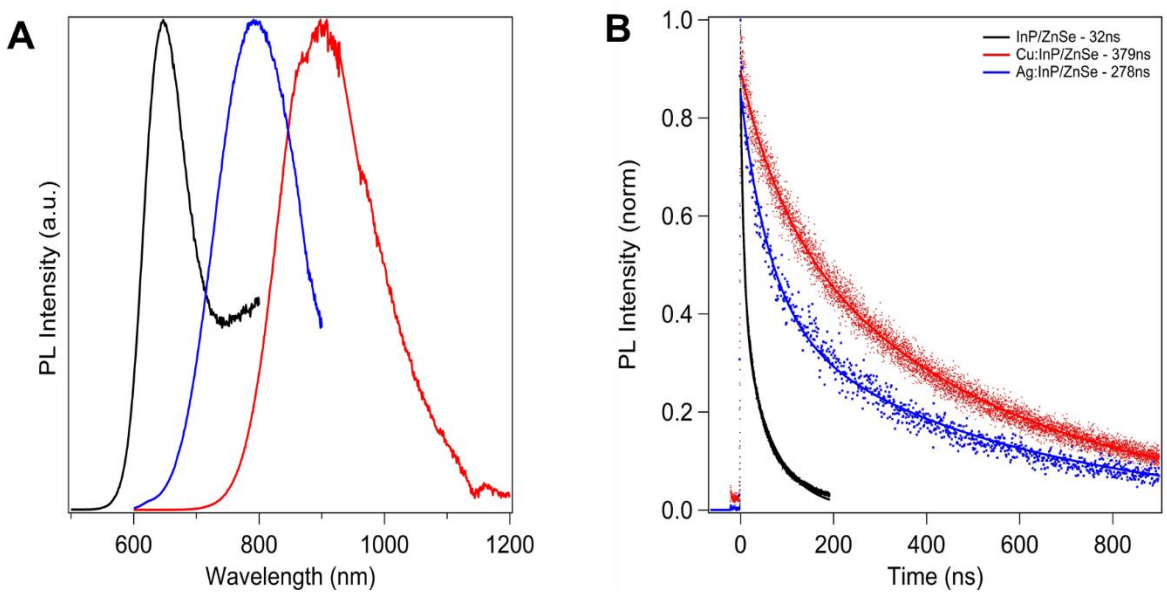

Figure 1.3. A) Example photoluminescence for InP/ZnSe (black), Ag^{+}:InP/ZnSe(blue) and Cu^{+}:InP/ZnSe (red) quantum dots. B) Time resolved photoluminescence decay of InP/ZnSe (black), Ag^{+}:InP/ZnSe(blue) and Cu^{+}:InP/ZnSe (red) quantum dots.

While these dopants serve as engineered defect states, the photoluminescence quantum yield, a measure of how emissive these materials are, is often low. This is due to the competition of other trap states, such as undercoordinated surface ions, potentially trapping the long lived excited electron, in turn leading to high amounts nonradiative recombination. This can be addressed however, by typical surface treatments that remove native surface traps.[54,55] Upon the introduction of a thin shell of ZnS onto Cu^+:ZnSe quantum dots, the PLQY of the $ML_{CB}CT$ increases significantly.[56] Similar effects were found for the inverted core/shell system of Cu^+:ZnSe/CdSe as well as for Cu:InP/ZnSe quantum dots.[57,58]

While Peng et al. were the first to demonstrate the synthesis of Cu:InP/ZnSe nanocrystals, the impact of various surface treatments was not considered and a holistic picture of the charge carrier processes was not developed. We will examine the impact of various surface treatments on Cu^+:InP quantum dots in chapter 1.

1.3.2 Charge Transfer in Doped QDs

Understanding the photophysical properties of quantum dots has implications that extend beyond photoluminescence. As quantum dots are semiconductors, there is great interest in utilizing the photogenerated charge carriers for a variety of processes that require charge extraction, such as solar cells and photocatalysis. As previously mentioned, introduction of a coinage metal dopant in a quantum dot drastically impacts the photophysical properties, shifting the luminescence profile due to the $ML_{CB}CT$ recombination. Due to the new spatial separation of the photogenerated charge carriers, the lifetimes of these luminescent features increase drastically, with dopants such as Cu^+ and Ag^+ increasing the lifetime by an order of magnitude

from ten of nanosecond to hundreds of nanoseconds. As such, they allow for greater charge extraction and thus enhanced activity.

Cu^+ doped quantum dots have recently been utilized as enhanced photocatalytic systems, showing enhanced activity for hydrogen evolution compared to undoped quantum dots, although these systems dope Cu^+ into the shell rather than the core.[59,60] Additionally, Cu^+ doped quantum dots have been shown to enhance photovoltaic performance compared to undoped quantum dot based solar cells.[61]

Chapter 3 outlines our efforts to further explain the effect that coinage metal doping has on charge transfer to a series of molecular acceptors.

1.4 Cation Exchange in Magic Sized Clusters

While cation exchange in bulk and nanocrystalline materials has been widely studied, control of the concentration and location of induced defects have remained elusive. Additionally, while many attempts have been made to fully characterize the mechanism by which cation exchange occurs, no general schema has been established, in part due to the large degree of heterogeneity found in nanoparticle ensembles. Magic sized clusters (MSCs) can serve as excellent platforms to study mechanism and physical effects induced by cation exchange as they do not suffer polydispersity.

As nanoscience has grown, a large focus on II-VI materials has led to the in depth investigation of II-VI magic sized clusters. The most common dopants for II-VI clusters are Mn^{2+} and Co^{2+} due to the unique magnetic features introduced upon introduction of the impurity ion.[62–64] However full cation exchange has also been explored in II-VI magic sized clusters with notable emphasis upon exchanges involving two Group 12 metals. Prominent examples of this include conversion of ZnX species to CdX species (X = S, Se, Te), as well as conversion of

CdSe to HgSe clusters.[65,66] However, more exotic cation exchanges have been performed, exchanging Cd with Cu^+ to form Cu_2Se clusters.[14] These new clusters exhibit highly interesting properties, such as super-ionicity, attributed to their ultrasmall size and strain.[67] This research has been further expounded in recent years by the Robinson group, studying the exchange of Cu^+ and Ag^+ in CdS MSCs, creating Cu_2S and Ag_2S clusters.[27]

In contrast with the wide collection on II-VI magic sized clusters, only three previous reports have examined cation exchange in InP MSC and no studies have examined other III-V clusters. The pioneering study by Stein et al. focused on the full cation exchange of In^{3+} to Cd^{2+}, specifically monitoring the transformation of the InP cluster to a Cd_3P_2 species.[15] Their findings indicated topotactic cation exchange of the surface indium upon small additions of cadmium carboxylate. With higher concentrations of Cd^{2+} cation, the Cd^{2+} then was introduced into the core, creating an alloyed structure, followed by full conversion with high excess of Cd^{2+} introduced.

Following this study, Friedfeld et al., focused upon attempting to introduce Zn^{2+} and Ga^{3+} dopants into the MSC lattice.[68] The results of this study found that incorporation of Ga^{3+} was difficult and that incorporating large amounts of Zn^{2+} lead to a drastic loss in crystallinity of the MSC. Furthermore, attempting to use these doped clusters as single source precursors did not result in alloyed quantum dots but rather Zn^{2+} and Ga^{3+} ions bound to the surfaces of InP quantum dots. Zn^{2+} doped clusters were further investigated by Kwon et al. and were found to undergo a conversion from a molecular like species to one that exhibited more quantum dot like properties.[69] The initial introduction of zinc does not greatly change the lattice of the MSC; however, upon heating the MSC undergoes significant structural rearrangement.

We will continue to build on studies of cation exchange in InP MSCs in chapter 4, demonstrating the conversion of InP MSC to a series of coinage metal phosphides and the products resulting from thermolysis of these new cluster species to access novel phosphide phases.

1.5 References

(1) Montanarella, F.; Kovalenko, M. V. Three Millennia of Nanocrystals. *ACS Nano* **2022**, *16* (4), 5085–5102. https://doi.org/10.1021/acsnano.1c11159.

(2) Zhu, H.; Jiang, S.; Chen, H.; Roco, M. C. International Perspective on Nanotechnology Papers, Patents, and NSF Awards (2000–2016). *J Nanopart Res* **2017**, *19* (11), 370. https://doi.org/10.1007/s11051-017-4056-7.

(3) Kamat, P. V. Quantum Dot Solar Cells. The Next Big Thing in Photovoltaics. *J. Phys. Chem. Lett.* **2013**, *4* (6), 908–918. https://doi.org/10.1021/jz400052e.

(4) Yuan, Y.; Jin, N.; Saghy, P.; Dube, L.; Zhu, H.; Chen, O. Quantum Dot Photocatalysts for Organic Transformations. *J. Phys. Chem. Lett.* **2021**, *12* (30), 7180–7193. https://doi.org/10.1021/acs.jpclett.1c01717.

(5) Weiss, E. A. Designing the Surfaces of Semiconductor Quantum Dots for Colloidal Photocatalysis. *ACS Energy Lett.* **2017**, *2* (5), 1005–1013. https://doi.org/10.1021/acsenergylett.7b00061.

(6) Su, H.; Wang, W.; Shi, R.; Tang, H.; Sun, L.; Wang, L.; Liu, Q.; Zhang, T. Recent Advances in Quantum Dot Catalysts for Hydrogen Evolution: Synthesis, Characterization, and Photocatalytic Application. *Carbon Energy* **2023**, *5* (9), e280. https://doi.org/10.1002/cey2.280.

(7) Michalet, X.; Pinaud, F. F.; Bentolila, L. A.; Tsay, J. M.; Doose, S.; Li, J. J.; Sundaresan, G.; Wu, A. M.; Gambhir, S. S.; Weiss, S. Quantum Dots for Live Cells, in Vivo Imaging, and Diagnostics. *Science* **2005**, *307* (5709), 538–544. https://doi.org/10.1126/science.1104274.

(8) Medintz, I. L.; Uyeda, H. T.; Goldman, E. R.; Mattoussi, H. Quantum Dot Bioconjugates for Imaging, Labelling and Sensing. *Nature Mater* **2005**, *4* (6), 435–446. https://doi.org/10.1038/nmat1390.

(9) Bourzac, K. Quantum Dots Go on Display. *Nature* **2013**, *493* (7432), 283–283. https://doi.org/10.1038/493283a.

(10) Moon, H.; Lee, C.; Lee, W.; Kim, J.; Chae, H. Stability of Quantum Dots, Quantum Dot Films, and Quantum Dot Light-Emitting Diodes for Display Applications. *Advanced Materials* **2019**, *31* (34), 1804294. https://doi.org/10.1002/adma.201804294.

(11) Busatto, S.; de Mello Donega, C. Magic-Size Semiconductor Nanostructures: Where Does the Magic Come From? *ACS Mater. Au* **2022**, *2* (3), 237–249. https://doi.org/10.1021/acsmaterialsau.1c00075.

(12) Gary, D. C.; Terban, M. W.; Billinge, S. J. L.; Cossairt, B. M. Two-Step Nucleation and Growth of InP Quantum Dots via Magic-Sized Cluster Intermediates. *Chemistry of Materials* **2015**, *27* (4), 1432–1441. https://doi.org/10.1021/acs.chemmater.5b00286.

(13) Qiao, L.; Pollard, N.; Senanayake, R. D.; Yang, Z.; Kim, M.; Ali, A. S.; Hoang, M. T.; Yao, N.; Han, Y.; Hernandez, R.; Clayborne, A. Z.; Jones, M. R. Atomically Precise Nanoclusters Predominantly Seed Gold Nanoparticle Syntheses. *Nat Commun* **2023**, *14* (1), 4408. https://doi.org/10.1038/s41467-023-40016-3.

(14) White, S. L.; Banerjee, P.; Chakraborty, I.; Jain, P. K. Ion Exchange Transformation of Magic-Sized Clusters. *Chem. Mater.* **2016**, *28* (22), 8391–8398. https://doi.org/10.1021/acs.chemmater.6b03882.

(15) Stein, J. L.; Steimle, M. I.; Terban, M. W.; Petrone, A.; Billinge, S. J. L.; Li, X.; Cossairt, B. M. Cation Exchange Induced Transformation of InP Magic-Sized Clusters. *Chem. Mater.* **2017**, *29* (18), 7984–7992. https://doi.org/10.1021/acs.chemmater.7b03075.

(16) Nevers, D. R.; Williamson, C. B.; Hanrath, T.; Robinson, R. D. Surface Chemistry of Cadmium Sulfide Magic-Sized Clusters: A Window into Ligand-Nanoparticle Interactions. *Chem. Commun.* **2017**, *53* (19), 2866–2869. https://doi.org/10.1039/C6CC09549F.

(17) Ritchhart, A.; Cossairt, B. M. Quantifying Ligand Exchange on InP Using an Atomically Precise Cluster Platform. *Inorg. Chem.* **2019**, *58* (4), 2840–2847. https://doi.org/10.1021/acs.inorgchem.8b03524.

(18) Fisher, D. J. Diffusion in GaAs and Other III-V Semiconductors. 286.

(19) Gui, J.; Ji, M.; Liu, J.; Xu, M.; Zhang, J.; Zhu, H. Phosphine-Initiated Cation Exchange for Precisely Tailoring Composition and Properties of Semiconductor Nanostructures: Old Concept, New Applications. *Angewandte Chemie International Edition* **2015**, *54* (12), 3683–3687. https://doi.org/10.1002/anie.201410053.

(20) Lee, D.; Kim, W. D.; Lee, S.; Bae, W. K.; Lee, S.; Lee, D. C. Direct Cd-to-Pb Exchange of CdSe Nanorods into PbSe/CdSe Axial Heterojunction Nanorods. *Chem. Mater.* **2015**, *27* (15), 5295–5304. https://doi.org/10.1021/acs.chemmater.5b01548.

(21) Jeong, S.; Han, J. H.; Jang, J.; Seo, J.; Kim, J.-G.; Cheon, J. Transformative Two-Dimensional Layered Nanocrystals. *J. Am. Chem. Soc.* **2011**, *133* (37), 14500–14503. https://doi.org/10.1021/ja2049594.

(22) Beberwyck, B. J.; Surendranath, Y.; Alivisatos, A. P. Cation Exchange: A Versatile Tool for Nanomaterials Synthesis. *J. Phys. Chem. C* **2013**, *117* (39), 19759–19770. https://doi.org/10.1021/jp405989z.

(23) Gupta, S.; Kershaw, S. V.; Susha, A. S.; Wong, T. L.; Higashimine, K.; Maenosono, S.; Rogach, A. L. Near-Infrared-Emitting CdxHg1−xSe Nanorods Fabricated by Ion Exchange in an Aqueous Medium. *ChemPhysChem* **2013**, *14* (12), 2853–2858. https://doi.org/10.1002/cphc.201300084.

(24) Routzahn, A. L.; Jain, P. K. Single-Nanocrystal Reaction Trajectories Reveal Sharp Cooperative Transitions. *Nano Lett.* **2014**, *14* (2), 987–992. https://doi.org/10.1021/nl4044289.

(25) White, S. L.; Smith, J. G.; Behl, M.; Jain, P. K. Co-Operativity in a Nanocrystalline Solid-State Transition. *Nat Commun* **2013**, *4* (1), 2933. https://doi.org/10.1038/ncomms3933.

(26) Routzahn, A. L.; Jain, P. K. Luminescence Blinking of a Reacting Quantum Dot. *Nano Lett.* **2015**, *15* (4), 2504–2509. https://doi.org/10.1021/acs.nanolett.5b00068.

(27) Yao, Y.; Lynch, R.; Robinson, R. D. Mass Spectroscopy Study of the Intermediate Magic-Size Cluster Species during Cooperative Cation Exchange. *The Journal of Chemical Physics* **2023**, *159* (1), 014704. https://doi.org/10.1063/5.0151904.

(28) Knowles, K. E.; Hartstein, K. H.; Kilburn, T. B.; Marchioro, A.; Nelson, H. D.; Whitham, P. J.; Gamelin, D. R. Luminescent Colloidal Semiconductor Nanocrystals Containing Copper: Synthesis, Photophysics, and Applications. *Chem. Rev.* **2016**, *116* (18), 10820–10851. https://doi.org/10.1021/acs.chemrev.6b00048.

(29) Sahu, A.; Kang, M. S.; Kompch, A.; Notthoff, C.; Wills, A. W.; Deng, D.; Winterer, M.; Frisbie, C. D.; Norris, D. J. Electronic Impurity Doping in CdSe Nanocrystals. *Nano Lett.* **2012**, *12* (5), 2587–2594. https://doi.org/10.1021/nl300880g.

(30) Martín-Rodríguez, R.; Geitenbeek, R.; Meijerink, A. Incorporation and Luminescence of Yb3+ in CdSe Nanocrystals. *J. Am. Chem. Soc.* **2013**, *135* (37), 13668–13671. https://doi.org/10.1021/ja4077414.

(31) Wu, P.; Yan, X.-P. Doped Quantum Dots for Chemo/Biosensing and Bioimaging. *Chem. Soc. Rev.* **2013**, *42* (12), 5489–5521. https://doi.org/10.1039/C3CS60017C.

(32) Lesnyak, V.; George, C.; Genovese, A.; Prato, M.; Casu, A.; Ayyappan, S.; Scarpellini, A.; Manna, L. Alloyed Copper Chalcogenide Nanoplatelets via Partial Cation Exchange Reactions. *ACS Nano* **2014**, *8* (8), 8407–8418. https://doi.org/10.1021/nn502906z.

(33) Smith, A. M.; Nie, S. Bright and Compact Alloyed Quantum Dots with Broadly Tunable Near-Infrared Absorption and Fluorescence Spectra through Mercury Cation Exchange. *J. Am. Chem. Soc.* **2011**, *133* (1), 24–26. https://doi.org/10.1021/ja108482a.

(34) Gan, X. Y.; Sen, R.; Millstone, J. E. Connecting Cation Exchange and Metal Deposition Outcomes via Hume–Rothery-Like Design Rules Using Copper Selenide Nanoparticles. *J. Am. Chem. Soc.* **2021**, *143* (21), 8137–8144. https://doi.org/10.1021/jacs.1c02765.

(35) Groeneveld, E.; van Berkum, S.; van Schooneveld, M. M.; Gloter, A.; Meeldijk, J. D.; van den Heuvel, D. J.; Gerritsen, H. C.; de Mello Donega, C. Highly Luminescent (Zn,Cd)Te/CdSe Colloidal

Heteronanowires with Tunable Electron–Hole Overlap. *Nano Lett.* **2012**, *12* (2), 749–757. https://doi.org/10.1021/nl203695m.

(36) Khalavka, Y.; Harms, S.; Henkel, A.; Strozyk, M.; Ahijado-Guzmán, R.; Sönnichsen, C. Synthesis of Au–CdS@CdSe Hybrid Nanoparticles with a Highly Reactive Gold Domain. *Langmuir* **2018**, *34* (1), 187–190. https://doi.org/10.1021/acs.langmuir.7b02756.

(37) Miszta, K.; Gariano, G.; Brescia, R.; Marras, S.; De Donato, F.; Ghosh, S.; De Trizio, L.; Manna, L. Selective Cation Exchange in the Core Region of Cu2–xSe/Cu2–xS Core/Shell Nanocrystals. *J. Am. Chem. Soc.* **2015**, *137* (38), 12195–12198. https://doi.org/10.1021/jacs.5b06379.

(38) Sytnyk, M.; Kirchschlager, R.; Bodnarchuk, M. I.; Primetzhofer, D.; Kriegner, D.; Enser, H.; Stangl, J.; Bauer, P.; Voith, M.; Hassel, A. W.; Krumeich, F.; Ludwig, F.; Meingast, A.; Kothleitner, G.; Kovalenko, M. V.; Heiss, W. Tuning the Magnetic Properties of Metal Oxide Nanocrystal Heterostructures by Cation Exchange. *Nano Lett.* **2013**, *13* (2), 586–593. https://doi.org/10.1021/nl304115r.

(39) Li, M.; Yu, X.-F.; Liang, S.; Peng, X.-N.; Yang, Z.-J.; Wang, Y.-L.; Wang, Q.-Q. Synthesis of Au–CdS Core–Shell Hetero-Nanorods with Efficient Exciton–Plasmon Interactions. *Advanced Functional Materials* **2011**, *21* (10), 1788–1794. https://doi.org/10.1002/adfm.201002233.

(40) Zhang, J.; Tang, Y.; Lee, K.; Ouyang, M. Nonepitaxial Growth of Hybrid Core-Shell Nanostructures with Large Lattice Mismatches. *Science* **2010**, *327* (5973), 1634–1638. https://doi.org/10.1126/science.1184769.

(41) Stone, D.; Koley, S.; Remennik, S.; Asor, L.; Panfil, Y. E.; Naor, T.; Banin, U. Luminescent Anisotropic Wurtzite InP Nanocrystals. *Nano Lett.* **2021**, *21* (23), 10032–10039. https://doi.org/10.1021/acs.nanolett.1c03719.

(42) Shan, X.; Li, B.; Ji, B. Synthesis of Wurtzite In and Ga Phosphide Quantum Dots Through Cation Exchange Reactions. *Chem. Mater.* **2021**, *33* (13), 5223–5232. https://doi.org/10.1021/acs.chemmater.1c01287.

(43) Beberwyck, B. J.; Alivisatos, A. P. Ion Exchange Synthesis of III–V Nanocrystals. *J. Am. Chem. Soc.* **2012**, *134* (49), 19977–19980. https://doi.org/10.1021/ja309416c.

(44) Li, H.; Zanella, M.; Genovese, A.; Povia, M.; Falqui, A.; Giannini, C.; Manna, L. Sequential Cation Exchange in Nanocrystals: Preservation of Crystal Phase and Formation of Metastable Phases. *Nano Lett.* **2011**, *11* (11), 4964–4970. https://doi.org/10.1021/nl202927a.

(45) Powell, A. E.; Hodges, J. M.; Schaak, R. E. Preserving Both Anion and Cation Sublattice Features during a Nanocrystal Cation-Exchange Reaction: Synthesis of Metastable Wurtzite-Type CoS and MnS. *J. Am. Chem. Soc.* **2016**, *138* (2), 471–474. https://doi.org/10.1021/jacs.5b10624.

(46) Sreenan, B.; Lee, B.; Wan, L.; Zeng, R.; Zhao, J.; Zhu, X. Review of Mn-Doped Semiconductor Nanocrystals for Time-Resolved Luminescence Biosensing/Imaging. *ACS Appl. Nano Mater.* **2022**, *5* (12), 17413–17435. https://doi.org/10.1021/acsanm.2c04337.

(47) Grandhi, G. K.; Tomar, R.; Viswanatha, R. Study of Surface and Bulk Electronic Structure of II–VI Semiconductor Nanocrystals Using Cu as a Nanosensor. *ACS Nano* **2012**, *6* (11), 9751–9763. https://doi.org/10.1021/nn304149s.

(48) Prins, P. T.; Spruijt, D. A. W.; Mangnus, M. J. J.; Rabouw, F. T.; Vanmaekelbergh, D.; de Mello Donega, C.; Geiregat, P. Slow Hole Localization and Fast Electron Cooling in Cu-Doped InP/ZnSe Quantum Dots. *J. Phys. Chem. Lett.* **2022**, *13* (42), 9950–9956. https://doi.org/10.1021/acs.jpclett.2c02764.

(49) Wang, L.; Chen, Z.; Liang, G.; Li, Y.; Lai, R.; Ding, T.; Wu, K. Observation of a Phonon Bottleneck in Copper-Doped Colloidal Quantum Dots. *Nat Commun* **2019**, *10* (1), 4532. https://doi.org/10.1038/s41467-019-12558-y.

(50) Nelson, H. D.; Hinterding, S. O. M.; Fainblat, R.; Creutz, S. E.; Li, X.; Gamelin, D. R. Mid-Gap States and Normal vs Inverted Bonding in Luminescent Cu+- and Ag+-Doped CdSe Nanocrystals. *J. Am. Chem. Soc.* **2017**, *139* (18), 6411–6421. https://doi.org/10.1021/jacs.7b01924.

(51) Vinokurov, A.; Chernysheva, G.; Mordvinova, N.; Dorofeev, S. Optical Properties and Structure of Ag-Doped InP Quantum Dots Prepared by a Phosphine Synthetic Route. *Dalton Trans.* **2018**, *47* (35), 12414–12419. https://doi.org/10.1039/C8DT02434K.

(52) Stroyuk, O.; Raevskaya, A.; Gaponik, N.; Selyshchev, O.; Dzhagan, V.; Schulze, S.; Zahn, D. R. T. Origin of the Broadband Photoluminescence of Pristine and Cu+/Ag+-Doped Ultrasmall CdS and CdSe/CdS Quantum Dots. *J. Phys. Chem. C* **2018**, *122* (18), 10267–10277. https://doi.org/10.1021/acs.jpcc.8b02337.

(53) Eagle, F. W.; Harvey, S.; Beck, R.; Li, X.; Gamelin, D. R.; Cossairt, B. M. Enhanced Charge Transfer from Coinage Metal Doped InP Quantum Dots. *ACS Nanosci. Au* **2023**. https://doi.org/10.1021/acsnanoscienceau.3c00029.

(54) Stein, J. L.; Mader, E. A.; Cossairt, B. M. Luminescent InP Quantum Dots with Tunable Emission by Post-Synthetic Modification with Lewis Acids. *The Journal of Physical Chemistry Letters* **2016**, *7* (7), 1315–1320. https://doi.org/10.1021/acs.jpclett.6b00177.

(55) Hughes, K. E.; Stein, J. L.; Friedfeld, M. R.; Cossairt, B. M.; Gamelin, D. R. Effects of Surface Chemistry on the Photophysics of Colloidal InP Nanocrystals. *ACS Nano* **2019**, *13* (12), 14198–14207. https://doi.org/10.1021/acsnano.9b07027.

(56) Cooper, J. K.; Gul, S.; Lindley, S. A.; Yano, J.; Zhang, J. Z. Tunable Photoluminescent Core/Shell Cu+-Doped ZnSe/ZnS Quantum Dots Codoped with Al3+, Ga3+, or In3+. *ACS Appl. Mater. Interfaces* **2015**, *7* (18), 10055–10066. https://doi.org/10.1021/acsami.5b02860.

(57) Viswanatha, R.; Brovelli, S.; Pandey, A.; Crooker, S. A.; Klimov, V. I. Copper-Doped Inverted Core/Shell Nanocrystals with "Permanent" Optically Active Holes. *Nano Lett.* **2011**, *11* (11), 4753–4758. https://doi.org/10.1021/nl202572c.

(58) Xie, R.; Peng, X. Synthesis of Cu-Doped InP Nanocrystals (d-Dots) with ZnSe Diffusion Barrier as Efficient and Color-Tunable NIR Emitters. *J. Am. Chem. Soc.* **2009**, *131* (30), 10645–10651. https://doi.org/10.1021/ja903558r.

(59) Bang, J.; Das, S.; Yu, E.-J.; Kim, K.; Lim, H.; Kim, S.; Hong, J. W. Controlled Photoinduced Electron Transfer from InP/ZnS Quantum Dots through Cu Doping: A New Prototype for the Visible-Light

Photocatalytic Hydrogen Evolution Reaction. *Nano Lett.* **2020**, *20* (9), 6263–6271. https://doi.org/10.1021/acs.nanolett.0c00983.

(60) Zhao, H.; Li, X.; Cai, M.; Liu, C.; You, Y.; Wang, R.; Channa, A. I.; Lin, F.; Huo, D.; Xu, G.; Tong, X.; Wang, Z. M. Role of Copper Doping in Heavy Metal-Free InP/ZnSe Core/Shell Quantum Dots for Highly Efficient and Stable Photoelectrochemical Cell. *Advanced Energy Materials* **2021**, *11* (31), 2101230. https://doi.org/10.1002/aenm.202101230.

(61) Muthalif, M. P. A.; Lee, Y.-S.; Sunesh, C. D.; Kim, H.-J.; Choe, Y. Enhanced Photovoltaic Performance of Quantum Dot-Sensitized Solar Cells with a Progressive Reduction of Recombination Using Cu-Doped CdS Quantum Dots. *Applied Surface Science* **2017**, *396*, 582–589. https://doi.org/10.1016/j.apsusc.2016.10.200.

(62) Yang, J.; Fainblat, R.; Kwon, S. G.; Muckel, F.; Yu, J. H.; Terlinden, H.; Kim, B. H.; Iavarone, D.; Choi, M. K.; Kim, I. Y.; Park, I.; Hong, H.-K.; Lee, J.; Son, J. S.; Lee, Z.; Kang, K.; Hwang, S.-J.; Bacher, G.; Hyeon, T. Route to the Smallest Doped Semiconductor: Mn2+-Doped (CdSe)13 Clusters. *J. Am. Chem. Soc.* **2015**, *137* (40), 12776–12779. https://doi.org/10.1021/jacs.5b07888.

(63) Muckel, F.; Yang, J.; Lorenz, S.; Baek, W.; Chang, H.; Hyeon, T.; Bacher, G.; Fainblat, R. Digital Doping in Magic-Sized CdSe Clusters. *ACS Nano* **2016**, *10* (7), 7135–7141. https://doi.org/10.1021/acsnano.6b03348.

(64) Yang, J.; Muckel, F.; Choi, B. K.; Lorenz, S.; Kim, I. Y.; Ackermann, J.; Chang, H.; Czerney, T.; Kale, V. S.; Hwang, S.-J.; Bacher, G.; Hyeon, T. Co2+-Doping of Magic-Sized CdSe Clusters: Structural Insights via Ligand Field Transitions. *Nano Lett.* **2018**, *18* (11), 7350–7357. https://doi.org/10.1021/acs.nanolett.8b03627.

(65) He, L.; Luan, C.; Liu, S.; Chen, M.; Rowell, N.; Wang, Z.; Li, Y.; Zhang, C.; Lu, J.; Zhang, M.; Liang, B.; Yu, K. Transformations of Magic-Size Clusters via Precursor Compound Cation Exchange at Room Temperature. *J. Am. Chem. Soc.* **2022**, *144* (41), 19060–19069. https://doi.org/10.1021/jacs.2c07972.

(66) Antanovich, A.; Prudnikau, A.; Gurin, V.; Artemyev, M. Cd/Hg Cationic Substitution in Magic-Sized CdSe Clusters: Optical Characterization and Theoretical Studies. *Chemical Physics* **2015**, *455*, 32–40. https://doi.org/10.1016/j.chemphys.2015.04.004.

(67) White, S. L.; Banerjee, P.; Jain, P. K. Liquid-like Cationic Sub-Lattice in Copper Selenide Clusters. *Nat Commun* **2017**, *8* (1), 14514. https://doi.org/10.1038/ncomms14514.

(68) Friedfeld, M. R.; Stein, J. L.; Johnson, D. A.; Park, N.; Henry, N. A.; Enright, M. J.; Mocatta, D.; Cossairt, B. M. Effects of Zn2+ and Ga3+ Doping on the Quantum Yield of Cluster-Derived InP Quantum Dots. *J. Chem. Phys.* **2019**, *151* (19), 194702. https://doi.org/10.1063/1.5126971.

(69) Kwon, Y.; Oh, J.; Lee, E.; Lee, S. H.; Agnes, A.; Bang, G.; Kim, J.; Kim, D.; Kim, S. Evolution from Unimolecular to Colloidal-Quantum-Dot-like Character in Chlorine or Zinc Incorporated InP Magic Size Clusters. *Nat Commun* **2020**, *11* (1), 3127. https://doi.org/10.1038/s41467-020-16855-9.

2 SYNTHESIS AND SPECTROSCOPY OF EMISSIVE, SURFACE MODIFIED, COPPER-DOPED, INDIUM PHOSPHIDE NANOCRYSTALS

Significant portions of this chapter have been published by and thus adapted from:

M. Elizabeth Mundy, Forrest W. Eagle, Kira E. Hughes, Daniel R. Gamelin, and Brandi M. Cossairt. *ACS Materials Letters*, **2020**, 2, 6, 576-581

Note for collaborative work: The interpretation of time resolved photoluminescence and transient absorption spectroscopy was assisted by Kira Hughes, under the guidance of Professor Daniel

Gamelin. Synthetic methodology was guided by M. Elizabeth Mundy, under the guidance of Professor Brandi Cossairt.

2.1 INTRODUCTION

Semiconductor nanocrystals (NCs), or quantum dots, have been of great fundamental interest over the past few decades because of their solution processability and size, shape, and composition tunability. These features also make them attractive for commercial applications, including displays, lighting, photovoltaics, and biological sensing.[1–4] Copper-doped NCs, however, have captured recent attention because they exhibit Stokes-shifted emission and long photoluminescence (PL) lifetimes, properties that reflect copper's presence as a dopant in the NC lattice.[5–11] These features are particularly attractive for the design of near-infrared emitters for use in luminescent solar concentrators because of the NCs' low reabsorption and the advantageous location of the copper-based PL relative to the band gap of traditional silicon photovoltaics.[12,13] The PL in copper-doped semiconductors is attributed to localization of photogenerated valence-band holes at the Cu^{+} dopants following interband photoexcitation, formally forming Cu^{2+} in a luminescent mid-gap charge-transfer (CT) excited state.[5,14] The nuclear reorganization associated with hole localization gives the copper-based PL its characteristic broad line width, and the CT nature of the excited state contributes to its long lifetime.

Understanding charge-carrier traps is fundamental to developing the highly luminescent materials needed for a range of semiconductor technologies, including displays and photovoltaics. To be industrially relevant, NCs must have high PL quantum yields (PLQYs) and

narrow PL line widths. Although cadmium selenide (CdSe) NCs with near-unity PLQYs have been obtained and are now fundamentally well-understood, synthesizing NCs of non-toxic alternatives (e.g., III–V materials) that possess similar physical properties has proven challenging.[15] Indium phosphide (InP) NCs are an exciting and commercially proven alternative to cadmium-based materials, given their inherently lower toxicity and similar optical properties.[16,17] Recent developments in InP NC syntheses have separately produced ensembles that are monodisperse and highly photo- and electroluminescent, albeit with broader PL line widths than their CdSe analogues.[18–20] Despite these advances, the underlying principles governing the increase in PLQY are still under question. Various literature reports highlight the passivation of electron or hole traps, but the extent to which each trapping mechanism impacts the PL of InP NCs is debated.[21–23]

Using copper as an "engineered" hole trap offers a unique opportunity to examine carrier dynamics in NCs that is complementary to the study of undoped NCs. By preparing Cu^{+}:InP NCs, we can analyze the charge-carrier dynamics as a function of different post-synthetic surface treatments and correlate increases in PLQY with reduction in surface carrier trapping. Copper can be incorporated into the InP NCs either through a bottom-up method during synthesis or via a post-synthetic cation exchange reaction. The copper-doped cores can then be treated with Lewis acids, specifically zinc carboxylate, to increase the PLQYs using a method pioneered by our lab, while maintaining dopant incorporation.[24,25] Similar to prior literature reports, shelling the doped cores proved challenging because of copper migration from the NCs under traditional shelling conditions.[6] However, we were able to post-synthetically incorporate copper into thinly shelled InP/ZnSe NCs, inspired by an approach used for doping of CdSe/CdS NCs.[14] All of the samples were then spectroscopically probed utilizing time-resolved photoluminescence

spectroscopy (TRPL) to study the recombination dynamics of the conduction-band electron and copper-localized hole.

Aminophosphines have recently generated interest as relatively environmentally benign phosphorus sources for the synthesis of a range of metal phosphide NCs.[26–31] Changing the identity of the indium and cadmium halide precursors, for example, produces size-tunable InP or Cd_3P_2 NCs.[27,30] Given the previously established reactivity of aminophosphines with transition metals, we hypothesized that this system may provide an excellent synthetic platform for generating doped InP NCs. Prior experiments in our lab showed the formation of crystalline Cu_3P platelets from $CuCl_2$ and tris(diethylamino)phosphine as shown in **Figure 2.1**.

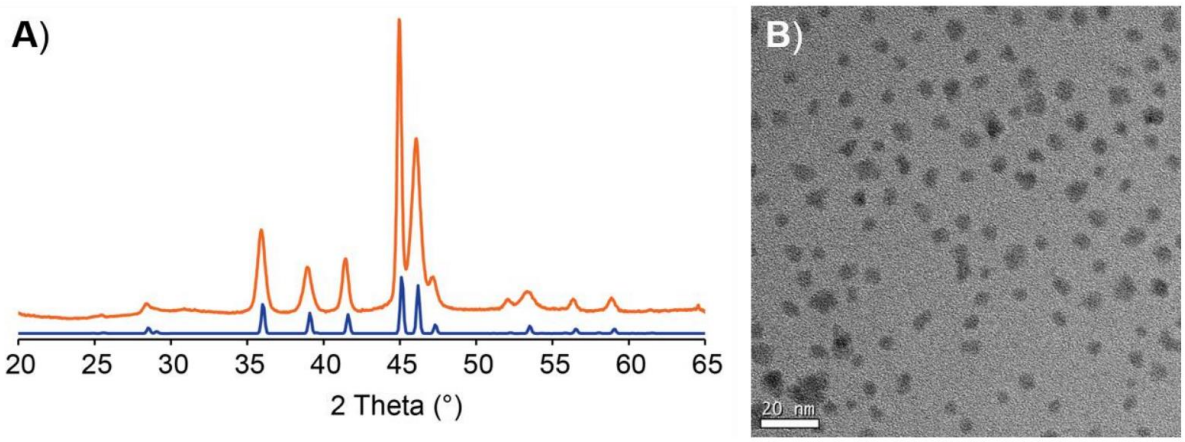

Figure 2.1 (A) P-XRD of reaction of PNEt and CuCl2 (orange) with the Cu3P standard pattern (blue). (B) TEM of resultant copper phosphide.

Although this result indicated the amenability of the system to the formation of Cu–P bonds, it also presented a challenge of preventing preferential formation of separate crystalline phases of Cu_3P and InP. This was recently seen under synthetic conditions where the presence of copper diverted significant amounts of phosphorus and allowed the formation of small InP NCs.[32] Although other reports gave no indication of the formation of Cu_3P under doping conditions, we

found that this impurity persisted when the aminophosphine was injected into a solution containing both the indium and copper halides.[33,34] To circumvent this detrimental reactivity, we delayed the introduction of the copper halide by 5 min to allow the InP to nucleate. Operationally, we used a syringe pump to add a solution of copper chloride in oleylamine over 30 minutes. The dropwise addition also maintained a relatively low concentration of copper to prevent monomers from reaching a critical concentration and separately nucleating Cu_3P.

2.2 Synthesis of Cu:InP via an aminophosphine route

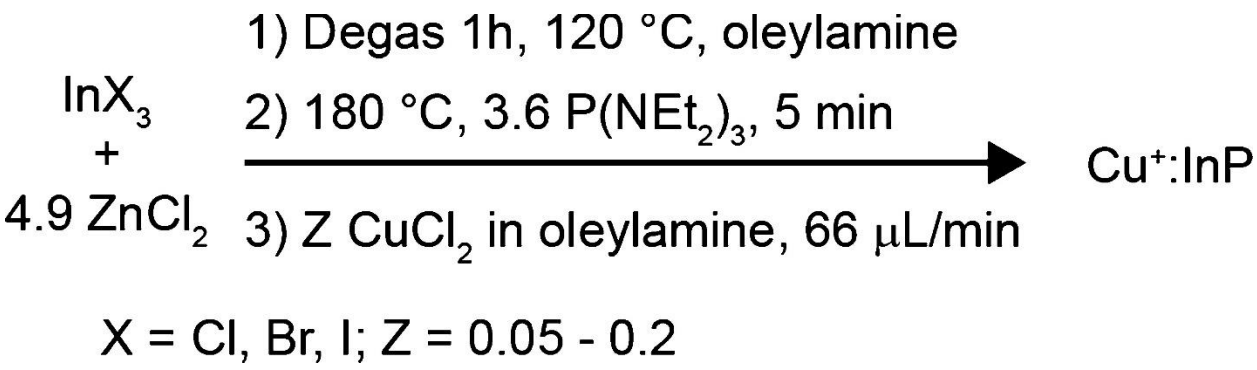

Figure 2.2. Synthetic scheme for the synthesis of Cu doped InP nanocrystals

With our procedure established (**Figure 2.2**), we successfully synthesized Cu^+:InP NCs. As shown in **Figure 2.3**A, the NCs synthesized with Z = 0.2 equivalents of copper and $InCl_3$ exhibit the characteristic tetrahedral morphology and 3.2 nm diameter associated with aminophosphine-derived InP NCs. The powder X-ray diffraction pattern (**Figure 2.3B**) is consistent with InP as the sole crystalline phase, and inductively coupled plasma optical emission spectroscopy (ICP-OES) confirmed the presence of copper in the NCs. The optical spectra strongly support copper doping (**Figure 2.3C**).

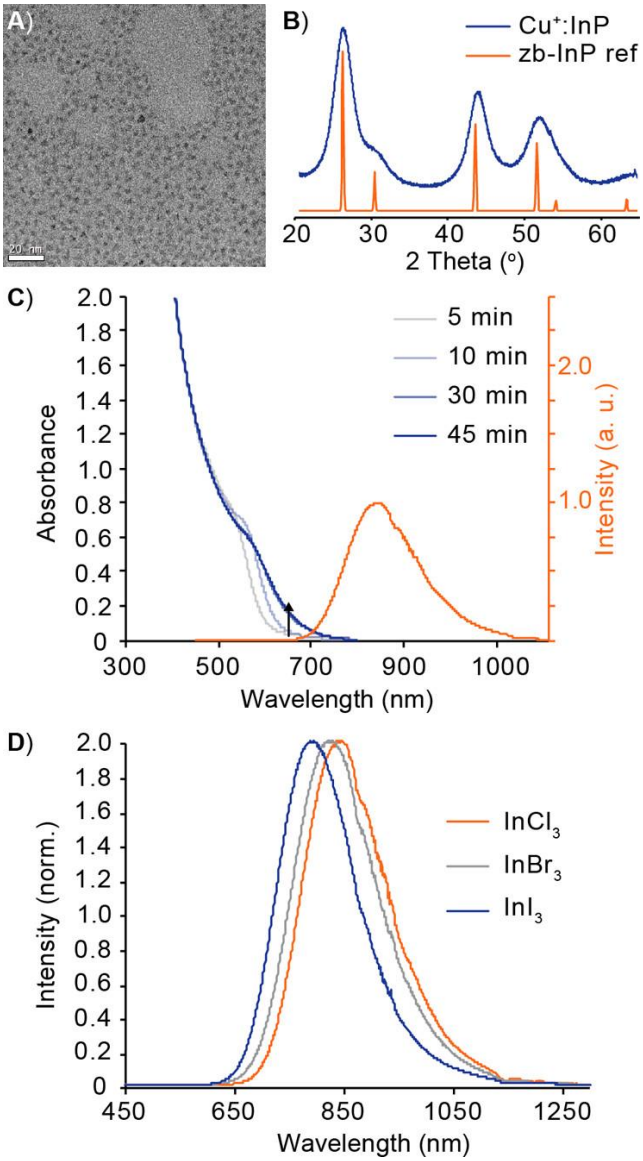

Figure 2.3. (A) TEM image of Cu^+:InP NCs derived from aminophosphines and $InCl_3$ showing d = 3.2 ± 0.3 nm NCs. (B) Powder X-ray diffraction pattern of the same NCs showing the only crystalline phase present to be InP. (C) UV–vis absorption spectra of reaction progress and final steady-state PL spectrum of a representative synthesis of Cu^+:InP NCs (10% PLQY). (D) Normalized steady-state PL spectra of copper-doped InP NCs synthesized with different halide precursors to tune the size of the NCs and the resulting $ML_{CB}CT$ emission energy.

Addition of copper results in the appearance of a broad red-shifted PL band with its maximum at ~850 nm and the emergence of weak near-band-edge absorption at ~650 nm that has been attributed to direct photoexcitation of the luminescent CT excited state.[35] Photoluminescence excitation (PLE) measurements monitoring the emission at 825 nm showed that the NIR emission arises from NC photoexcitation (**Figure 2.4**).

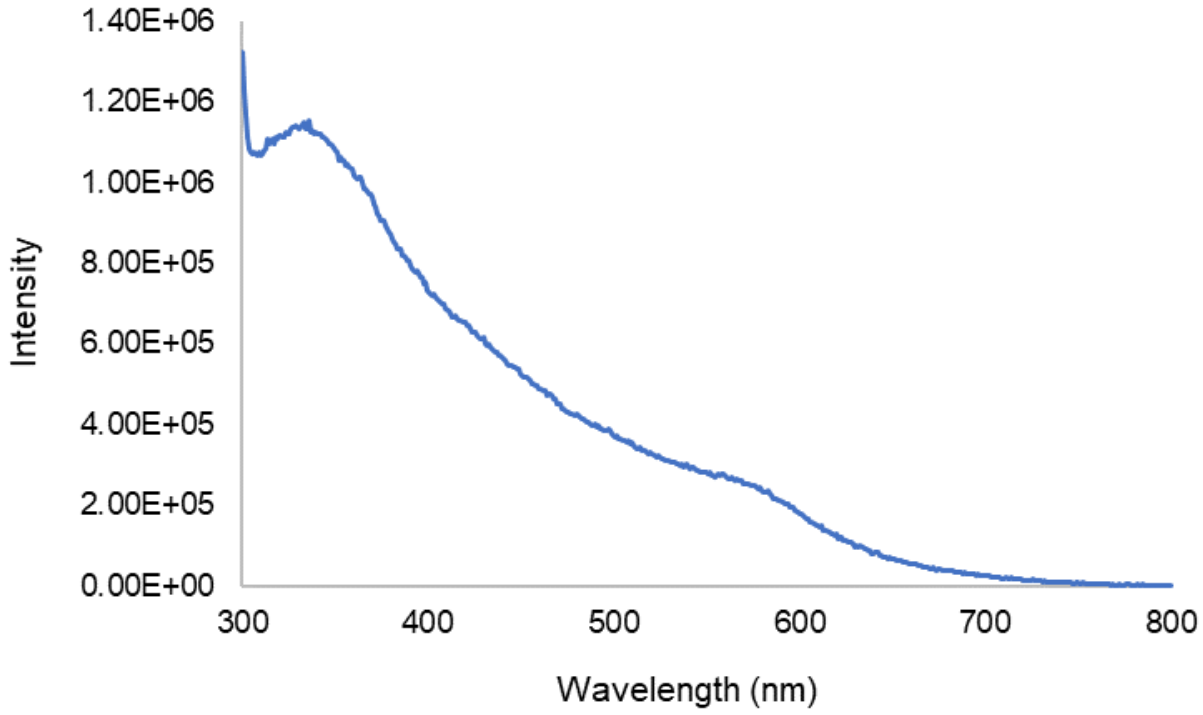

Figure 2.4. Photoluminescence excitation of Cu:InP monitored at 825 nanometers.

Together, these data constitute strong support for the incorporation of copper ions into the NC lattice. These NCs exhibit high PLQYs directly out of synthesis, ranging from 8 to 25%. We found that the PLQY decreases when the reaction scale is increased, likely as a result of variations in the heating profile that lead to less uninform copper incorporation.

We investigated the tunability of this reaction with regard to NC size and amount of copper incorporated. By alteration of the amount of copper added to the reaction (Z in Scheme

1), the In:Cu ratio in the final products could be modestly tuned (**Table 2.1**). We found that the upper limit was an In:Cu ratio of 17:1 (5.6% replacement of In), achieved with a starting In:Cu ratio of 10:1 or 20:1 in the reaction mixture. This NC doping level corresponds to incorporation of approximately 12 copper atoms per NC. When the starting In:Cu ratio was changed to 40:1, the corresponding In:Cu ratio was decreased to 33:1, corresponding to six copper atoms per nanocrystal. Higher levels of copper incorporation could be attained by changing the copper source to the more reactive copper (II) bromide, which gave an In:Cu ratio of 4:1 while maintaining the InP crystal phase. However, this synthesis did not result in an increased PLQY or a dramatic shift in the PL peak position, which may suggest the presence of significant surface-bound copper.

Table 2.1: ICP-OES elemental ratios of Cu doped nanocrystals formed under varying synthetic conditions.

Sample	Indium	Phosphorus	Copper	Zinc (Cadmium)	Selenium
$InCl_3$ 10:1 In:Cu	1.2	1	0.07		
$InCl_3$ 20:1 In:Cu	1.3	1	0.08		
$InCl_3$ 40:1 In:Cu	1.2	1	0.04		
$InBr_3$	1	1	0.1		
InI_3	1	1	0.13		
Zinc Treated	1	1	0.07	0.8	
Cadmium treated	1	1	0.05	(0.7)	
Thin Shelled	1.3	1	0.1	0.2	0.8
$CuBr_2$	1	1	0.25		

The NC size could be tuned by following established literature procedures for aminophosphine-derived InP NCs.[27] By replacing $InCl_3$ with either $InBr_3$ or InI_3 as the indium source and utilizing our standard slow-injection procedure, we also synthesized 3.0 and 2.8 nm diameter Cu^+:InP NCs with PLQYs of 15% and 18%, respectively. These changes in size were accompanied by a corresponding blue shift in the copper PL peak for the smaller NCs, as can be seen in **Figure 2.3D**. Our data agree with prior reports of the tunability of both the copper PL and host NC size.[6] The size changes were accompanied by increases in the level of copper incorporation, which could be attributed to increased reactivity of the copper precursor due to partial ligand scrambling at elevated temperatures.[36,37]

2.3 Surface treatments of Cu:InP

An advantage of Cu^+:InP NCs as a material for photophysical studies is the localization of the hole at the copper.[5] Recent work by our group has posited that both hole trapping and electron trapping are present and account for the typically low PLQY of as-synthesized InP NCs.[21] It is hypothesized that the electron traps can be addressed by exchanging undercoordinated indium atoms at the surface via treatment with lower-valent Lewis acids, specifically for M^{2+} carboxylates.

Despite prior reports of moderate copper stability within InP NCs, excitonic PL re-emerged under traditional shelling and Lewis acid treatment conditions, signaling copper loss from a subset of NCs (**Figure 2.5A-B**). This instability necessitated the use of a lower temperature, 100 °C compared to 200 °C, for the Lewis acid treatment with zinc stearate. At 100 °C, treatment with zinc carboxylate maintains the In:Cu ratio as determined by ICP (**Table 2.1**)

while inducing an increase in PLQY from 10% to 20% for Cu^{+}:InP/Zn NCs with no evidence of excitonic luminescence (**Figure 2.5C**).

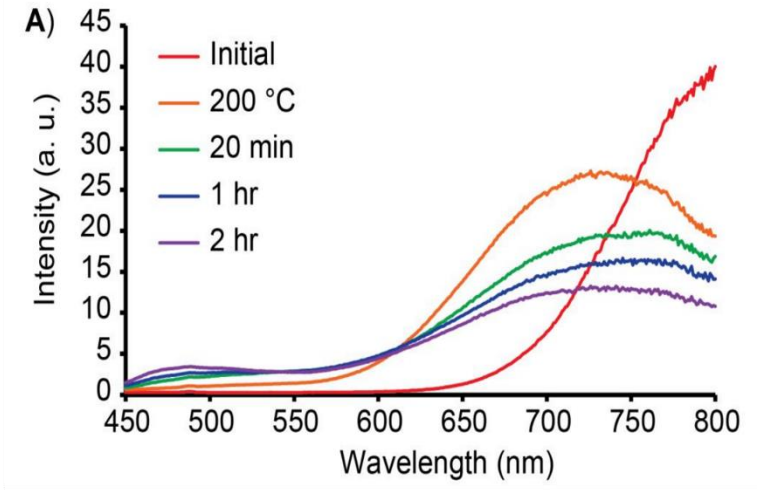

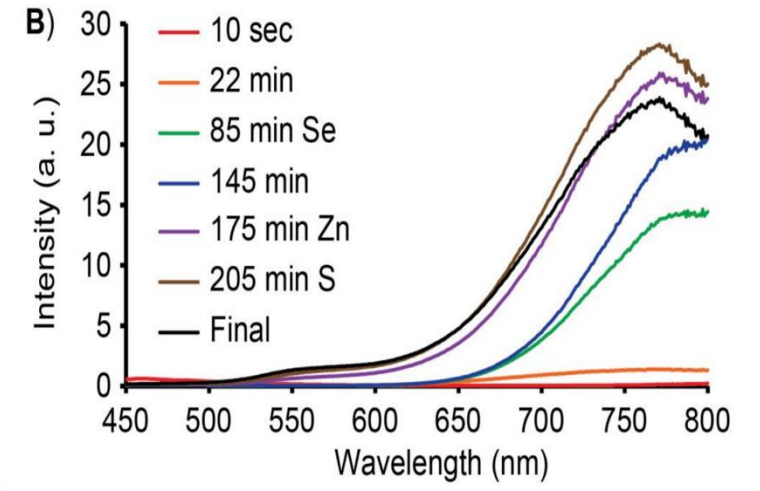

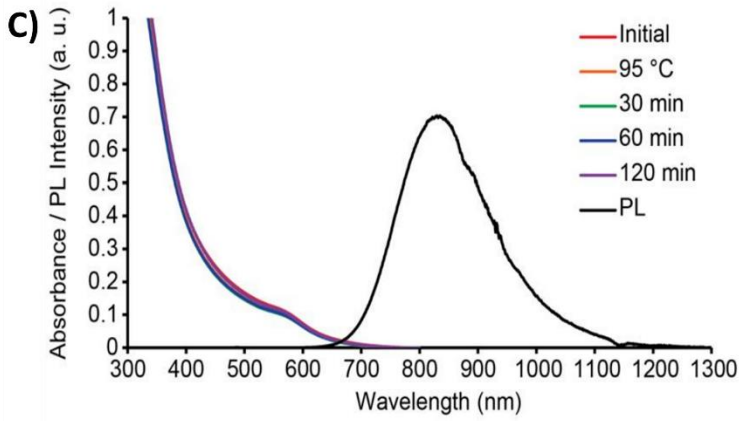

Figure 2.5. A) Photoluminescence of Cu:InP treated with zinc stearate at 200 °C. B) Photoluminescence of Cu:InP treated using a ZnSeS shelling procedure. C) UV-Vis and PL of a Cu:InP treated with zinc stearate at 100 °C.

The standard aminophosphine reaction contains an excess of zinc in the nucleation pot, which has been shown to increase the monodispersity of the final NCs and likely creates a zinc-rich surface that facilitates shell growth.[29,31] However, the treatment that we perform with the zinc carboxylates clearly alters the surface chemistry and passivates defects in a way the zinc halides cannot.

Prior reports have shown that cadmium carboxylates strongly interact with the InP surface and are highly successful agents for passivating electron traps.[21,24] In this study, we found that cadmium treatment is incompatible with the doped materials; at temperatures high enough for PLQY enhancement, we observed that the dopant leaves the NCs, as confirmed by PL and ICP analysis (**Figure 2.6**A-B). This might be due to alloying of cadmium into the surface, disrupting the lattice and accelerating copper loss.[24,38]

Shelling of previously doped NCs resulted in partial migration of copper from the lattice under a range of conditions, as reported in the literature.[27,34] Such samples demonstrated extremely high PLQYs, over 60% for the copper peak alone, but the presence of both doped and undoped NC populations in the sample limited their usefulness for spectroscopic study (**Figure 2.6C-D**).

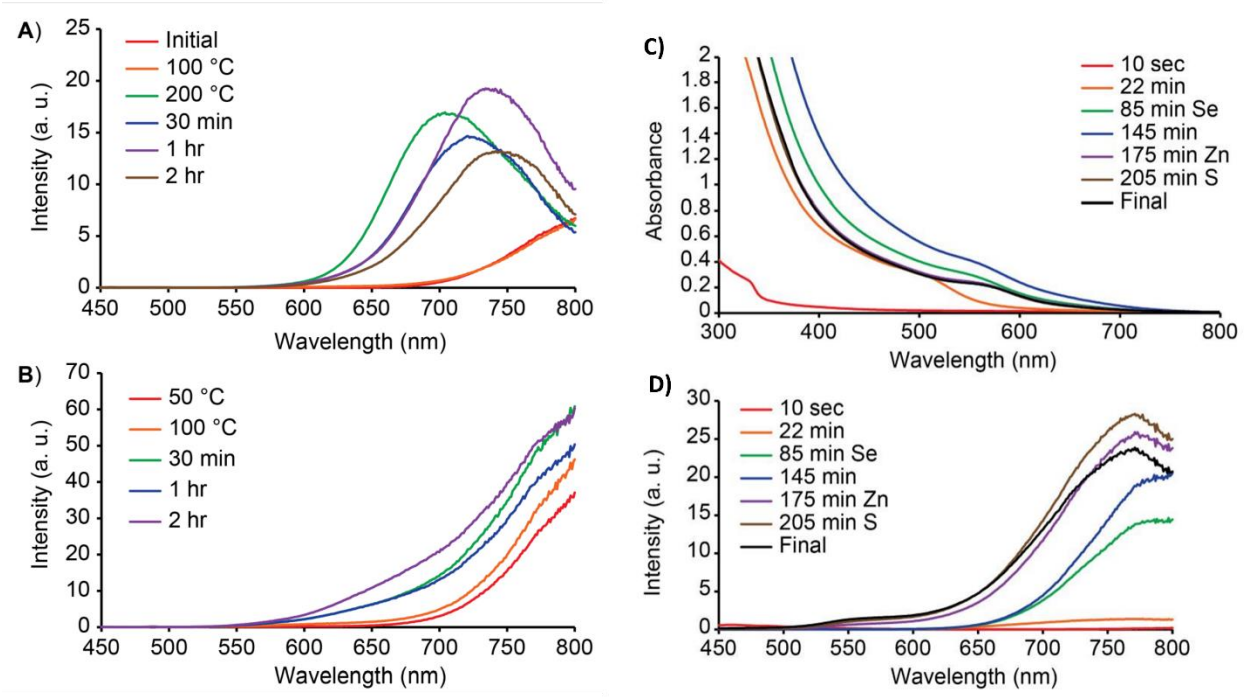

Figure 2.6. Photoluminescence of Cu^+:InP QDs after treatment with cadmium oleate at 200 °C (A) or 100 °C (B). Absorbance (C) and photoluminescence (D) of thickly shelled Cu^+:InP/ZnSeS QDs that were shelled *in situ*.

To our knowledge, this quantum yield is the highest reported for Cu+:InP, as prior studies reported copper-based PLQYs of up to only 40%, making this a dramatic 20% increase in PLQY.[6,9,11,33] As mentioned above, copper can be post-synthetically doped into InP NC cores and has been previously shown to incorporate post-synthetically into II–VI NCs with thin shells.[6,14] Using this established precedent, we explored copper incorporation in thinly (~1 monolayer) ZnSe-shelled InP NCs via cation exchange.[6,14] A copper chloride solution was added after shelling, and within 2 h the excitonic PL disappeared and the characteristic copper PL dominated the spectrum, with a PLQY of 40% (**Figure 2.7**). An initial 10:1 In:Cu molar ratio produced NCs with a final In:Cu ratio of 14:1, similar to the upper limit seen in the bottom-up synthesis. Thick-shelled InP NCs were also doped via the same method, but the time needed for

copper diffusion exceeded 12 hours with no comparative increase in PLQY relative to the thinly shelled materials. This may be due to distribution of copper throughout both the nanocrystal core and shell in these samples.

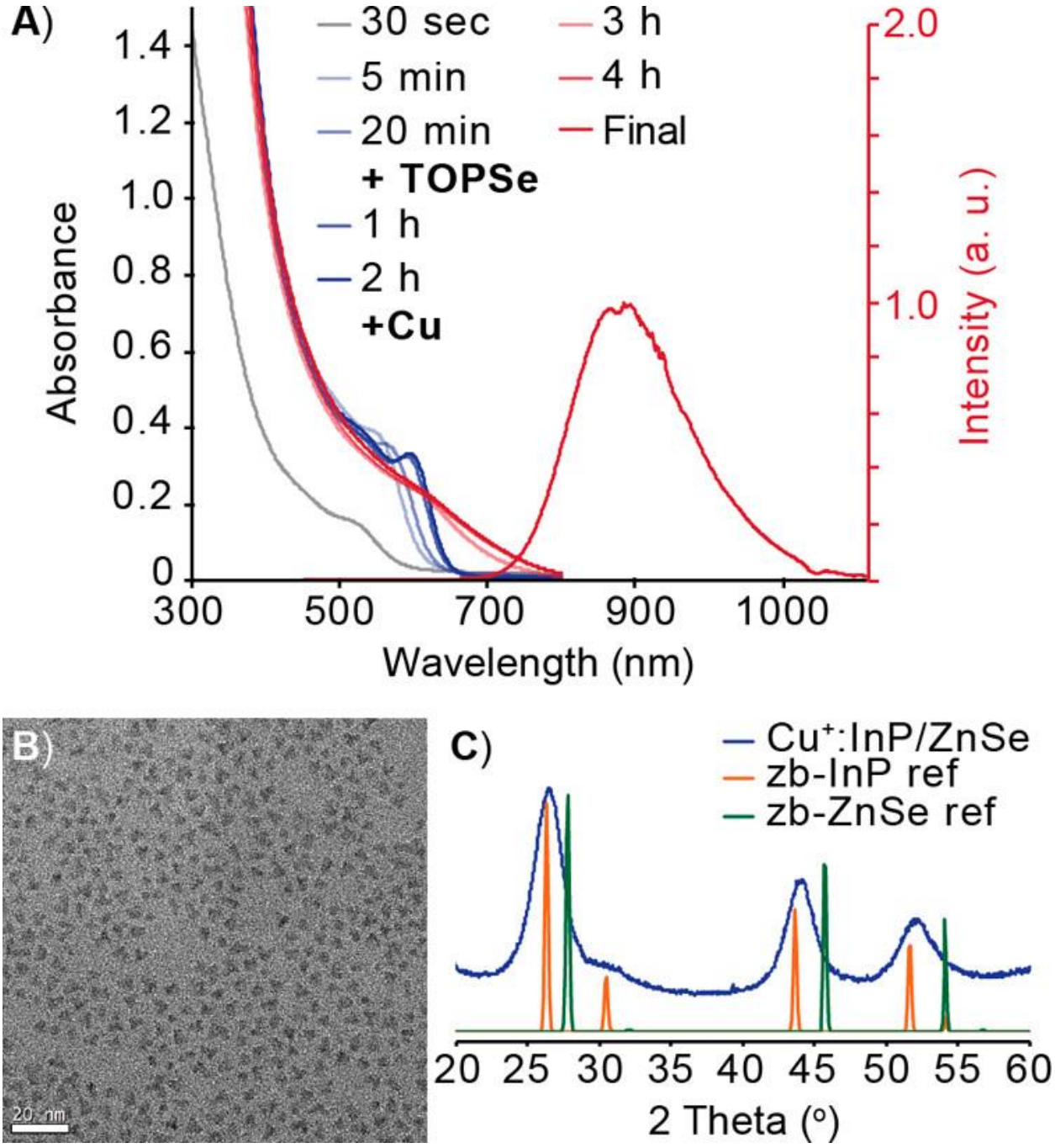

Figure 2.7. (A) UV–vis absorption spectra of reaction progress and final steady-state PL spectrum of a representative synthesis of Cu^{+}:InP/ZnSe NCs (40% PLQY). (B) TEM of Cu^{+}:InP/ZnSe NCs showing d = 4.2 ± 0.4 nm. (C) Powder X-ray diffraction pattern of the same NCs showing the crystalline phase present to be primarily InP with slight shifts toward ZnSe.

2.4 Spectroscopic analysis of Cu:InP and surface treated Cu:InP

Previous work showed that native carboxylate-ligated InP NCs exhibit electron trapping at undercoordinated indium sites within ~10 ns and sub-nanosecond hole trapping.[21,22] These trap states can be passivated by various surface treatments; in the case of our aminophosphine NCs, a zinc carboxylate treatment passivates electron traps by exchanging with either undercoordinated indium ions on the NC surface or datively bound Lewis bases like primary amine, while zinc chalcogenide shelling can passivate both electron and hole traps.[21]

As discussed above, upon introduction of Cu^+ into the InP NC lattice, the PLQY increases from ~1% to 10%, suggesting that the Cu^+ competes effectively with native surface traps for capture of the photogenerated hole. However, it is likely that a PLQY of only 10% still indicates the presence of significant carrier trapping at the NC surface. Therefore, the aforementioned surface treatments should help remove potential trap sites and increase the sample PLQY. We used TRPL spectroscopy to study recombination of the photogenerated delocalized conduction-band electron with the copper-localized hole as a function of these NC surface treatments. **Figure 2.8** shows PL decay curves measured for Cu^+:InP, Cu^+:InP/Zn, and Cu^+:InP/ZnSe NCs, plotted on a 1 μs window. Fitting the PL decay of the untreated Cu^+:InP NCs to a biexponential function gives a weighted PL lifetime of 272 ns. This result aligns well with previous reports of long luminescence lifetimes in copper-doped NCs, but the decay lifetime here is slightly shorter than the ~500 ns lifetime reported for Cu^+:InP/ZnS/InP/ZnS NCs.[39] This discrepancy could be due to a difference in the physical structures of the two materials, or it could indicate that our system still has competing carrier trapping pathways.[17] The PL decay of the Cu^+:InP/Zn NC sample is nearly identical, with a weighted lifetime of 313 ns. The Cu^+:InP/ZnSe NC sample,

however, has a much longer lifetime of 383 ns, indicating the efficiency with which even a thin layer of ZnSe can eliminate surface traps.

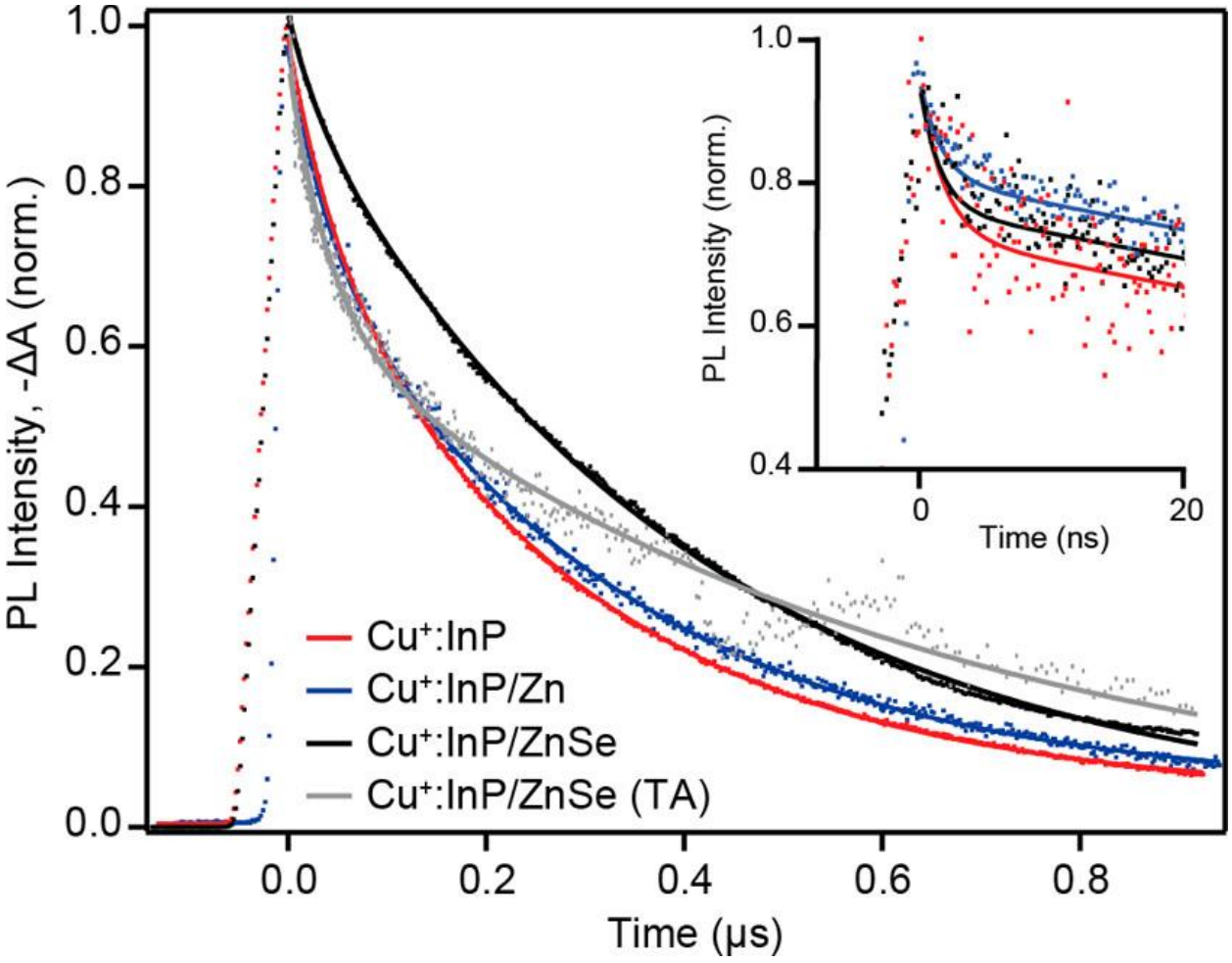

Figure 2.8 Normalized PL decay dynamics of the copper PL for Cu+:InP NCs (red), Cu^{+}:InP/Zn NCs (blue), and Cu^{+}:InP/ZnSe NCs (black). The inset shows the first 20 ns of data collected in a 100 ns window. In addition, normalized TA (−ΔA) data are shown for Cu^{+}:InP/ZnSe NCs (gray).

Despite similarities in the decay dynamics of the Cu^{+}:InP and Cu^{+}:InP/Zn NC samples, the PLQY of the Cu^{+}:InP/Zn NCs is 20%, double that of the Cu^{+}:InP NCs. Therefore, we also examined the PL decay dynamics on a 100 ns time scale (Figure 3 inset) to attempt to observe

faster processes. The Cu^+:InP and Cu^+:InP/Zn NCs appear to have very similar decay dynamics on this time scale as well, but the Cu^+:InP NCs decay almost twice as much as the Cu+:InP/Zn NCs in the first ~2 ns. This result shows that the zinc carboxylate surface treatment doubles the PLQY by eliminating trapping processes that occur on this time scale. The Cu^+:InP/ZnSe NCs also exhibit less ~2 ns decay than the Cu^+:InP NCs, and their slower decay on the 1 μs time scale accounts for their higher PLQY compared with the Cu^+:InP/Zn NCs. Moreover, examination of the excitonic bleach recovery dynamics of Cu^+:InP/ZnSe using transient absorption (TA) spectroscopy shows significant deviation from the corresponding TRPL data at early times (Figure 2.8). The observation of faster dynamics in the TA spectra provides strong support for hole localization at copper prior to other trapping processes and suggests that any differences in the decay dynamics we observe among surface-treated samples are due to differences in electron trapping. Since the TRPL specifically monitors the copper luminescence, the hole must be localized at copper for that signal to be observed. The presence of a faster component in the TA dynamics, however, indicates that trapping contributes to faster decay of the conduction-band electron (and hence the TA signal), consistent with the 40–45% PLQY. While fast hole trapping due to non-luminescent surface-bound copper ions has been previously implicated in Cu^+:InP,[40] we find this to be an unlikely explanation in the present system because of the observed trends in the fast-time TRPL data and the comparison with the TA dynamics.

2.5 Conclusion

In summary, we have developed a synthetic route to access highly luminescent copper-doped InP NCs from aminophosphine and metal halide precursors. The copper content can be tuned by altering the initial molar ratio or through post synthetic cation exchange, and the copper PL energy can be shifted by changing the indium precursor, which controls the size of the final

NCs. Upon surface modification, either by Lewis acid treatment with zinc carboxylate or by growth of a thin ZnSe shell, the PLQY increases. This PLQY increase is correlated with the decrease of an ~2 ns PL decay component and, in the case of the Cu^+:InP/ZnSe NCs, also with slower PL decay over the subsequent hundreds of nanoseconds. This work demonstrates that similar trapping processes occur in doped and undoped InP NCs and that surface treatments first developed for undoped InP NCs are effective in eliminating competing trap pathways in doped InP NCs as well. We are able to synthesize highly luminescent Cu^+:InP NCs and demonstrate the applicability of post synthetic surface modification for doped NC emitters.

2.6 Experimental Details

2.6.1 General Considerations and Chemicals

All glassware was dried in a 160 °C oven overnight prior to use. All reactions were run under an inert atmosphere of nitrogen using a glovebox or standard Schlenk techniques. Zinc chloride (>98%), tris-diethylaminophosphine (97%), copper (II) chloride (≥98%), indium (III) chloride (97%), indium (III) bromide (99%), and anhydrous isopropanol were purchased from Millipore-Sigma, stored in a nitrogen glovebox or desiccator, and used without further purification. Indium iodide (99%), copper (I) chloride (anhydrous 97%+), and copper (II) bromide (99%) were purchased from Strem Chemicals Inc., stored in a nitrogen glovebox or desiccator, and used without further purification. All other solvents including oleylamine, pentane, and toluene were purchased from Sigma Aldrich Chemical Co., dried over CaH_2, distilled, and stored over 4 Å sieves in a nitrogen glovebox. Omni Trace nitric acid was purchased from EMD Millipore and used without purification. 18.2 MΩ water was collected from an EMD Millipore water purification system. UV-Vis spectra were collected on a Cary

5000 spectrophotometer from Agilent. TEM images were collected on a FEI Tecnai G2 F20 microscope using an ultrathin carbon film on holey carbon purchased from Ted Pella Inc. P-XRD diffractograms were collected a Bruker Microfocus instrument. Luminescence spectra were collected on an Edinburgh FLS1000 fluorimeter. Photoluminescence quantum yields were measured with a Hamamatsu integrating sphere.

2.6.2 Standard doped indium phosphide reaction procedure

0.45 mmol of an indium halide, 2.2 mmol $ZnCl_2$, and 5 mL of dried and distilled oleylamine were added to a 25 mL 3-neck flask. The solution was then placed under vacuum at 120 °C and degassed for 1 hour. The vessel was then placed under an inert atmosphere and heated to 180 °C. Once the reaction temperature was reached, 0.45 mL of tris-diethylaminophosphine (1.6 mmol) was rapidly injected. The reaction was allowed to proceed for 5 minutes after which the previously prepared copper halide solution was slowly injected (2 mL at 4 mL/h). The flask was then cooled down to room temperature before being moved into a nitrogen glovebox for purification. The nanocrystals were precipitated with anhydrous methanol or isopropanol, centrifuged at 7830 rpm, and suspended in toluene. This procedure was repeated 5 times before any additional sample analysis was performed.

2.6.3 Thin shelled doped indium phosphide reaction procedure

0.23 mmol of an indium halide, 1.1 mmol of $ZnCl_2$, and 2.5 mL of dried and distilled oleylamine were added to a 15 mL 3-neck flask. The solution was then placed under vacuum at 120 °C and degassed for 1 hour. The vessel was then placed under an inert atmosphere and heated to 180 °C. Once the reaction temperature was reached, 0.23 mL of tris-diethylaminophosphine (0.8 mmol) was rapidly injected. The reaction was allowed to proceed

for 20 minutes after which 0.5 mL of the previously prepared 1M TOP=Se was slowly injected. At 60 minutes the temperature was increased to 200 ℃ and held there for an hour. At 120 minutes, the temperature was decreased to 150 ℃. Once temperature was reached the copper halide solution was slowly injected (1 mL at 2 mL/h). After the injection had completed the temperature was increased to 210 ℃ and held there for 1.5 hours. The flask was then cooled down to room temperature before being moved into a nitrogen glovebox for purification. The nanocrystals were precipitated with anhydrous methanol or isopropanol, centrifuged at 7830 rpm, and suspended in toluene. This procedure was repeated 5 times before any additional sample analysis was performed. Modified shelling procedures to grow a thicker ZnSeS shell used a method adapted Economic and Size-Tunable Synthesis of InP/ZnE (E = S, Se) Colloidal Quantum Dots. Chem. Mater., 2015, 27, 4893-4898 where TOP=Se was used in place of TOP=S in the first chalcogenide injection.

2.6.4 Zinc stearate treatment procedure

0.1 mmol zinc stearate was degassed in a 15 mL flask. Half of a previously prepared Cu^{+}:InP nanocrystal reaction at the 0.45 mmol scale was precipitated once and then resuspended in 4 mL of 1-octadecene. The solution containing approximately 0.2 mmol of indium was injected into the flask containing the zinc stearate at room temperature. The entire solution was gently heated while stirring to 100 ℃ and held at that temperature for 2 hours. The flask was then cooled down to room temperature before being moved into a nitrogen glovebox for purification. The nanocrystals were precipitated with anhydrous methanol or isopropanol, centrifuged at 7830 rpm, and suspended in toluene. This procedure was repeated 5 times before any additional sample analysis was performed.

2.6.5 Photophysical characterization methods

Room-temperature TRPL measurements were performed by exciting colloidal NCs at 365 nm via a Coherent Inc./Light Source OPerA optical parametric amplifier, power measured at ~50 μW. Time-resolved PL spectra were collected using a Hamamatsu streak camera with a synchroscan unit. Room temperature transient absorption measurements were performed using an EOS unit from Ultrafast Systems at the University of Washington's Molecular Analysis Facility. The pump wavelength of 365 nm was generated via a Coherent Inc./Light Source OPerA optical parametric amplifier, with a power of ~50 μW measured through a 200μm pinhole. The probe white light was generated using an external Q-switched Nd:YAG laser with an electronic delay. The collinear pump and probe beams overlapped at the sample. PL data were acquired using an excitation wavelength of 365 nm, and PL decay curves were obtained by integrating between 780 and 880 nm. TA data were acquired using a 365 nm pump pulse followed by a continuum white-light probe pulse. The dynamics was obtained by integration of the TA bleach between 654 and 714 nm.

2.7 REFERENCES

1. Talapin, D. V.; Steckel, J. Quantum Dot Light-Emitting Devices. *MRS Bull.* **2013**, *38*, 685– 691, DOI: 10.1557/mrs.2013.204
2. Talapin, D. V.; Lee, J.-S.; Kovalenko, M. V.; Shevchenko, E. V. Prospects of Colloidal Nanocrystals for Electronic and Optoelectronic Applications. *Chem. Rev.* **2010**, *110*, 389– 458, DOI: 10.1021/cr900137k
3. Kramer, I. J.; Sargent, E. H. Colloidal Quantum Dot Photovoltaics: A Path Forward. *ACS Nano* **2011**, *5*, 8506– 8514, DOI: 10.1021/nn203438u
4. Medintz, I.; Uyeda, H.; Goldman, E.; Mattoussi, H. Quantum Dot Bioconjugates for Imaging, Labelling and Sensing. *Nat. Mater.* **2005**, *4*, 435– 446, DOI: 10.1038/nmat1390
5. Knowles, K. E.; Hartstein, K. H.; Kilburn, T. B.; Marchioro, A.; Nelson, H. D.; Whitham, P. J.; Gamelin, D. R. Luminescent Colloidal Semiconductor Nanocrystals Containing Copper: Synthesis, Photophysics, and Applications. *Chem. Rev.* **2016**, *116*, 10820– 10851, DOI: 10.1021/acs.chemrev.6b00048

6. Xie, R.; Peng, X. Synthesis of Cu-Doped InP Nanocrystals (d-Dots) with ZnSe Diffusion Barrier as Efficient and Color-Tunable NIR Emitters. *J. Am. Chem. Soc.* **2009**, *131*, 10645– 10651, DOI: 10.1021/ja903558r

7. Srivastava, B. B.; Jana, S.; Pradhan, N. Doping Cu in Semiconductor Nanocrystals: Some Old and Some New Physical Insights. *J. Am. Chem. Soc.* **2011**, *133*, 1007– 1015, DOI: 10.1021/ja1089809

8. Grandhi, G. K.; Viswanatha, R. Tunable Infrared Phosphors Using Cu Doping in Semiconductor Nanocrystals: Surface Electronic Structure Evaluation. *J. Phys. Chem. Lett.* **2013**, *4*, 409– 415, DOI: 10.1021/jz3021588

9. Knowles, K. E.; Nelson, H. D.; Kilburn, T. B.; Gamelin, D. R. Singlet–Triplet Splittings in the Luminescent Excited States of Colloidal Cu+:CdSe, Cu+:InP, and CuInS2 Nanocrystals: Charge-Transfer Configurations and Self-Trapped Excitons. *J. Am. Chem. Soc.* **2015**, *137*, 13138– 13147, DOI: 10.1021/jacs.5b08547

10. Cooper, J. K.; Gul, S.; Lindley, S. A.; Yano, J.; Zhang, J. Z. Tunable Photoluminescent Core/Shell Cu+-Doped ZnSe/ZnS Quantum Dots Codoped with Al3+, Ga3+, or In3+. *ACS Appl. Mater. Interfaces* **2015**, *7*, 10055– 10066, DOI: 10.1021/acsami.5b02860

11. Hassan, A.; Zhang, X.; Liu, X.; Rowland, C. E.; Jawaid, A. M.; Chattopadhyay, S.; Gulec, A.; Shamirian, A.; Zuo, X.; Klie, R. F.; Schaller, R. D.; Snee, P. T. Charge Carriers Modulate the Bonding of Semiconductor Nanoparticle Dopants As Revealed by Time-Resolved X-ray Spectroscopy. *ACS Nano* **2017**, *11*, 10070– 10076, DOI: 10.1021/acsnano.7b04414

12. Sharma, M.; Gungor, K.; Yeltik, A.; Olutas, M.; Guzelturk, B.; Kelestemur, Y.; Erdem, T.; Delikanli, S.; McBride, J. R.; Demir, H. V. Near-Unity Emitting Copper-Doped Colloidal Semiconductor Quantum Wells for Luminescent Solar Concentrators. *Adv. Mater.* **2017**, *29*, 1700821, DOI: 10.1002/adma.201700821

13. Bradshaw, L. R.; Knowles, K. E.; McDowall, S.; Gamelin, D. R. Nanocrystals for Luminescent Solar Concentrators. *Nano Lett.* **2015**, *15*, 1315– 1323, DOI: 10.1021/nl504510t

14. Hughes, K. E.; Hartstein, K. H.; Gamelin, D. R. Photodoping and Transient Spectroscopies of Copper-Doped CdSe/CdS Nanocrystals. *ACS Nano* **2018**, *12*, 718– 728, DOI: 10.1021/acsnano.7b07879

15. Hanifi, D. A.; Bronstein, N. D.; Koscher, B. A.; Nett, Z.; Swabeck, J. K.; Takano, K.; Schwartzberg, A. M.; Maserati, L.; Vandewal, K.; van de Burgt, Y.; Salleo, A.; Alivisatos, A. P. Redefining Near-Unity Luminescence in Quantum Dots with Photothermal Threshold Quantum Yield. *Science* **2019**, *363*, 1199, DOI: 10.1126/science.aat3803

16. Tarantini, A.; Wegner, K. D.; Dussert, F.; Sarret, G.; Beal, D.; Mattera, L.; Lincheneau, C.; Proux, O.; Truffier-Boutry, D.; Moriscot, C.; Gallet, B.; Jouneau, P.-H.; Reiss, P.; Carrière, M. Physicochemical Alterations and Toxicity of InP Alloyed Quantum Dots

Aged in Environmental Conditions: A Safer by Design Evaluation. *NanoImpact* **2019**, *14*, 100168, DOI: 10.1016/j.impact.2019.100168

17. Wegner, K. D.; Dussert, F.; Truffier-Boutry, D.; Benayad, A.; Beal, D.; Mattera, L.; Ling, W. L.; Carrière, M.; Reiss, P. Influence of the Core/Shell Structure of Indium Phosphide Based Quantum Dots on Their Photostability and Cytotoxicity. *Front. Chem.* **2019**, *7*, 466, DOI: 10.3389/fchem.2019.00466

18. Won, Y.-H.; Cho, O.; Kim, T.; Chung, D.-Y.; Kim, T.; Chung, H.; Jang, H.; Lee, J.; Kim, D.; Jang, E. Highly Efficient and Stable InP/ZnSe/ZnS Quantum Dot Light-Emitting Diodes. *Nature* **2019**, *575*, 634– 638, DOI: 10.1038/s41586-019-1771-5

19. Kim, Y.; Ham, S.; Jang, H.; Min, J. H.; Chung, H.; Lee, J.; Kim, D.; Jang, E. Bright and Uniform Green Light Emitting InP/ZnSe/ZnS Quantum Dots for Wide Color Gamut Displays. *ACS Appl. Nano Mater.* **2019**, *2*, 1496– 1504, DOI: 10.1021/acsanm.8b02063

20. Ramasamy, P.; Ko, K.-J.; Kang, J.-W.; Lee, J.-S. Two-Step "Seed-Mediated" Synthetic Approach to Colloidal Indium Phosphide Quantum Dots with High-Purity Photo- and Electroluminescence. *Chem. Mater.* **2018**, *30*, 3643– 3647, DOI: 10.1021/acs.chemmater.8b02049

21. Hughes, K. E.; Stein, J. L.; Friedfeld, M. R.; Cossairt, B. M.; Gamelin, D. R. Effects of Surface Chemistry on the Photophysics of Colloidal InP Nanocrystals. *ACS Nano* **2019**, *13*, 14198– 14207, DOI: 10.1021/acsnano.9b07027

22. Janke, E. M.; Williams, N. E.; She, C.; Zherebetskyy, D.; Hudson, M. H.; Wang, L.; Gosztola, D. J.; Schaller, R. D.; Lee, B.; Sun, C.; Engel, G. S.; Talapin, D. V. Origin of Broad Emission Spectra in InP Quantum Dots: Contributions from Structural and Electronic Disorder. *J. Am. Chem. Soc.* **2018**, *140*, 15791– 15803, DOI: 10.1021/jacs.8b08753

23. Richter, A. F.; Binder, M.; Bohn, B. J.; Grumbach, N.; Neyshtadt, S.; Urban, A. S.; Feldmann, J. Fast Electron and Slow Hole Relaxation in InP-Based Colloidal Quantum Dots. *ACS Nano* **2019**, *13*, 14408– 14415, DOI: 10.1021/acsnano.9b07969

24. Stein, J. L.; Mader, E. A.; Cossairt, B. M. Luminescent InP Quantum Dots with Tunable Emission by Post-Synthetic Modification with Lewis Acids. *J. Phys. Chem. Lett.* **2016**, *7*, 1315– 1320, DOI: 10.1021/acs.jpclett.6b00177

25. Kirkwood, N.; Monchen, J. O. V.; Crisp, R. W.; Grimaldi, G.; Bergstein, H. A. C.; du Fossé, I.; van der Stam, W.; Infante, I.; Houtepen, A. J. Finding and Fixing Traps in II–VI and III–V Colloidal Quantum Dots: The Importance of Z-Type Ligand Passivation. *J. Am. Chem. Soc.* **2018**, *140*, 15712– 15723, DOI: 10.1021/jacs.8b07783

26. Tessier, M. D.; De Nolf, K.; Dupont, D.; Sinnaeve, D.; De Roo, J.; Hens, Z. Aminophosphines: A Double Role in the Synthesis of Colloidal Indium Phosphide Quantum Dots. *J. Am. Chem. Soc.* **2016**, *138*, 5923– 5929, DOI: 10.1021/jacs.6b01254

27. Tessier, M. D.; Dupont, D.; De Nolf, K.; De Roo, J.; Hens, Z. Economic and Size-Tunable Synthesis of InP/ZnE (E = S, Se) Colloidal Quantum Dots. *Chem. Mater.* **2015**, *27*, 4893– 4898, DOI: 10.1021/acs.chemmater.5b02138

28. Buffard, A.; Dreyfuss, S.; Nadal, B.; Heuclin, H.; Xu, X.; Patriarche, G.; Mézailles, N.; Dubertret, B. Mechanistic Insight and Optimization of InP Nanocrystals Synthesized with Aminophosphines. *Chem. Mater.* **2016**, *28*, 5925– 5934, DOI: 10.1021/acs.chemmater.6b02456

29. Laufersky, G.; Bradley, S.; Frécaut, E.; Lein, M.; Nann, T. Unraveling Aminophosphine Redox Mechanisms for Glovebox-Free InP Quantum Dot Syntheses. *Nanoscale* **2018**, *10*, 8752– 8762, DOI: 10.1039/C8NR01286E

30. Mundy, M. E.; Ung, D.; Lai, N. L.; Jahrman, E. P.; Seidler, G. T.; Cossairt, B. M. Aminophosphines as Versatile Precursors for the Synthesis of Metal Phosphide Nanocrystals. *Chem. Mater.* **2018**, *30*, 5373– 5379, DOI: 10.1021/acs.chemmater.8b02206

31. Song, W.-S.; Lee, H.-S.; Lee, J. C.; Jang, D. S.; Choi, Y.; Choi, M.; Yang, H. Amine-Derived Synthetic Approach to Color-Tunable InP/ZnS Quantum Dots with High Fluorescent Qualities. *J. Nanopart. Res.* **2013**, *15*, 1750, DOI: 10.1007/s11051-013-1750-y

32. Huang, F.; Bi, C.; Guo, R.; Zheng, C.; Ning, J.; Tian, J. Synthesis of Colloidal Blue-Emitting InP/ZnS Core/Shell Quantum Dots with the Assistance of Copper Cations. *J. Phys. Chem. Lett.* **2019**, *10*, 6720– 6726, DOI: 10.1021/acs.jpclett.9b02386

33. Mei, S.; Wei, X.; Yang, D.; Su, D.; Yang, W.; Zhang, G.; Hu, Z.; Yang, B.; Dai, H.; Xie, F.; Zhang, W.; Guo, R. Color-Tunable Optical Properties of Cadmium-Free Transition Metal Ions Doped InP/ZnS Quantum Dots. *J. Lumin.* **2019**, *212*, 264– 270, DOI: 10.1016/j.jlumin.2019.04.040

34. Wei, X.; Mei, S.; Zhang, G.; Su, D.; Xie, F.; Zhang, W.; Guo, R. Enhanced Tunable Dual Emission of Cu:InP/ZnS Quantum Dots Enabled by Introducing Ag Ions. *Appl. Surf. Sci.* **2019**, *493*, 605– 612, DOI: 10.1016/j.apsusc.2019.06.059

35. Yang, L.; Knowles, K. E.; Gopalan, A.; Hughes, K. E.; James, M. C.; Gamelin, D. R. One-Pot Synthesis of Monodisperse Colloidal Copper-Doped CdSe Nanocrystals Mediated by Ligand–Copper Interactions. *Chem. Mater.* **2016**, *28*, 7375– 7384, DOI: 10.1021/acs.chemmater.6b02869

36. Ruberu, T. P. A.; Albright, H. R.; Callis, B.; Ward, B.; Cisneros, J.; Fan, H.-J.; Vela, J. Molecular Control of the Nanoscale: Effect of Phosphine–Chalcogenide Reactivity on CdS–CdSe Nanocrystal Composition and Morphology. *ACS Nano* **2012**, *6*, 5348– 5359, DOI: 10.1021/nn301182h

37. Hunt, C. T.; Balch, A. L. Scrambling of Halide Ligands between Palladium(II) and between Palladium(I) Complexes of Bis(Diphenylphosphino)Methane. Observation of Unusual Temperature-Dependent Phosphorus-31 NMR Chemical Shifts. *Inorg. Chem.* **1982**, *21*, 1641– 1644, DOI: 10.1021/ic00134a073

38. Stein, J. L.; Steimle, M. I.; Terban, M. W.; Petrone, A.; Billinge, S. J. L.; Li, X.; Cossairt, B. M. Cation Exchange Induced Transformation of InP Magic-Sized Clusters. *Chem. Mater.* **2017**, *29*, 7984– 7992, DOI: 10.1021/acs.chemmater.7b03075

39. Zhang, Z.; Liu, D.; Li, D.; Huang, K.; Zhang, Y.; Shi, Z.; Xie, R.; Han, M.-Y.; Wang, Y.; Yang, W. Dual Emissive Cu:InP/ZnS/InP/ZnS Nanocrystals: Single-Source "Greener" Emitters with Flexibly Tunable Emission from Visible to Near-Infrared and Their Application in White Light-Emitting Diodes. *Chem. Mater.* **2015**, *27*, 1405– 1411, DOI: 10.1021/cm5047269

40. Hassan, A.; Zhang, X.; Liu, C.; Snee, P. T. Electronic Structure and Dynamics of Copper-Doped Indium Phosphide Nanocrystals Studied with Time-Resolved X-ray Absorption and Large-Scale DFT Calculations. *J. Phys. Chem. C* **2018**, *122*, 11145– 11151, DOI: 10.1021/acs.jpcc.8b02124

3 ENHANCED CHARGE TRANSFER FROM COINAGE METAL DOPED INP QUANTUM DOTS

Significant portions of this chapter have been published by:

Forrest W. Eagle, Samantha Harvey, Ryan Beck, Xiaosong Li, Daniel R. Gamelin, and Brandi M. Cossairt. *ACS Nanoscience Au*, **2023**, 3, 6, 451-461

3.1 NOTE FOR COLLABORATIVE WORK

All theoretical work calculations were performed by Dr. Ryan Beck, under the guidance of Professor Xiaosong Li in the Department of Chemistry at the University of Washington. Transient absorption data were collected by Dr. Samantha Harvey under the co-guidance of Professor Brandi Cossairt and Daniel Gamelin.

3.2 INTRODUCTION

With the global demand for value-added chemical products increasing each year, new catalytic materials must be developed to improve process efficiency. Many current processes require the use of intense reaction conditions, such as a high pressure or temperature. Solar powered catalysts offer an attractive alternative or supplement to current processes. Efficient photocatalytic materials typically require three characteristics: high extinction coefficients, high photostability, and long-lived photoexcited states. Many current photocatalysts are based on rare metals such as rhodium or iridium, which can have high turnover numbers depending on the specific reaction.[1,2] However, these compounds often do not have large absorption cross sections at $\lambda > 400$ nm, which results in underutilization of the solar spectrum.

Quantum dots (QDs) intrinsically have large, tunable extinction coefficients,[3] which can be further enhanced by adding inorganic shells on their surfaces.[4] Inorganic shells also improve quantum dot stability [5–7] and passivate surface states that serve as charge carrier traps.[8,9] By shelling using a traditional Type-1 heterostructure, charge carriers are highly localized to the core of the quantum dot, [10] making charge transfer difficult due to the energetic barrier for tunneling. This, along with the relatively short excited-state lifetimes found in traditional III–V and II–VI quantum dots (QDs) (<50 ns),[11,12] makes them a poor platform for photoredox catalysis. Despite these issues, quantum dots have been shown to perform a catalogue of photochemical reactions, such as hydrogen evolution and organic C–C, C–O, and C–N bond making and breaking reactions. However, photocatalytic organic reactions typically occur through optically dark triplet-like excitonic states and hydrogen evolution often requires cocatalysts.[13–16]

With the idea of designing improved quantum dot photocatalysts, the observation that coinage metal dopants, such as copper, enhance charge-carrier lifetimes by over an order of magnitude is notable.[17–20] This increase in is found in II–VI nanocrystals (and InP) as these dopants introduce hole trap states, where photoexcited electrons can recombine with trapped holes.[21,22]

Recent work in our lab has demonstrated the introduction of copper dopants into III–V quantum dots, along with the spectroscopic examination of the charge carriers, finding that the photogenerated hole rapidly localizes to the copper site before other trapping processes occur similar to what has been observed in II–VI systems.[17,19–21,23,24] Previous theoretical work has investigated the electronic structure of Cu^+ and Ag^+ doped CdSe quantum dots, showing that the emissive excited state consists of a delocalized electron and a hole localized at the copper

dopant, with broad photoluminescence spectra arising due to vibronic coupling.[18,19] Theoretical work on Cu^+-doped InP suggested that their electronic structure is strongly dependent on ligand coating and other effects such as self-compensation.[25]

Here we prepare a series of Cu^+- and Ag^+-doped InP QDs, each shelled with a monolayer of ZnSe. The physical and electronic structures are studied by means of electron microscopy, elemental analysis, powder X-ray diffraction, steady-state and time-resolved optical spectroscopy, and first-principles DFT calculations. Using a combination of static and dynamic fluorescence quenching experiments and transient-absorption spectroscopy, we demonstrate the enhancement of electron transfer upon doping InP quantum dots with Cu^+ and Ag^+. We also show that this enhancement is strongly dependent on the electron acceptor's mechanism of adsorption to the quantum dot surface. Smaller acceptors show the highest rates of electron transfer from doped QDs but also lower enhancement when comparing doped versus undoped QDs due to the ability to adsorb directly to the surface of the quantum dot without requiring a dissociation step.

3.3 Results and Discussion

3.3.1 Synthesis and characterization of doped InP/ZnSe

A general synthesis of core/shell InP/ZnSe QDs was adapted from ref ([23]) **(Figure 3.1**). In brief, 1 equivalents of indium halide, approximately 5 equivalents of $ZnCl_2$, and an excess of dried and distilled oleylamine were combined, degassed at 120 °C, and heated to 180 °C. Approximately 4 equivalents of tris-diethylaminophosphine was then rapidly injected. After a fixed period of time (see experimental section), 1 M TOP=Se was slowly injected. After an hour, the reaction temperature was increased to 200 °C and held for an additional hour. Doped

samples were synthesized following the same method as above with a few notable changes. After 120 min of reaction with TOP=Se, the temperature was decreased to 150 °C and a solution of 0.1 equivalents of copper(II) chloride ($CuCl_2$) or silver(I) chloride (AgCl) was slowly injected (1 mL at 2 mL/h). After complete addition, the temperature was increased to 210 °C and held there for 1.5 h. In all cases, purification was achieved by 5 repeated cycles of precipitation and redissolution with anhydrous ethanol and toluene, respectively.

Figure 3.1

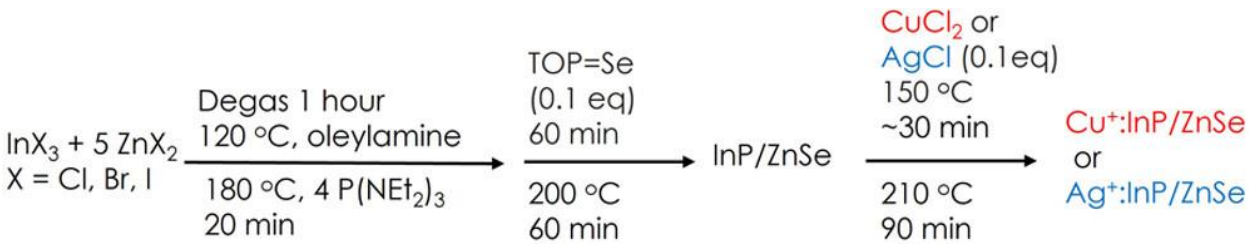

Figure 3.1. General Synthesis of Coinage Metal Doped InP/ZnSe Core/Shell QDs

Using this method, ICP-OES data show InP/ZnSe QDs with 11% Cu and 6% Ag (reported as cation mole fraction, **Table 3.1**). The QDs show little change in structure as determined by powder X-ray diffraction (**Figure 3.2C**). Additionally, the crystallite sizes remain similar pre- and post-cation exchange, all averaging approximately 2.9 nm by Scherrer analysis and 3.0 nm by TEM size analysis.

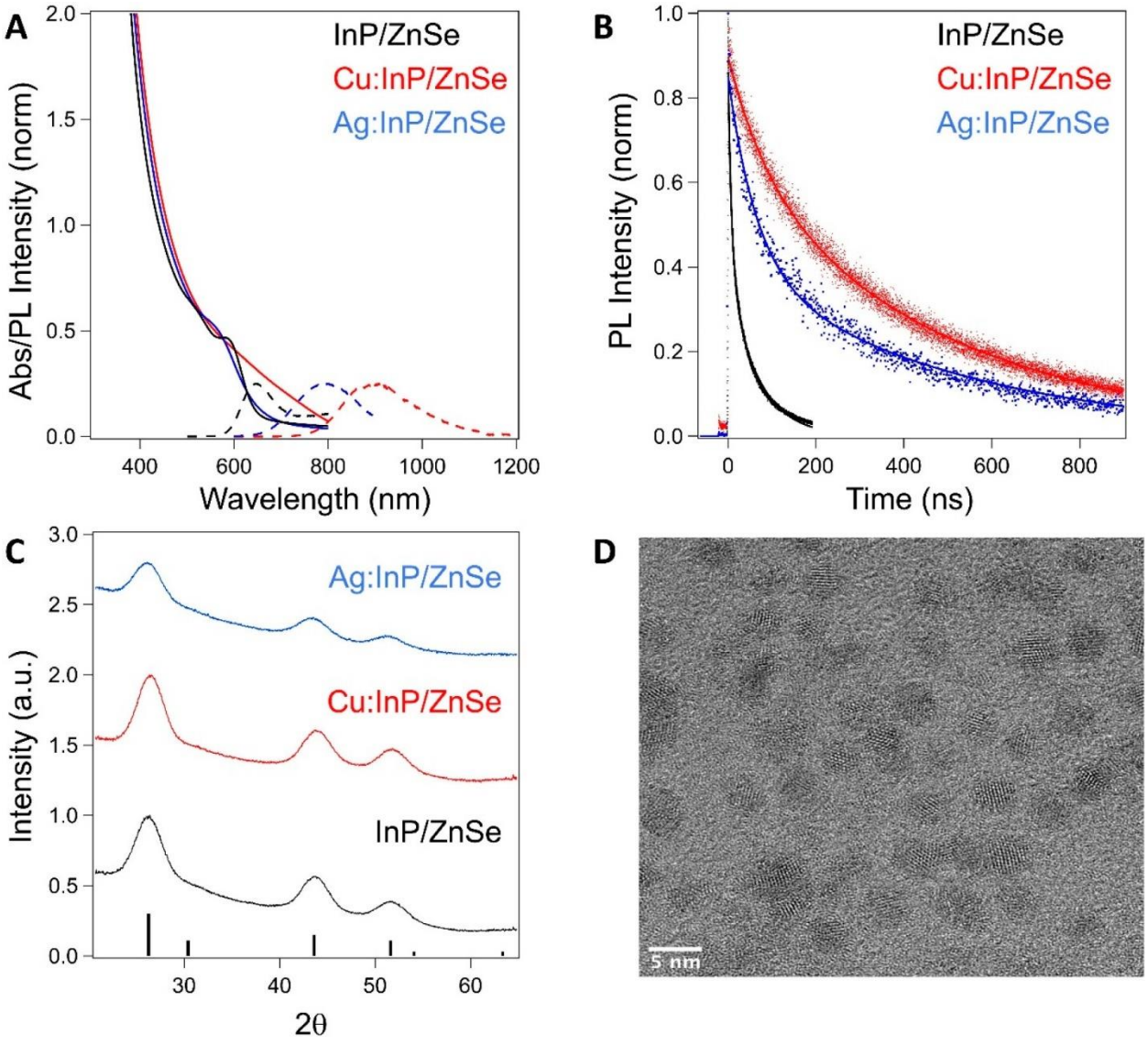

Figure 3.2. (A) Representative absorption(solid) and photoluminescence (dashed) spectra of InP/ZnSe (black), Ag^+:InP/ZnSe (blue), and Cu^+:InP/ZnSe (red) QDs. (B) Time-resolved photoluminescence decay profiles of InP/ZnSe, Ag^+:InP/ZnSe, and Cu^+:InP/ZnSe QDs. (C) Powder XRD patterns of InP/ZnSe, Ag^+:InP/ZnSe, and Cu^+:InP/ZnSe QDs. All data were collected at room temperature. (D) Representative TEM image of purified Cu^+:InP/ZnSe QDs.

Table 3.1. ICP-OES analysis of samples.

	In	**P**	**Zn**	**Se**	**Ag**	**Cu**	**Dopant Cation Mole Fraction [M]/([M]+[In]+[Zn])**
InP/ZnSe	1	0.83	0.2	0.77			0
Ag:InP/ZnSe	1	0.87	0.18	0.8	0.08		0.06
Cu:InP/ZnSe	1	0.815	0.22	0.7		0.15	0.11

Figure 3.2A shows the absorption and photoluminescence spectra of the InP/ZnSe, Ag^+:InP/ZnSe, and Cu^+:InP/ZnSe QDs. Both doped species of InP show broadened absorption compared to the undoped InP/ZnSe QDs. Time-resolved photoluminescence measurements show lengthening of the luminescence lifetime from ~30 ns in the undoped QDs to ~270 ns in the Ag^+-doped QDs and ~360 ns in the Cu^+ doped QDs (**Figure 3.2B**) (these data were fit to biexponential functions with the following amplitudes and time constants: InP/ZnSe (A_1 = 0.466 ± 0.001, τ_1 = 8.11 ± 0.04 ns, A_2 = 0.393 ± 0.001, τ_2 = 65.56 ± 0.16 ns, $\tau_{weighted}$ = 34.4 ns), Ag^+:InP/ZnSe (A_1 = 0.449 ± 0.004, τ_1 = 64.01 ± 1.31 ns, A_2 = 0.401 ± 0.003, τ_2 = 517.38 ± 4.27 ns, $\tau_{weighted}$ = 278.14 ns), and Cu^+:InP/ZnSe (A_1 = 0.264 ± 0.003 , τ_1 = 92.17 ± 1.74 ns, A_2 = 0.631 ± 0.003, τ_2 =500.38 ± 2.35 ns, $\tau_{weighted}$ = 379.8 ns)). Upon photoexcitation, the photogenerated hole rapidly localizes to the Cu center within 2 ps,[26] reducing the electron–hole wave function overlap, and slowing recombination. While no report has described the photoluminescence of Ag^+:InP QDs, they appear similar to those of Ag^+ doped CdSe QDs.

To further understand the behavior of the photoexcited charge carriers in these doped systems, they were examined in silico using $In_{77}P_{77}$ and $[In_{76}MP_{77}]^{2-}$ (M = Ag, Cu) model quantum dots. All QDs were terminated by pseudohydrogens (e.g., $In_{77}P_{77}H_{108}$) to provide charge balance and minimize the exaggerated surface effects that may result from small cluster models. Upon optimization, the geometry of the InP QD around the dopant broke the C3v starting symmetry, as can be seen in **Figure 3.3A.** The addition of the metal dopant gives rise to midgap states, which are shown in **Figure 3.3B**. To gain insight into the band structure, density of states (DOS) plots are provided in **Figure 3.3C**. Examining the DOS for the undoped QD, the valence band can be seen to be comprised primarily of phosphide character, while the conduction band is primarily indium based. Upon doping, the valence and conduction bands are still composed of phosphorus and indium, respectively; however, copper and silver contributions appear in new mid-gap states. Examining these mid-gap states shows that, while still primarily composed of phosphorus p orbitals, the doping metal contributes d orbital character that affects the ionization potential. Between the Cu^+ and Ag^+ the highest occupied molecular orbitals (HOMOs) have the same character; however, a reordering of the states between the Cu^+:InP and Ag^+:InP can be seen in **Figure 3.3B** where the Ag^+ HOMO–1 is the same as the Cu+ HOMO–2 (and vice versa). This reordering results in slightly different character for the leaving (hole) orbitals between the Cu^+:InP and the Ag^+:InP as can be viewed in **Figure 3.3C**. The increased d orbital contribution to the mid-gap states by the Cu^+ atom with respect to Ag^+, and different hole character can be ascribed to the difference in d-orbital character between the Cu^+ and Ag^+ ions. This differing character has been noted previously.[18] Even with this orbital reordering, the excited state properties of both systems are similar. Predicted absorption spectra for these geometries are shown in **Figure 3.3C**. Examining the natural transition orbitals (NTOs), inset

into the absorption spectra, the first transition is easily determined to be a transition from the occupied midgap state to the unoccupied conduction band.

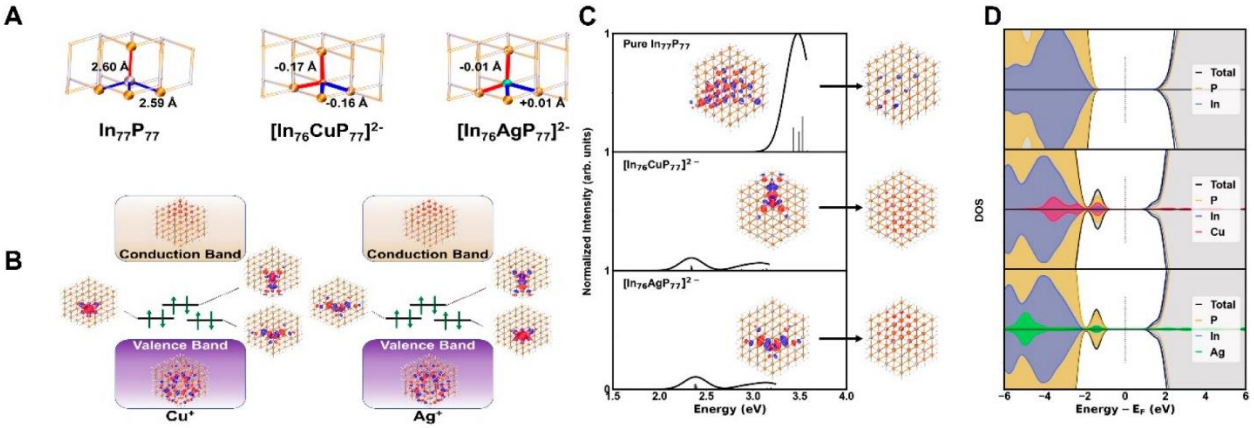

Figure 3.3. (A) Optimized geometries for the undoped ($In_{77}P_{77}$), copper-doped ($[In_{76}CuP_{77}]^{2-}$), and silver-doped ($[In_{76}AgP_{77}]^{2-}$) quantum dots. The atoms shown are those immediately surrounding the metal center. Changes in the bond length for $[In_{76}CuP_{77}]^{2-}$ and $[In_{76}AgP_{77}]^{2-}$ are given in relation to the undoped structure. The same color marks a bond that is the same length. (B) Molecular orbital diagrams for the $[In_{76}CuP_{77}]^{2-}$ quantum dot (left) and the $[In_{76}AgP_{77}]^{2-}$ quantum dot (right). Pictured are the midgap molecular orbitals plotted with an isovalue of 0.01 electron·Bohr^{-3}. Black bars mark the midgap states (not drawn to scale), with green arrows marking the occupation for the spin up and spin down electrons. (C) Predicted absorption spectra of the undoped $In_{77}P_{77}$ QD, $[In_{76}CuP_{77}]^{2-}$, and $[In_{76}AgP_{77}]^{2-}$ QDs are shown on the left. Inset into each plot are the natural transition orbitals for the first excitation (numerical values for the energy given in Table 1) with the leaving (hole) orbital on the left and the arriving (electron) orbital on the right. The density of states plots for the undoped QD, the $[In_{76}CuP_{77}]^{2-}$ and $[In_{76}AgP_{77}]^{2-}$ QDs with positive values corresponding to spin up electrons and negative values corresponding to spin down electrons, are shown on the right.

Due to the similar nature of the transitions between Cu+:InP and Ag+:InP QDs, a quantitative method is required to differentiate the localization between the two metal dopants.

This is achieved using the hole/electron delocalization index (HDI and EDI, respectively) as implemented in Multiwfn.[27,28] This value is able to give a numerical value for the density over the space occupied by the hole/electron corresponding to an excitation. A lower value indicates that the hole or electron is more delocalized in space. Examining Table 2.2 for the HDI, we found that the most delocalized system (that with the lowest HDI value) is the undoped system. This is expected, as the first transition for the undoped $In_{77}P_{77}$ QD is a band-to-band type transition. When the dopants are added, the HDI grows, showing the hole localization that we have already observed in **Figure 3.3C**, but the HDI for the Cu^+:InP QDs is greater than that for the Ag^+:InP QDs. The EDI values for the doped QDs are both similar to that of the undoped QD.

Table 3.2. Excitation Energy for the First Transition along with the Corresponding Hole and Electron Delocalized Index for the InP Quantum Dots

dot	**excitation [eV] (osc. str.)**	**hole delocalization index (a.u.)**	**electron delocalization index (a.u.)**
$In_{77}P_{77}$	3.429 (0.1854)	2.14	1.22
$[In_{76}CuP_{77}]^{2-}$	2.337 (0.0391)	16.89	1.07
$[In_{76}AgP_{77}]^{2-}$	2.374 (0.0357)	6.61	1.09

3.3.2 Photoluminescence quenching with anthraquinone

To study photoinduced charge transfer from these quantum dots, we examined a series of quinones as electron acceptors. Not only are quinones readily soluble in many of the same organic solvents as quantum dots, but they have previously been shown to accept electrons from photoexcited quantum dots.[29–32] By an increase in the concentration of anthraquinone in the QD

solution, a decrease in the QD fluorescence intensity is observed. This decrease can be attributed to the formation of a quantum dot-anthraquinone* adduct, where the electron has been transferred from the photoexcited quantum dot to the anthraquinone adsorbed on the surface. By fitting the loss of luminescence with respect to the concentration of added quencher to the Stern–Volmer equation (**Equation 3.1**), we can extract a Stern–Volmer quenching constant, K_{SV}, that measures how readily electron transfer occurs between the photoexcited quantum dot and the quinone acceptor. In **Equation 3.1**, F_0 is defined as the initial photoluminescence intensity, F is defined as the photoluminescence intensity at a given concentration of added quencher, and K_{SV} is defined as the quenching factor or Stern–Volmer constant.

$$\frac{F_0}{F} = 1 + K_{SV}[Q] \tag{3.1}$$

Figure 3.4A illustrates that undoped quantum dots retain much of their initial luminescence intensity following addition of anthraquinone, indicating low rates of electron transfer relative to PL. However, both the Ag^+- and Cu^+-doped samples depicted in **Figure 3.4B** and **C**, respectively, show a marked decrease in their photoluminescence intensity following addition of anthraquinone, with the Cu^+-doped sample showing the greatest loss of photoluminescence in the series.

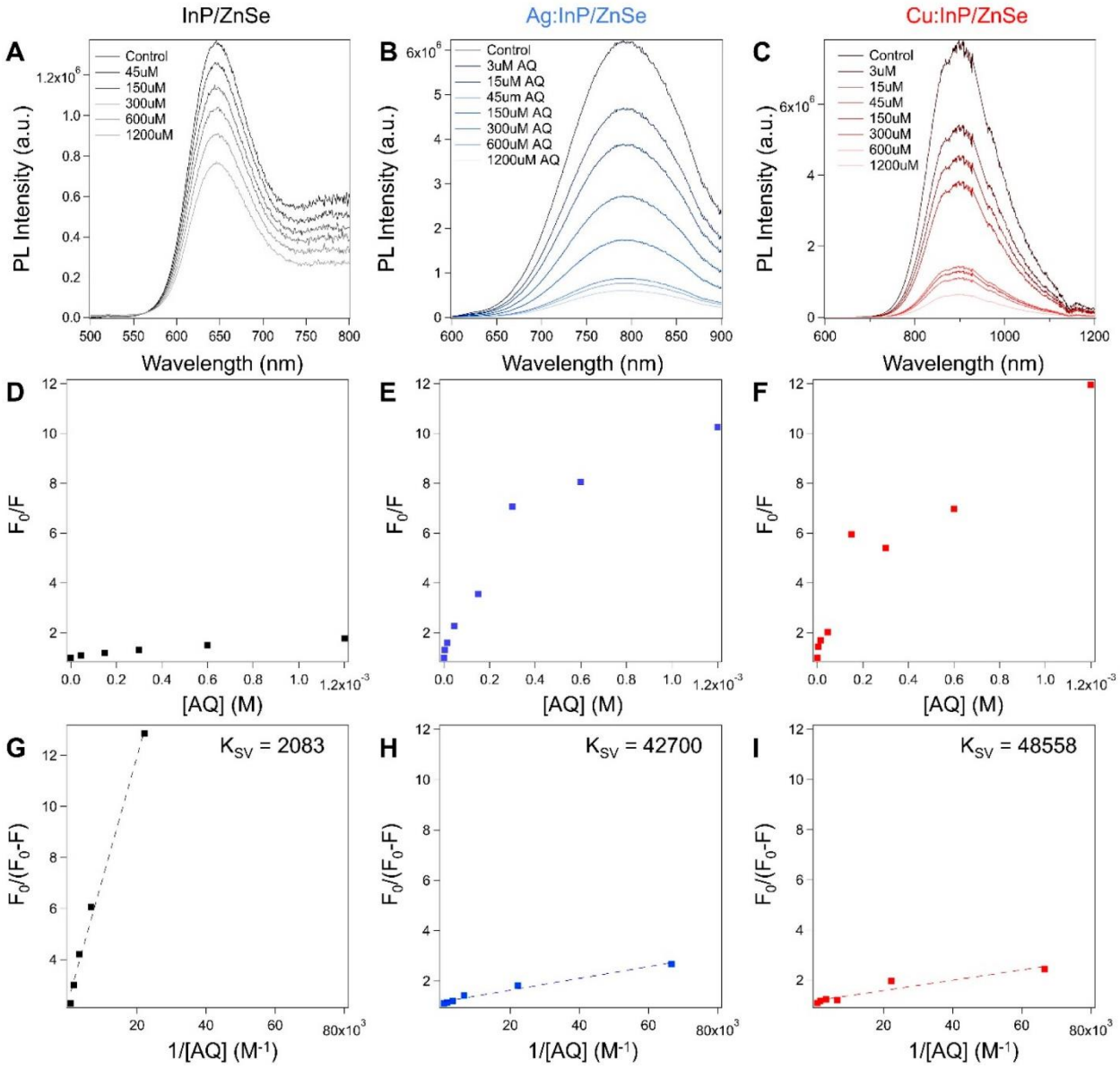

Figure 3.4. (A) PL quenching of InP/ZnSe QDs upon addition of anthraquinone. (B) PL quenching of Ag^{+}:InP/ZnSe QDs upon addition of anthraquinone. (C) PL quenching of Cu^{+}:InP/ZnSe QDs upon addition of anthraquinone. (D) Stern–Volmer plot of InP/ZnSe QDs. (E) Stern–Volmer plot of Ag+:InP/ZnSe QDs. (F) Stern–Volmer plot of Cu^{+}:InP/ZnSe. (G) Transformed Stern–Volmer plot of InP/ZnSe QDs. (H) Transformed Stern–Volmer plot of Ag^{+}:InP/ZnSe QDs. (I) Transformed Stern–Volmer plot of Cu^{+}:InP/ZnSe QDs.

Of note in these quenching experiments is the severe negative deviation from the linearity usually expected in simple Stern–Volmer behavior, as shown in **Figure 3.4D-F**. This negative deviation has been previously seen during fluorescence quenching of two different conformers of the same fluorophore.[33,34] A similar negative deviation has been observed in CdS QD/methyl viologen systems.[35] In the CdS system two mechanisms of adsorption of methyl viologen were proposed: one in which the acceptor directly associates with the quantum dot surface and one where a weakly bound surface metal ion and/or ligand species dissociates from the surface, followed by adsorption of the acceptor. This dissociation of bound surface ligands followed by adsorption of a new species has also been posited as the mechanism by which InP quantum dots lose under-passivated indium ions at their surfaces to increase photoluminescence quantum yield.[36] We hypothesize that a similar process occurs in our InP/ZnSe QDs, in which we see either direct adsorption of anthraquinone to the surface or dissociation of a zinc halide-oleylamine complex, followed by adsorption of the anthraquinone. As we observe that the negative deviation occurs at relatively low concentrations of anthraquinone, we suggest that the second mechanism, disassociation of a surface cation followed by adsorption of a quinone, dominates the interaction between the quantum dot and the electron acceptor.

To extract a singular K_{SV} from these data, we transform the data of **Figure 3.4D–F** using **Equation 3.2**. In **Equation 3.2**, F_0, F, and K_{SV} are defined as in eq 1, and f is defined as the fraction of accessible fluorophore and assumed to be 1.

$$\frac{F_0}{F_0 - F} = \frac{1}{f} + \frac{1}{f K_{SV}[Q]} \tag{3.2}$$

After applying this transformation to the PL quenching data, we see that the data can be fit to a single linear equation, as shown in **Figure 3.4G–I**. From these fits, we extract KSV values of 2083, 42700, and 48558 $mol^{-1} \cdot L$ for InP/ZnSe, Ag^+:InP/ZnSe, and Cu^+:InP/ZnSe QDs, respectively, showing an increase in charge transfer by over an order of magnitude for the doped quantum dot-anthraquinone systems. We attribute this enhancement to the extended excited state lifetimes in these doped materials.

3.3.3 Transient absorption spectroscopy of QD-AQ systems

To probe the photoinduced charge transfer to anthraquinone further, we turned to transient absorption spectroscopy to examine the bleach kinetics of the photoexcited quantum dots. Transient absorption spectroscopy allows us to examine the decay of the photogenerated conduction-band electron without major convolution from hole dynamics due to the degeneracy of holes at the valence band edge (undoped),[37] or deep localization of the holes (doped). Each of the quantum dots showed well-defined bleach features associated with the generation of a conduction band electron (**Figure 3.5A**). Furthermore, the kinetics of the bleach recovery are in good agreement with the decay dynamics observed in the time-resolved photoluminescence, as both Ag^+- and Cu^+-doped QDs show a longer charge separated state, with the Cu^+-doped InP/ZnSe QD decay being longer than the Ag^+-doped InP/ZnSe QD decay (**Figure 3.5B**). These results indicate that the photogenerated electrons in the doped QDs live much longer than in the undoped QDs.

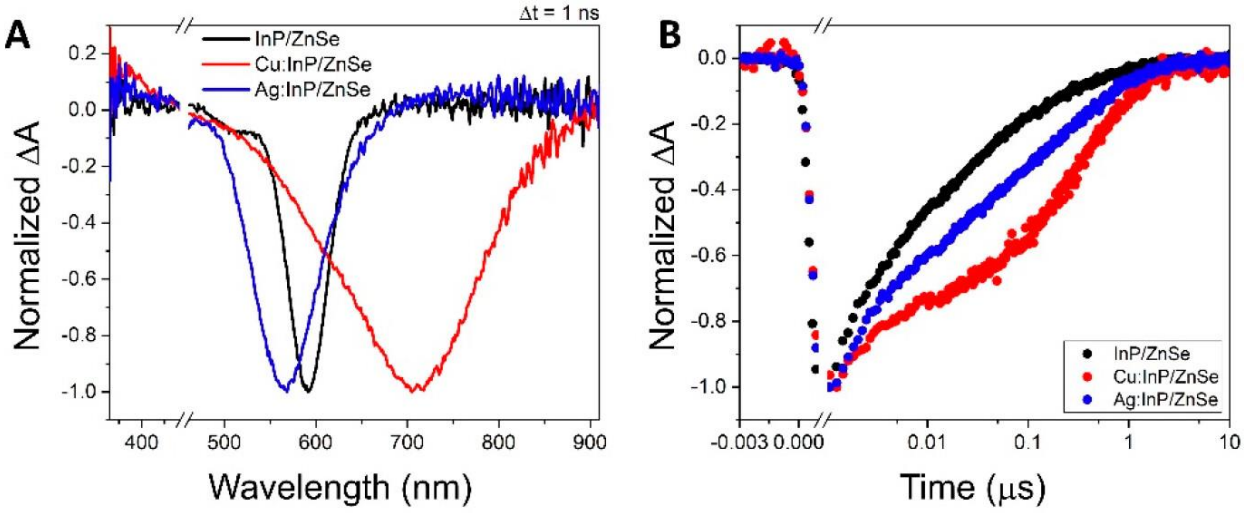

Figure 3.5. (A) Excitonic bleaches of InP/ZnSe, Ag^+:InP/ZnSe, and Cu^+:InP/ZnSe QDs. (B) Bleach-recovery kinetics of respective samples.

By examining the change in bleach recovery kinetics upon addition of anthraquinone, we can determine the relative amount of electron transfer in doped and undoped quantum dots (**Figure 3.6** and **Table 3.3-3.5**).

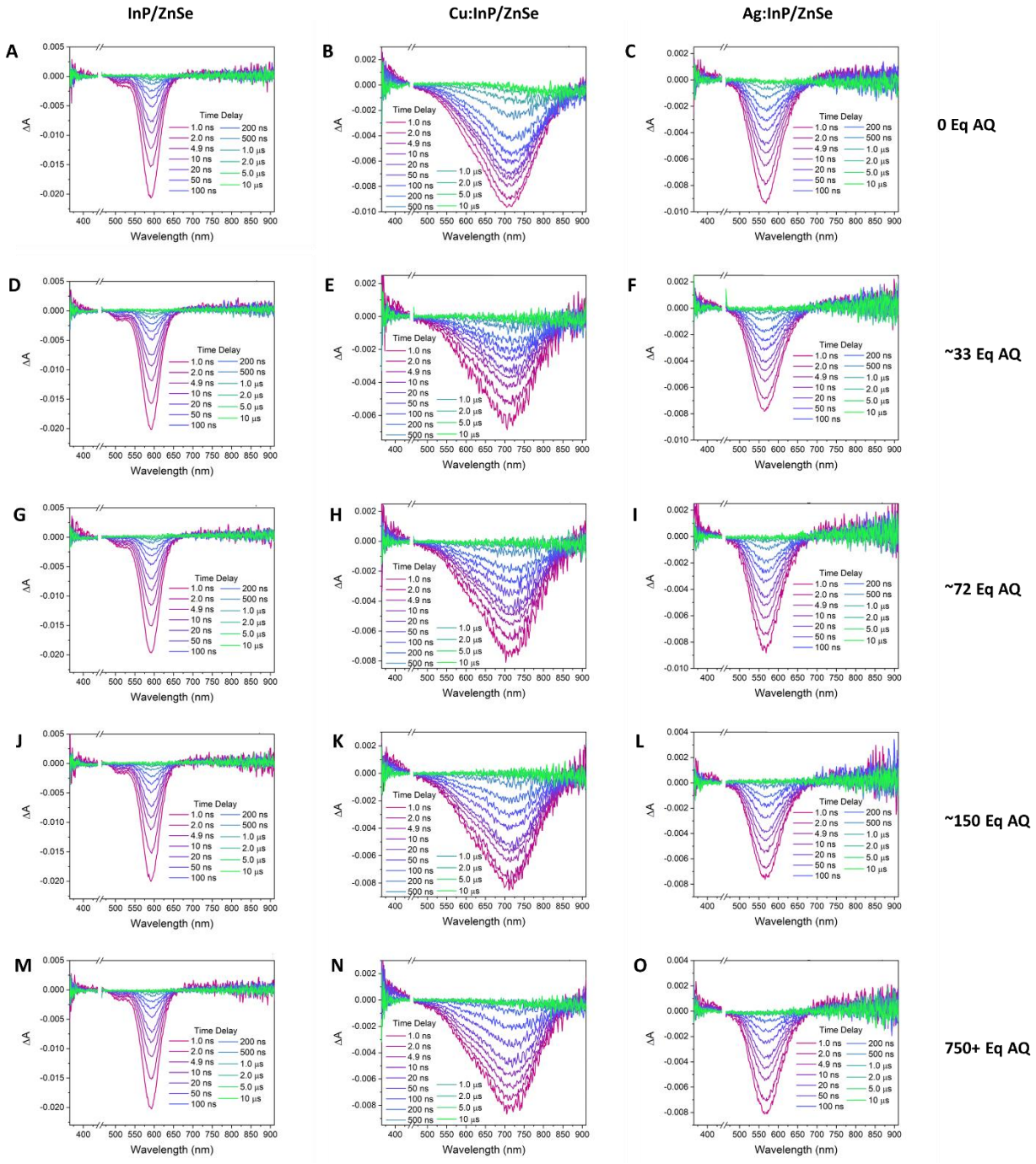

Figure 3.6. Transient absorption spectra of InP (column 1), Cu^{+}:InP/ZnSe (column 2), and Ag^{+}:InP/ZnSe (column 3), treated with 0 (row 1), 33 (row 2), 72 (row 3), 100-200 (row 4), and 750 (row 5) equivalents of anthraquinone.

Table 3.3. Lifetimes found via transient absorption spectroscopy of InP/ZnSe-AQ.

Sample	τ_1	τ_2	τ_3	τ_{ave}	k_{sve}
0 eq	1.9 ± 0.1 ns	30.2 ± 0.7 ns	470 ± 10 ns	90.2 ns	1.11 x 10^7
37 eq	1.8 ± 0.1 ns	26.0 ± 0.5 ns	348 ± 7 ns	70.5 ns	1.42 x 10^7
88 eq	1.6 ± 0.1 ns	24.5 ± 0.6 ns	324 ± 8 ns	63.6 ns	1.57 x 10^7
158 eq	1.5 ± 0.1 ns	27.6 ± 0.5 ns	383 ± 8 ns	72.2 ns	1.38 x 10^7
795 eq	1.8 ± 0.1 ns	29.0 ± 0.6 ns	422 ± 8 ns	78.3 ns	1.28 x 10^7

Table 3.4. Lifetimes found via transient absorption spectroscopy of Ag:InP/ZnSe-AQ.

Sample	τ_1	τ_2	τ_3	τ_{ave}	k_{sve}
0 eq	2.7 ± 0.1 ns	61 ± 2 ns	760 ± 10 ns	227 ns	4.39 x 10^6
32 eq	3.2 ± 0.1 ns	64 ± 2 ns	620 ± 20 ns	180 ns	5.56 x 10^6
63 eq	1.9 ± 0.1 ns	32 ± 1 ns	390 ± 7 ns	139 ns	7.22 s 10^6
177 eq	1.9 ± 0.1 ns	42 ± 2 ns	230 ± 10 ns	67 ns	1.50 x 10^7
744 eq	1.8 ± 0.1 ns	18 ± 1 ns	131 ± 3 ns	49 ns	2.06 x 10^7

Table 3.5. Lifetimes found via transient absorption spectroscopy of Cu:InP/ZnSe-AQ.

Sample	τ_1	τ_2	τ_3	τ_{ave}	k_{sve}
0 eq	2 ± 0.1 ns	62 ± 2 ns	554 ± 6 ns	279 ns	3.58×10^6
33 eq	1.5 ± 0.1 ns	32 ± 1 ns	366 ± 6 ns	138 ns	7.26×10^6
72 eq	1.5 ± 0.1 ns	54 ± 1 ns	470 ± 10 ns	165 ns	6.08×10^6
108 eq	1.6 ± 0.1 ns	42 ± 1 ns	291 ± 4 ns	129 ns	7.77×10^6
775 eq	1.2 ± 0.1 ns	19.4 ± 0.9 ns	95 ± 2 ns	44 ns	2.25×10^7

As previously shown by Zhu et al., electron transfer in quantum dot-anthraquinone systems occurs on the picosecond time scale with recombination to the ground state occurring in a few ns.[38] By monitoring the shortening of the excitonic bleach, we are able to determine if the major process occurring is excited-state recombination or charge separation followed by recombination from the quinone. Upon the addition of approximately 770 equivalents of anthraquinone to undoped InP/ZnSe QDs, we see that the change in the recovery dynamics is negligible (**Figure 3.7A**), indicating that exciton recombination is the preferred pathway for excited state relaxation. In contrast, the Ag^+- and Cu^+-doped InP/ZnSe QDs show large changes in the recovery dynamics (**Figure 3.7**B and C) upon the addition of the same amount of anthraquinone. **Figure 3.7**D compares the three systems and shows that both Ag^+ and Cu^+ doped QDs outperform undoped QDs by over an order of magnitude in transferring electrons to the anthraquinone acceptor, in good agreement with the photoluminescence quenching results (**Table 3.3**-**Table 3.5**).

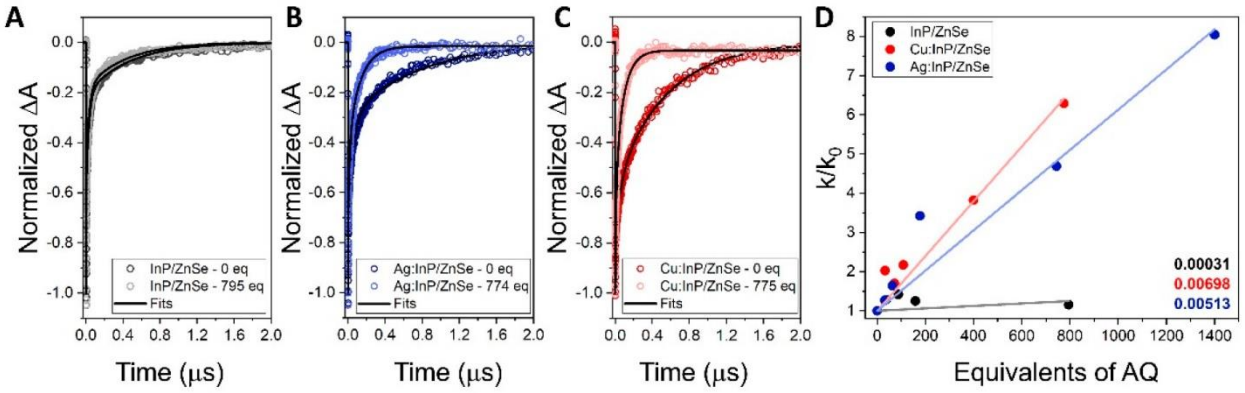

Figure 3.7. Bleach recovery dynamics of (A) InP/ZnSe, (B) Ag^+:InP/ZnSe, and (C) Cu^+:InP/ZnSe QDs with 0 equivalents of anthraquinone and ~770 equivalents of anthraquinone (2.34e–4 M). (D) Comparison of bleach recovery rate constants (k) relative to the original recovery rate constant (k_0). Inset are slopes of each fit.

3.3.4 Photoluminescence Quenching Modulated by Acceptor Size

To test the proposed dependence of electron transfer on the surface desorption/acceptor adsorption mechanism described for anthraquinone, we examined PL quenching by electron acceptors of varying sizes, including naphthoquinone and benzoquinone. By using smaller acceptor molecules, the more dominant pathway is expected to shift toward a simple adsorption mechanism, leading to increased PL quenching with all quantum dots. We began these studies by monitoring PL quenching in the quantum dot-benzoquinone system, shown in **Figure 3.8**A–C. Not only did we observe much more PL quenching, we also observed greater linearity in the resulting Stern–Volmer plots, **Figure 3.8**D–F, suggesting that the mechanism shifts toward a simple adsorption process. From these data, we extract K_{SV} values for InP/ZnSe-benzoquinone, Ag^+:InP/ZnSe-benzoquinone, and Cu^+:InP/ZnSe-benzoquinone of 26744, 28149, and 62055 mol^{-1}·L, respectively. Notably, upon the addition of higher equivalents of benzoquinone we see

the nonlinear deviation begin, suggesting that while the simple adsorption mechanism is most prevalent, the displacement mechanism occurs once all easily available surface sites on the QD are occupied.

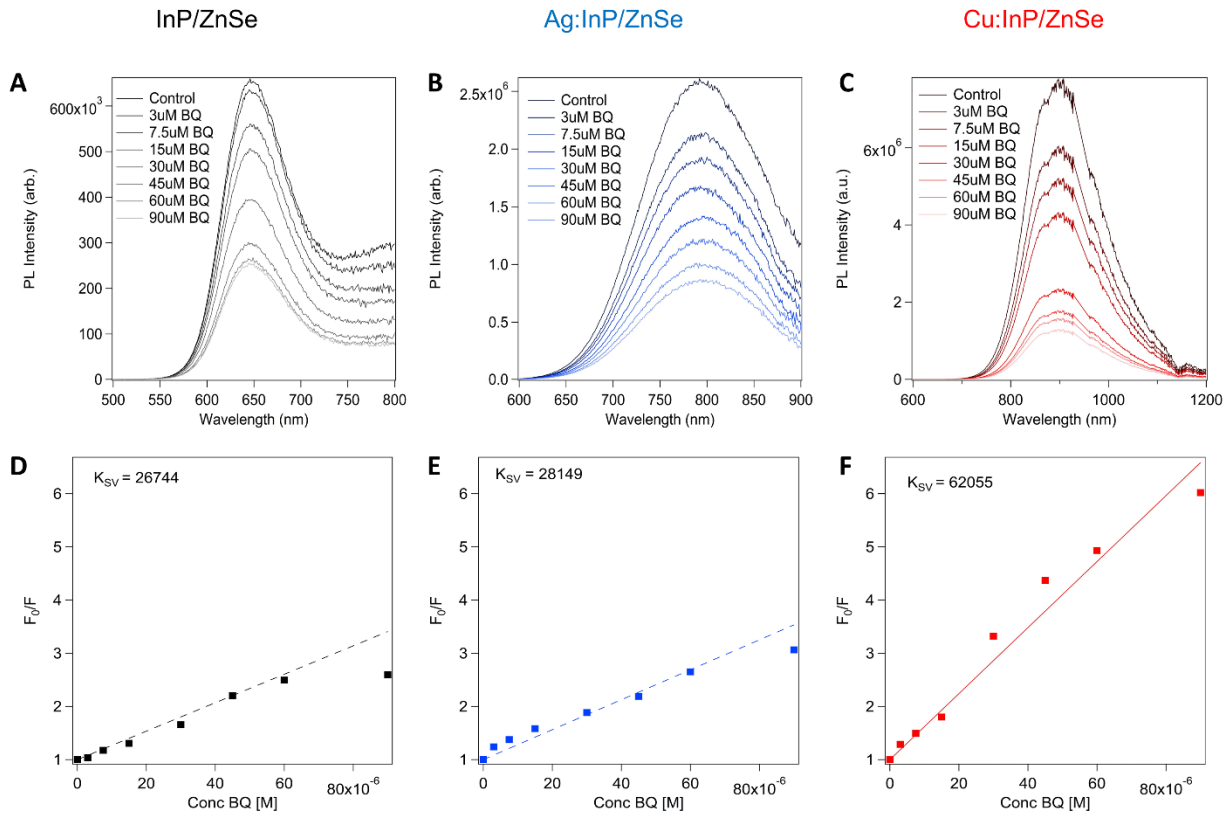

Figure 3.8. (A) PL quenching of InP/ZnSe QDs with addition of benzoquinone. (B) PL quenching of Ag^+:InP/ZnSe QDs with addition of benzoquinone. (C) PL quenching of Cu^+:InP/ZnSe QDs with addition of benzoquinone. (D) Stern–Volmer plot of InP/ZnSe QDs with benzoquinone. (E) Stern–Volmer plot of Ag^+:InP/ZnSe QDs with benzoquinone. (F) Stern–Volmer plot of Cu^+:InP/ZnSe QDs with benzoquinone.

Additionally, we see negligible changes between losses in the excited state lifetime when comparing doped and undoped quantum dots with adsorbed benzoquinone, indicating both species are undergoing electron transfer on similar time scales with small acceptors (**Figure 3.9**, **Table 3.6-Table 3.8**).

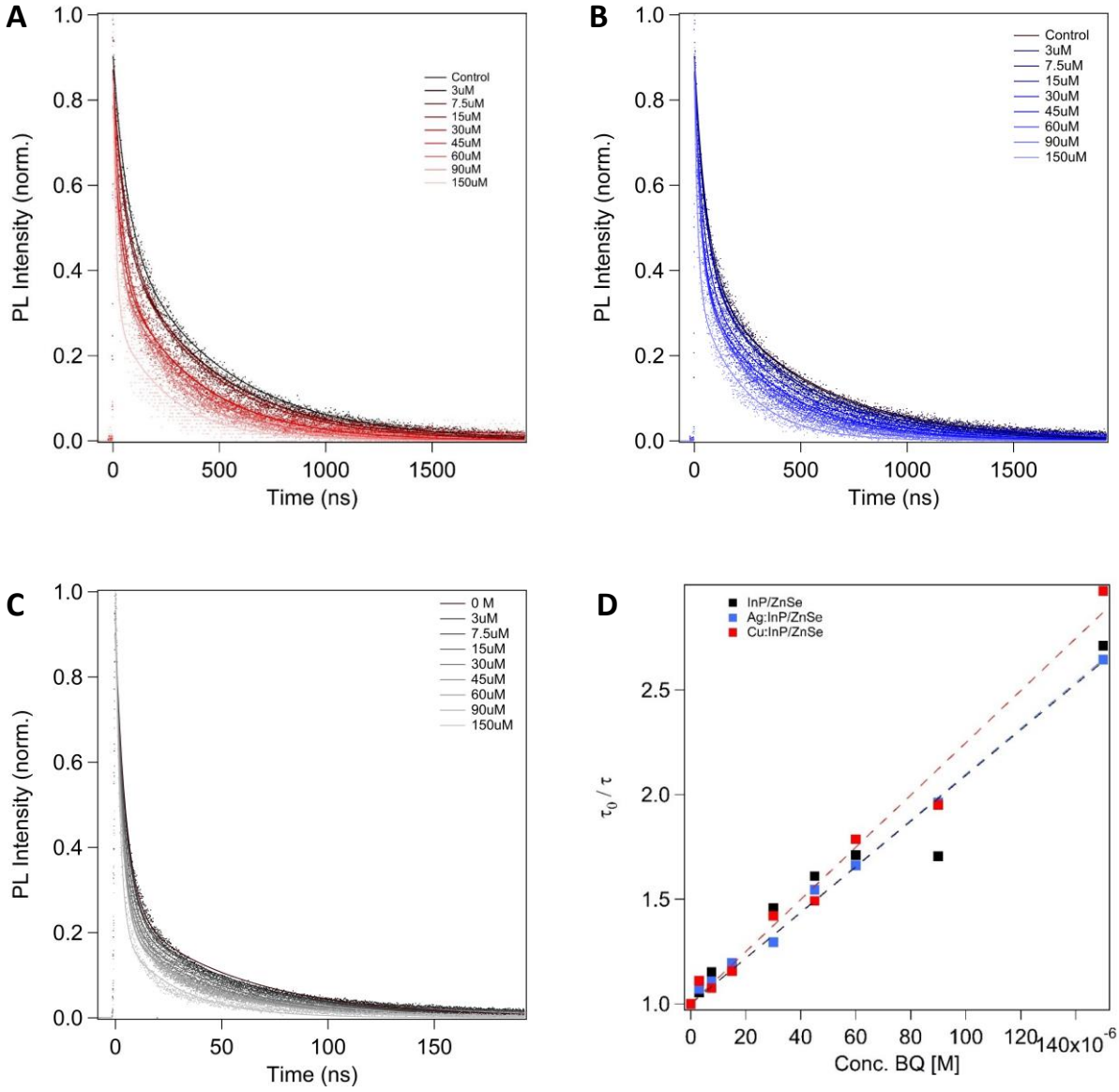

Figure 3.9. TRPL decay traces of A) Cu^{+}:InP/ZnSe, B) Ag^{+}:InP/ZnSe, and C) InP/ZnSe with added benzoquinone. D) Comparison of lifetimes for each system relative to added BQ.

Table 3.6. Time constants for Cu^{+}:InP/ZnSe with added BQ.

	A1	**τ 1**	**A2**	**τ2**	**$\tau_{weighted}$**
0 µM BQ	0.41068 ± 0.0054	66.694 ± 1.73	0.49291 ± 0.00476	482.23 ± 3.99	293.36
3 µM BQ	0.39727 ± 0.00554	47.919 ± 1.33	0.47481 ± 0.00393	445.31 ± 3.49	264.28
7.5 µM BQ	0.38511 ± 0.00592	60.524 ± 1.85	0.46704 ± 0.00512	447.8 ± 4.24	272.78
15 µM BQ	0.38099 ± 0.00597	50.559 ± 1.59	0.48021 ± 0.00473	414.77 ± 3.69	253.65
30 µM BQ	0.38211 ± 0.00599	33.48 ± 1.02	0.40513 ± 0.00355	369.85 ± 3.25	206.58
45 µM BQ	0.44259 ± 0.00615	40.693 ± 1.13	0.40262 ± 0.00442	367.93 ± 3.77	196.57
60 µM BQ	0.4513 ± 0.00689	22.67 ± 0.645	0.40884 ± 0.00324	320.37 ± 2.73	164.17
90 µM BQ	0.40328 ± 0.00619	24.349 ± 0.727	0.41297 ± 0.00363	273.41 ± 2.42	150.36
150 µM BQ	0.55483 ± 0.0121	14.992 ± 0.593	0.2909 ± 0.00483	258.29 ± 4.84	98.68

Table 3.7. Time constants for Ag^{+}:InP/ZnSe with added BQ.

	A1	**τ 1**	**A2**	**τ2**	**$\tau_{weighted}$**
0 µM BQ	0.46261 ± 0.00515	60.931 ± 1.36	0.39733 ± 0.00402	512.31 ± 4.76	269.49
3 µM BQ	0.49802 ± 0.00548	56.351 ± 1.24	0.40555 ± 0.00413	491.26 ± 4.65	251.55
7.5 µM BQ	0.46818 ± 0.00556	55.933 ± 1.33	0.39879 ± 0.00438	462.91 ± 4.62	243.14
15 µM BQ	0.4843 ± 0.00579	50.469 ± 1.21	0.40976 ± 0.00442	431.78 ± 4.28	225.23
30 µM BQ	0.44832 ± 0.00498	45.401 ± 1.01	0.38299 ± 0.00368	398.48 ± 3.54	208.07
45 µM BQ	0.48728 ± 0.00518	34.314 ± 0.715	0.36844 ± 0.00323	359.69 ± 3.11	174.41
60 µM BQ	0.49882 ± 0.00508	34.034 ± 0.684	0.36055 ± 0.00332	339.4 ± 3.03	162.15
90 µM BQ	0.49107 ± 0.0057	26.05 ± 0.594	0.40604 ± 0.00358	272.06 ± 2.36	137.39
150 µM BQ	0.49571 ± 0.00698	16.482 ± 0.439	0.34958 ± 0.00346	223.01 ± 2.35	101.89

Table 3.8. Time constants for InP/ZnSe with added BQ.

	A1	**τ 1**	**A2**	**τ2**	**$\tau_{weighted}$**
0 µM BQ	0.6428 ± 0.00456	4.945 ± 0.0685	0.26152 ± 0.00272	55.721 ± 0.594	19.63
3 µM BQ	0.63624 ± 0.00453	4.8261 ± 0.0674	0.25339 ± 0.00275	53.235 ± 0.587	18.61
7.5 µM BQ	0.67232 ± 0.00481	4.3686 ± 0.0608	0.25747 ± 0.00281	50.079 ± 0.558	17.02
15 µM BQ	0.64531 ± 0.00453	4.3109 ± 0.0589	0.24081 ± 0.00265	49.213 ± 0.553	16.51
30 µM BQ	0.7227 ± 0.00382	0.7227 ± 0.00382	0.2372 ± 0.00204	43.674 ± 0.39	13.47
45 µM BQ	0.7162 ± 0.00394	3.1804 ± 0.0333	0.2318 ± 0.00206	40.039 ± 0.371	12.19
60 µM BQ	0.70793 ± 0.00392	3.0777 ± 0.0324	0.21921 ± 0.00206	38.56 ± 0.377	11.47
90 µM BQ	0.68149 ± 0.00377	3.053 ± 0.0322	0.21683 ± 0.00199	38.074 ± 0.363	11.51
150 µM BQ	0.79083 ± 0.00429	2.1424 ± 0.0221	0.20216 ± 0.00224	27.19 ± 0.315	7.24

We next examined PL quenching by naphthoquinone. As it is larger than benzoquinone but smaller than anthraquinone, one would expect the K_{SV} values for these systems to be intermediate to the previously explored quinones, which is what is observed experimentally (**Figure 3.10G**–**I**). All three samples in the series show higher quenching than with anthraquinone but lower than with benzoquinone, with K_{SV} values for undoped, Ag^{+}-doped, and Cu^{+}-doped InP/ZnSe QDs of 18991, 27076, and 44764 $mol^{-1}\cdot L$, respectively (**Figure 3.10J–L**). Interestingly, quantum dot-naphthoquinone systems exhibit nonlinear deviations at higher quencher concentrations than anthraquinone but earlier than benzoquinone, further supporting the interpretation that the size of the acceptor molecule greatly influences the mechanism of adsorption, and hence of electron transfer.

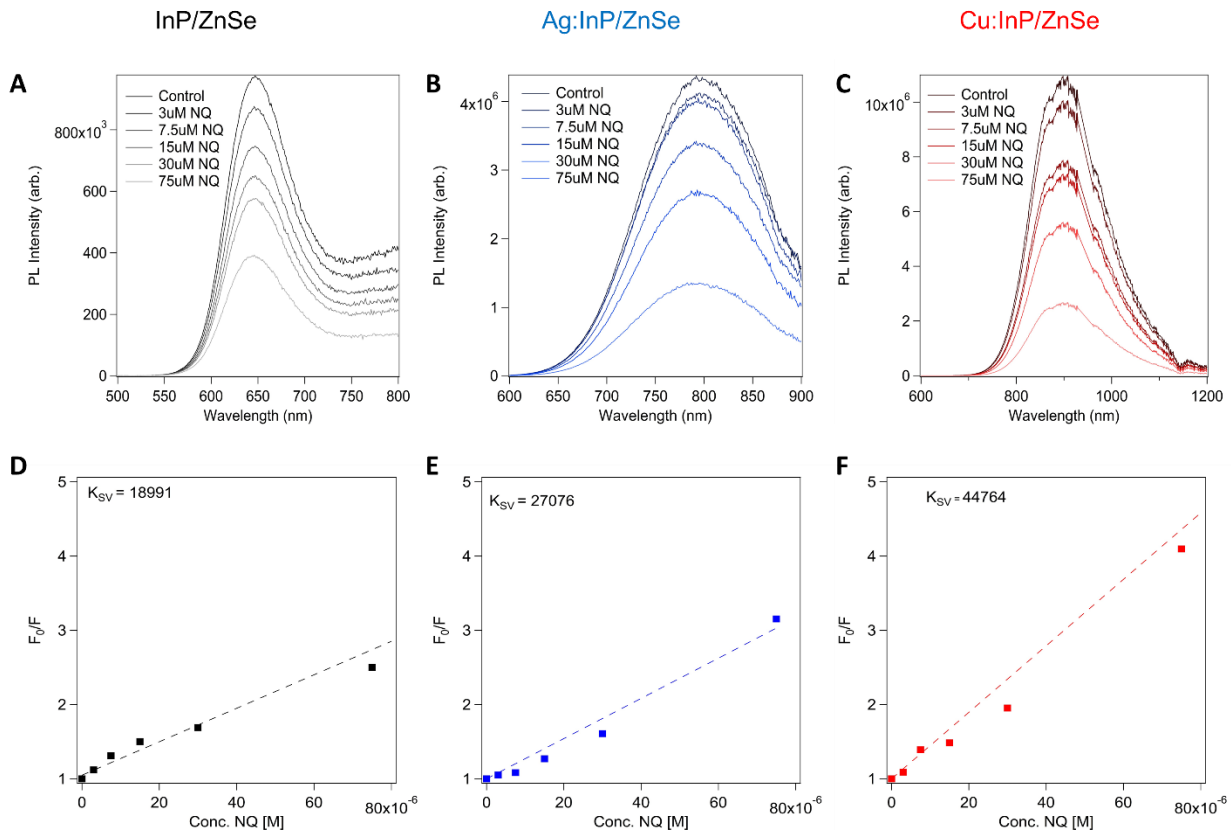

Figure 3.10. (A) PL quenching of InP/ZnSe QDs with the addition of naphthoquinone. (B) PL quenching of Ag^+:InP/ZnSe QDs with the addition of naphthoquinone. (C) PL quenching of Cu^+:InP/ZnSe QDs with addition of naphthoquinone. (D) Stern–Volmer plot of InP/ZnSe QDs with naphthoquinone. (E) Stern–Volmer plot of Ag^+:InP/ZnSe QDs with naphthoquinone. (F) Stern–Volmer plot of Cu^+:InP/ZnSe QDs with naphthoquinone.

Finally, methyl viologen was investigated, as it is a well-known electron acceptor in QD-molecular systems, showing ultrafast electron transfer.[39–42] While the size of the methyl viologen is similar to that of anthraquinone, its reduction potential is much larger. Therefore, the study of methyl viologen as an electron acceptor allows determination of whether electron transfer is more impacted by the adsorption mechanism of the acceptor or by driving force. Upon addition of methyl viologen, we once again see remarkable charge transfer enhancement when comparing

doped and undoped InP/ZnSe quantum dots (**Figure 3.11A–C**). Similar to other acceptors explored here, Ag^+-doped InP/ZnSe QDs show enhanced electron transfer in comparison to undoped quantum dots but lower charge transfer than Cu^+-doped InP/ZnSe QDs with K_{SV} values of 12647, 49147, and 93454 $mol^{-1} \cdot L$ for InP/ZnSe, Ag^+:InP/ZnSe, and Cu^+:InP/ZnSe, respectively (**Figure 3.11D–F**).

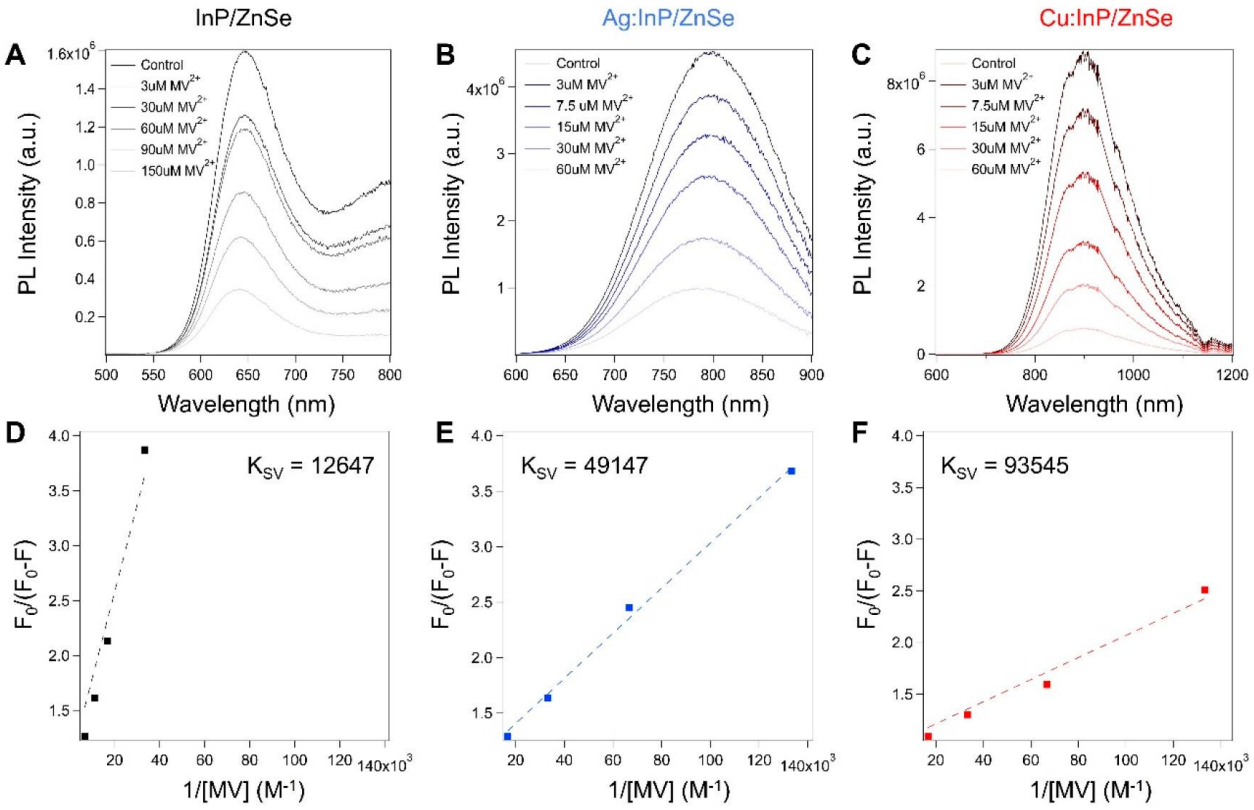

Figure 3.11. Photoluminescence quenching of (A) InP/ZnSe QDs, (B) Ag^+:InP/ZnSe QDs, and (C) Cu^+:InP/ZnSe QDs in the presence of methyl viologen. (D) Transformed Stern–Volmer plot of InP/ZnSe QDs. (E) Transformed Stern–Volmer plot of Ag^+:InP/ZnSe QDs. (F) Transformed Stern–Volmer plot of Cu^+:InP/ZnSe QDs.

While the K_{SV} values are larger than those for the anthraquinone systems, the overall trend is the same, with Cu^{+}-doped QDs showing almost an order of magnitude enhancement in electron transfer. We therefore attribute the increased K_{SV} values to the higher driving force for electron transfer to methyl viologen than anthraquinone. By examining a comparison of reduction potential vs K_{SV} we see that the larger acceptors show over an order of magnitude increase between the undoped and doped species when compared to a sample with similar reduction potential (**Figure 3.12**).

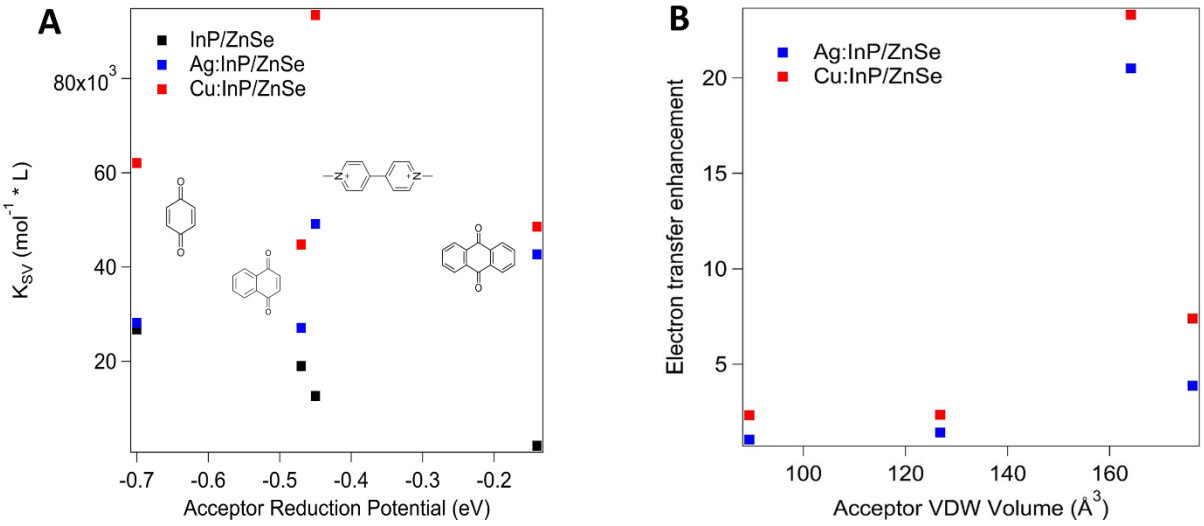

Figure 3.12. A) Comparison of K_{SV} to acceptor reduction potential. B) Comparison of electron transfer enhancement (K_{SV}(doped)/K_{SV}(undoped)) relative to size.

Additionally, we see that Cu^{+}-doped species outperform Ag^{+}-doped species in all cases, which we attribute to the more highly localized hole at the band edges, and thus, the reducing potential of both species is nearly identical (**Figure 3.13**).

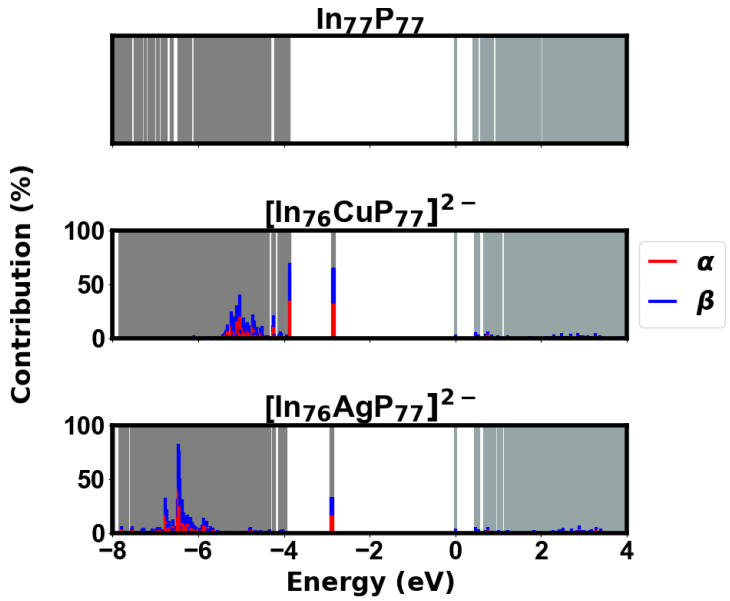

Figure 3.13. Calculated molecular orbitals for undoped and doped model clusters.

3.3.5 Conclusions

In this work, we have found that coinage-metal-doped InP quantum dots show remarkably enhanced electron transfer to a wide variety of electron acceptors compared to undoped InP/ZnSe quantum dots. Through ab initio DFT calculations, we confirm the assignment of hole localization to the dopant, with increased structural distortion and elevated hole and electron localization for Cu^{+}- versus Ag^{+}-doped QDs. Analysis of photoluminescence quenching shows that electron transfer is enhanced by over an order of magnitude when the quantum dot is paired with a bulky acceptor such as anthraquinone. By changing the size of our electron acceptors, we are able to preferentially choose the dominant adsorption pathway of the electron acceptor as either direct adsorption or ligand dissociation, followed by adsorption. With acceptors that require ligand dissociation, the long-lived excited state lifetimes generated by dopants were found to be necessary for efficient electron transfer, and larger differences between doped and undoped quantum dots are observed. However, when small acceptors were added, the difference

in the electron transfer between doped and undoped quantum dots is smaller. Transient absorption spectroscopy was performed to examine the electron dynamics in these systems, showing greatly enhanced lifetimes of photogenerated conduction band electrons in the doped QDs, consistent with the formation of an emissive charge transfer excited state. This work provides new insight into the role of dopant-induced wave function localization on charge transfer from quantum dot photosensitizers, paving the way for improved design and implementation of these materials as photoredox catalysts.

3.4 Experimental Details

3.4.1 General considerations and materials

All glassware was dried in a 160 °C oven overnight prior to use. All reactions were run under an inert atmosphere of nitrogen using a glovebox or standard Schlenk techniques. Zinc chloride (>98%), tris-diethylaminophosphine (97%), copper(II) chloride (≥98%), indium(III) chloride (97%), silver(I) chloride (99%), and anhydrous ethanol were purchased from Millipore-Sigma, stored in a nitrogen glovebox or desiccator, and used without further purification. Anthraquinone, benzoquinone, naphthoquinone, and methyl viologen dichloride were purchased from Milipore-Sigma and stored in an inert atmosphere glovebox. Methyl viologen diiodide was formed via salt metathesis from methyl viologen dichloride. ([43])

Oleylamine and toluene, which were purchased from Milipore-Sigma, were dried over CaH2, distilled, and stored over 4 Å sieves in a nitrogen glovebox. Omni Trace nitric acid was purchased from EMD Millipore and used without purification. Water, 18.2 MΩ, was collected from an EMD Millipore water purification system.

3.4.2 Synthesis of InP/ZnSe, Ag^+:InP/ZnSe, and Cu^+:InP/ZnSe Quantum Dots

0.23 mmol portion of an indium halide, 1.1 mmol of $ZnCl_2$, and 2.5 mL of dried and distilled oleylamine were added to a 15 mL 3-neck flask. The solution was then placed under vacuum at 120 °C and degassed for 1 h. The vessel was then placed under an inert atmosphere and heated to 180 °C. Once the reaction temperature was reached, 0.23 mL of tris-diethylaminophosphine (0.8 mmol) was rapidly injected. The reaction was allowed to proceed for 20 min, after which 0.5 mL of previously prepared 1 M TOP=Se was slowly injected. At 60 min, the temperature was increased to 200 °C and held there for an additional 60 min. The flask was then cooled down to room temperature before being moved into a nitrogen glovebox for purification. The nanocrystals were precipitated with anhydrous ethanol, centrifuged at 7830 rpm, and suspended in toluene. This procedure was repeated 5 times before any additional sample analysis was performed.

Doped samples were synthesized following the same method as above. However, 120 min after TOP=Se addition, the temperature was decreased to 150 °C. Once this temperature was reached, the copper halide ($CuCl_2$) or silver halide (AgCl) solution was slowly injected (1 mL at 2 mL/h). After the injection had completed, the temperature was increased to 210 °C and held there for 1.5 h. Purification procedures remained the same as those for the undoped samples.

3.4.3 Characterization techniques

UV–vis absorption spectroscopy was carried out using an Agilent Cary 5000 spectrophotometer. Photoluminescence spectroscopy was performed using an Edinburgh FLS 1000 Fluorimeter located in the University of Washington's MEM-C shared user facility.

Concentrations of QD solutions were set to 300 nM via dilution as determined using the method developed in ref (10).

For quenching experiments, samples were cycled into an inert atmosphere glovebox, and microliter volumes of toluene solutions containing the electron acceptor were added to avoid convolution from large dilution effects (the concentration of the added solution of electron acceptor was 10 mM (from the range of 3 μM to 45 μM) or 100 mM (more than 45 μM acceptor added). The total added volume of solvent in any sample did not exceed 100 μL. Excitation for quantum dot/anthraquinone systems occurred at 450 nm to avoid co-excitation. Quantum dot/benzoquinone, quantum dot/naphthoquinone, and quantum dot/methyl viologen systems were all excited at 402 nm. Preparation of the QD-MV^{2+} system varied from other quenching experiment preparations due to the insolubility of MV^{2+} in common organic solvents. Instead, methyl viologen diiodide was suspended in dry methanol and sonicated before being brought back into an inert atmosphere glovebox and added to the quantum dot solution.[44]

Powder X-ray diffraction data were recorded on a Bruker D8 Discover instrument with the IμS 2-D XRD system at the University of Washington's Molecular Analysis Facility. TEM images were obtained on an FEI Tecnai G2 F20 microscope at the University of Washington's Molecular Analysis Facility. TEM samples were prepared by spotting 5 μL of a dilute solution of QDs dispersed in toluene onto an ultrathin carbon on a holey carbon support film purchased from Ted Pella. A PerkinElmer Optima 8300 inductively coupled plasma–optical emission spectrophotometer was used for elemental analysis.

3.4.4 Computational Methods

Quasi-spherical InP quantum dots, $In_{77}P_{77}$ (diameter ~2 nm), were constructed using the bulk Zinc Blende crystal structure. The undoped structure conformed to C_{3v} symmetry before optimization. Doped structures were built from the InP core by replacing one In center with a dopant atom to form $In_{76}MP_{77}$ ($M = Cu^+, Ag^+$). Ground-state geometric optimizations were performed, and the structures were considered optimized when both the forces [maximum and root-mean-square (rms) of the force 0.000450 and 0.000300 hartree/Bohr, respectively] and displacement [maximum and rms displacement 0.00018 and 0.0012 Bohr, respectively] values were below the threshold criteria. Surface dangling bonds were terminated using a pseudohydrogen capping scheme to compensate surface ions (±1/3 to passivate the In/P ions, respectively) resulting in an $In_{77}P_{77}H_{108}$ structure for the pure, non-doped system. In order to maintain a proper charge on the M^+ ion, the doped systems have an overall charge of (−2). Similar methods have been used in previous studies on doped semiconductor nanocrystals.[18,45−47] These systems are expected to exhibit quantum confinement (Bohr exciton radius is 10 nm for InP [48]); however, the diameters of the prepared dots are similar to those able to be created experimentally.[49] Calculations were conducted using the Gaussian software package[50] using the Perdew, Burke, and Ernzerhof hybrid functional (PBE0)[51−53] to compute the Kohn–Sham ground-state electronic structure. The Los Alamos National Lab 2-Double Zeta (LANL2DZ) pseudopotential and associated basis sets was used.[54−57] This combination is able to fairly accurately reproduce the experimentally observed 3.7 eV band gap (computational gap is 3.89 eV, + 5% in relation to experiment).[47,49] The electronic structures of excited states were calculated using time-dependent DFT (TD-DFT) within the linear-response framework.[58−60]

Transient Absorption Measurements

Transient absorption measurements were performed using an EOS unit from Ultrafast Systems at the University of Washington's Molecular Analysis Facility. The pump wavelength of 450 nm was chosen to avoid coexcitation of the quinone acceptor. It was generated via a Coherent Inc./Light Source OPerA optical parametric amplifier, with a power of 400 μW measured through a 200 μm pinhole. The probe white light was generated by using an external Q-switched Nd:YAG laser with an electronic delay. The collinear pump and probe beams overlapped with the sample.

3.5 REFERENCES

(1) Nakajima, T.; Tamaki, Y.; Ueno, K.; Kato, E.; Nishikawa, T.; Ohkubo, K.; Yamazaki, Y.; Morimoto, T.; Ishitani, O. Photocatalytic Reduction of Low Concentration of CO2. *J. Am. Chem. Soc.* **2016**, *138* (42), 13818–13821. https://doi.org/10.1021/jacs.6b08824.

(2) Sahara, G.; Kumagai, H.; Maeda, K.; Kaeffer, N.; Artero, V.; Higashi, M.; Abe, R.; Ishitani, O. Photoelectrochemical Reduction of CO2 Coupled to Water Oxidation Using a Photocathode with a Ru(II)–Re(I) Complex Photocatalyst and a CoOx/TaON Photoanode. *J. Am. Chem. Soc.* **2016**, *138* (42), 14152–14158. https://doi.org/10.1021/jacs.6b09212.

(3) Brus, L. Electronic Wave Functions in Semiconductor Clusters: Experiment and Theory. *J. Phys. Chem.* **1986**, *90* (12), 2555–2560. https://doi.org/10.1021/j100403a003.

(4) Toufanian, R.; Chern, M.; Kong, V. H.; Dennis, A. M. Engineering Brightness-Matched Indium Phosphide Quantum Dots. *Chem. Mater.* **2021**, *33* (6), 1964–1975. https://doi.org/10.1021/acs.chemmater.0c03181.

(5) Peng, X.; Schlamp, M. C.; Kadavanich, A. V.; Alivisatos, A. P. Epitaxial Growth of Highly Luminescent CdSe/CdS Core/Shell Nanocrystals with Photostability and Electronic Accessibility. *J. Am. Chem. Soc.* **1997**, *119* (30), 7019–7029. https://doi.org/10.1021/ja970754m.

(6) Lim, J.; Bae, W. K.; Lee, D.; Nam, M. K.; Jung, J.; Lee, C.; Char, K.; Lee, S. InP@ZnSeS, Core@Composition Gradient Shell Quantum Dots with Enhanced Stability. *Chem. Mater.* **2011**, *23* (20), 4459–4463. https://doi.org/10.1021/cm201550w.

(7) Murcia, M. J.; Shaw, D. L.; Woodruff, H.; Naumann, C. A.; Young, B. A.; Long, E. C. Facile Sonochemical Synthesis of Highly Luminescent ZnS−Shelled CdSe Quantum Dots. *Chem. Mater.* **2006**, *18* (9), 2219–2225. https://doi.org/10.1021/cm0505547.

(8) Hughes, K. E.; Stein, J. L.; Friedfeld, M. R.; Cossairt, B. M.; Gamelin, D. R. Effects of Surface Chemistry on the Photophysics of Colloidal InP Nanocrystals. *ACS Nano* **2019**, *13* (12), 14198–14207. https://doi.org/10.1021/acsnano.9b07027.

(9) Kirkwood, N.; Monchen, J. O. V.; Crisp, R. W.; Grimaldi, G.; Bergstein, H. A. C.; du Fossé, I.; van der Stam, W.; Infante, I.; Houtepen, A. J. Finding and Fixing Traps in II–VI and III–V Colloidal Quantum Dots: The Importance of Z-Type Ligand Passivation. *J. Am. Chem. Soc.* **2018**, *140* (46), 15712–15723. https://doi.org/10.1021/jacs.8b07783.

(10) Reiss, P.; Protière, M.; Li, L. Core/Shell Semiconductor Nanocrystals. *Small* **2009**, *5* (2), 154–168. https://doi.org/10.1002/smll.200800841.

(11) Mićić, O. I.; Sprague, J.; Lu, Z.; Nozik, A. J. Highly Efficient Band-edge Emission from InP Quantum Dots. *Appl. Phys. Lett.* **1996**, *68* (22), 3150–3152. https://doi.org/10.1063/1.115807.

(12) Jones, M.; Nedeljkovic, J.; Ellingson, R. J.; Nozik, A. J.; Rumbles, G. Photoenhancement of Luminescence in Colloidal CdSe Quantum Dot Solutions. *J. Phys. Chem. B* **2003**, *107* (41), 11346–11352. https://doi.org/10.1021/jp035598m

(13) Jiang, Y.; Wang, C.; Rogers, C. R.; Kodaimati, M. S.; Weiss, E. A. Regio- and Diastereoselective Intermolecular [2+2] Cycloadditions Photocatalysed by Quantum Dots. *Nat. Chem.* **2019**, *11* (11), 1034–1040. https://doi.org/10.1038/s41557-019-0344-4.

(14) Jones, L. O.; Mosquera, M. A.; Jiang, Y.; Weiss, E. A.; Schatz, G. C.; Ratner, M. A. Thermodynamics and Mechanism of a Photocatalyzed Stereoselective [2 + 2] Cycloaddition on a CdSe Quantum Dot. *J. Am. Chem. Soc.* **2020**, *142* (36), 15488–15495. https://doi.org/10.1021/jacs.0c07130.

(15) Yu, S.; Fan, X.-B.; Wang, X.; Li, J.; Zhang, Q.; Xia, A.; Wei, S.; Wu, L.-Z.; Zhou, Y.; Patzke, G. R. Efficient Photocatalytic Hydrogen Evolution with Ligand Engineered All-Inorganic InP and InP/ZnS Colloidal Quantum Dots. *Nat Commun* **2018**, *9* (1), 4009. https://doi.org/10.1038/s41467-018-06294-y.

(16) Han, Z.; Qiu, F.; Eisenberg, R.; Holland, P. L.; Krauss, T. D. Robust Photogeneration of H2 in Water Using Semiconductor Nanocrystals and a Nickel Catalyst. *Science* **2012**, *338* (6112), 1321–1324. https://doi.org/10.1126/science.1227775.

(17) Knowles, K. E.; Nelson, H. D.; Kilburn, T. B.; Gamelin, D. R. *Singlet–Triplet Splittings in the Luminescent Excited States of Colloidal Cu+:CdSe, Cu+:InP, and CuInS2 Nanocrystals: Charge-Transfer Configurations and Self-Trapped Excitons*. https://doi.org/10.1021/jacs.5b08547.

(18) Nelson, H. D.; Hinterding, S. O. M.; Fainblat, R.; Creutz, S. E.; Li, X.; Gamelin, D. R. Mid-Gap States and Normal vs Inverted Bonding in Luminescent Cu+- and Ag+-Doped CdSe Nanocrystals. *J. Am. Chem. Soc.* **2017**, *139* (18), 6411–6421. https://doi.org/10.1021/jacs.7b01924.

(19) Nelson, H. D.; Li, X.; Gamelin, D. R. Computational Studies of the Electronic Structures of Copper-Doped CdSe Nanocrystals: Oxidation States, Jahn–Teller Distortions, Vibronic Bandshapes, and Singlet–Triplet Splittings. *J. Phys. Chem. C* **2016**, *120* (10), 5714–5723. https://doi.org/10.1021/acs.jpcc.5b11319.

(20) Whitham, P. J.; Knowles, K. E.; Reid, P. J.; Gamelin, D. R. Photoluminescence Blinking and Reversible Electron Trapping in Copper-Doped CdSe Nanocrystals. *Nano Lett.* **2015**, *15* (6), 4045–4051. https://doi.org/10.1021/acs.nanolett.5b01046.

(21) Knowles, K. E.; Hartstein, K. H.; Kilburn, T. B.; Marchioro, A.; Nelson, H. D.; Whitham, P. J.; Gamelin, D. R. Luminescent Colloidal Semiconductor Nanocrystals Containing Copper: Synthesis, Photophysics, and Applications. *Chem. Rev.* **2016**, *116* (18), 10820–10851. https://doi.org/10.1021/acs.chemrev.6b00048.

(22) Grandhi, G. K.; Tomar, R.; Viswanatha, R. Study of Surface and Bulk Electronic Structure of II–VI Semiconductor Nanocrystals Using Cu as a Nanosensor. *ACS Nano* **2012**, *6* (11), 9751–9763. https://doi.org/10.1021/nn304149s.

(23) Mundy, M. E.; Eagle, F. W.; Hughes, K. E.; Gamelin, D. R.; Cossairt, B. M. Synthesis and Spectroscopy of Emissive, Surface-Modified, Copper-Doped Indium Phosphide Nanocrystals. *ACS Materials Lett.* **2020**, *2* (6), 576–581. https://doi.org/10.1021/acsmaterialslett.0c00112.

(24) Hughes, K. E.; Hartstein, K. H.; Gamelin, D. R. Photodoping and Transient Spectroscopies of Copper-Doped CdSe/CdS Nanocrystals. *ACS Nano* **2018**, *12* (1), 718–728. https://doi.org/10.1021/acsnano.7b07879.

(25) Hassan, A.; Zhang, X.; Liu, C.; Snee, P. T. Electronic Structure and Dynamics of Copper-Doped Indium Phosphide Nanocrystals Studied with Time-Resolved X-Ray Absorption and Large-Scale DFT Calculations. *J. Phys. Chem. C* **2018**, *122* (20), 11145–11151. https://doi.org/10.1021/acs.jpcc.8b02124.

(26) Prins, P. T.; Spruijt, D. A. W.; Mangnus, M. J. J.; Rabouw, F. T.; Vanmaekelbergh, D.; de Mello Donega, C.; Geiregat, P. Slow Hole Localization and Fast Electron Cooling in Cu-Doped InP/ZnSe Quantum Dots. *J. Phys. Chem. Lett.* **2022**, *13* (42), 9950–9956. https://doi.org/10.1021/acs.jpclett.2c02764.

(27) Lu, T.; Chen, F. Multiwfn: A Multifunctional Wavefunction Analyzer. *Journal of Computational Chemistry* **2012**, *33* (5), 580–592. https://doi.org/10.1002/jcc.22885.

(28) Liu, Z.; Lu, T.; Chen, Q. An Sp-Hybridized All-Carboatomic Ring, Cyclo[18]Carbon: Electronic Structure, Electronic Spectrum, and Optical Nonlinearity. *Carbon* **2020**, *165*, 461–467. https://doi.org/10.1016/j.carbon.2020.05.023.

(29) Aruda, K. O.; Bohlmann Kunz, M.; Tagliazucchi, M.; Weiss, E. A. Temperature-Dependent Permeability of the Ligand Shell of PbS Quantum Dots Probed by Electron Transfer to Benzoquinone. *J. Phys. Chem. Lett.* **2015**, *6* (14), 2841–2846. https://doi.org/10.1021/acs.jpclett.5b01256.

(30) Long, D.; Wu, G.; Wang, W.; Yao, S. Photo-Induced Interfacial Electron Transfer from CdSe Quantum Dots to Surface-Bound p-Benzoquinone and Anthraquinone. *Res Chem Intermed* **2007**, *33* (7), 655–661. https://doi.org/10.1163/156856707781749937.

(31) Knowles, K. E.; Malicki, M.; Weiss, E. A. Dual-Time Scale Photoinduced Electron Transfer from PbS Quantum Dots to a Molecular Acceptor. *J. Am. Chem. Soc.* **2012**, *134* (30), 12470–12473. https://doi.org/10.1021/ja3060222.

(32) Lou, Y.; Chen, X.; Samia, A. C.; Burda, C. Femtosecond Spectroscopic Investigation of the Carrier Lifetimes in Digenite Quantum Dots and Discrimination of the Electron and Hole Dynamics via Ultrafast Interfacial Electron Transfer. *J. Phys. Chem. B* **2003**, *107* (45), 12431–12437. https://doi.org/10.1021/jp035618k.

(33) Htun, T. A Negative Deviation from Stern–Volmer Equation in Fluorescence Quenching. *Journal of Fluorescence* **2004**, *14* (2), 217–222. https://doi.org/10.1023/B:JOFL.0000016294.96775.fd.

(34) Boaz, H.; Rollefson, G. K. The Quenching of Fluorescence. Deviations from the Stern-Volmer Law. *J. Am. Chem. Soc.* **1950**, *72* (8), 3435–3443. https://doi.org/10.1021/ja01164a032.

(35) Peterson, M. D.; Jensen, S. C.; Weinberg, D. J.; Weiss, E. A. Mechanisms for Adsorption of Methyl Viologen on CdS Quantum Dots. *ACS Nano* **2014**, *8* (3), 2826–2837. https://doi.org/10.1021/nn406651a.

(36) Calvin, J. J.; Swabeck, J. K.; Sedlak, A. B.; Kim, Y.; Jang, E.; Alivisatos, A. P. Thermodynamic Investigation of Increased Luminescence in Indium Phosphide Quantum Dots by Treatment with Metal Halide Salts. *J. Am. Chem. Soc.* **2020**, *142* (44), 18897–18906. https://doi.org/10.1021/jacs.0c08954.

(37) Klimov, V. I. Optical Nonlinearities and Ultrafast Carrier Dynamics in Semiconductor Nanocrystals. *J. Phys. Chem. B* **2000**, *104* (26), 6112–6123. https://doi.org/10.1021/jp9944132.

(38) Zhu, H.; Song, N.; Lian, T. Controlling Charge Separation and Recombination Rates in CdSe/ZnS Type I Core−Shell Quantum Dots by Shell Thicknesses. *J. Am. Chem. Soc.* **2010**, *132* (42), 15038–15045. https://doi.org/10.1021/ja106710m.

(39) Morris-Cohen, A. J.; Peterson, M. D.; Frederick, M. T.; Kamm, J. M.; Weiss, E. A. Evidence for a Through-Space Pathway for Electron Transfer from Quantum Dots to Carboxylate-Functionalized Viologens. *J. Phys. Chem. Lett.* **2012**, *3* (19), 2840–2844. https://doi.org/10.1021/jz301318m.

(40) Wang, Y.-F.; Wang, H.-Y.; Li, Z.-S.; Zhao, J.; Wang, L.; Chen, Q.-D.; Wang, W.-Q.; Sun, H.-B. Electron Extraction Dynamics in CdSe and CdSe/CdS/ZnS Quantum Dots Adsorbed with Methyl Viologen. *J. Phys. Chem. C* **2014**, *118* (31), 17240–17246. https://doi.org/10.1021/jp5024789.

(41) Zhao, F.; Li, Q.; Han, K.; Lian, T. Mechanism of Efficient Viologen Radical Generation by Ultrafast Electron Transfer from CdS Quantum Dots. *J. Phys. Chem. C* **2018**, *122* (30), 17136–17142. https://doi.org/10.1021/acs.jpcc.8b06551.

(42) Wu, K.; Song, N.; Liu, Z.; Zhu, H.; Rodríguez-Córdoba, W.; Lian, T. Interfacial Charge Separation and Recombination in InP and Quasi-Type II InP/CdS Core/Shell Quantum Dot-Molecular Acceptor Complexes. *J. Phys. Chem. A* **2013**, *117* (32), 7561–7570. https://doi.org/10.1021/jp402425w.

(43) Macfarlane, A. J.; Williams, R. J. P. Charge-Transfer Properties of Some Paraquat Salts. *J. Chem. Soc., A* **1969**, 1517. https://doi.org/10.1039/j19690001517.

(44) Matylitsky, V. V.; Dworak, L.; Breus, V. V.; Basché, T.; Wachtveitl, J. Ultrafast Charge Separation in Multiexcited CdSe Quantum Dots Mediated by Adsorbed Electron Acceptors. *J. Am. Chem. Soc.* **2009**, *131* (7), 2424–2425. https://doi.org/10.1021/ja808084y.

(45) Goings, J. J.; Schimpf, A. M.; May, J. W.; Johns, R. W.; Gamelin, D. R.; Li, X. Theoretical Characterization of Conduction-Band Electrons in Photodoped and Aluminum-Doped Zinc Oxide (AZO) Quantum Dots. *J. Phys. Chem. C* **2014**, *118* (46), 26584–26590. https://doi.org/10.1021/jp5090229.

(46) Petrone, A.; Beck, R. A.; Kasper, J. M.; Li, X.; Huang, Y.; Crane, M.; Pauzauskie, P. Electronic Structures and Spectroscopic Signatures of Silicon-Vacancy Containing Nanodiamonds. *Phys. Rev. B* **2018**, *98* (20), 205405. https://doi.org/10.1103/PhysRevB.98.205405.

(47) Park, N.; Eagle, F. W.; DeLarme, A. J.; Monahan, M.; LoCurto, T.; Beck, R.; Li, X.; Cossairt, B. M. Tuning the Interfacial Stoichiometry of InP Core and InP/ZnSe Core/Shell Quantum Dots. *J. Chem. Phys.* **2021**, *155* (8), 084701. https://doi.org/10.1063/5.0060462.

(48) Chen, B.; Li, D.; Wang, F. InP Quantum Dots: Synthesis and Lighting Applications. *Small* **2020**, *16* (32), 2002454. https://doi.org/10.1002/smll.202002454.

(49) Cho, E.; Kim, T.; Choi, S.; Jang, H.; Min, K.; Jang, E. Optical Characteristics of the Surface Defects in InP Colloidal Quantum Dots for Highly Efficient Light-Emitting Applications. *ACS Appl. Nano Mater.* **2018**, *1* (12), 7106–7114. https://doi.org/10.1021/acsanm.8b01947.

(50) *Citation | Gaussian.com*. https://gaussian.com/citation/ (accessed 2023-02-27).

(51) Ernzerhof, M.; Scuseria, G. E. Assessment of the Perdew–Burke–Ernzerhof Exchange-Correlation Functional. *J. Chem. Phys.* **1999**, *110* (11), 5029–5036. https://doi.org/10.1063/1.478401.

(52) Adamo, C.; Barone, V. Toward Reliable Density Functional Methods without Adjustable Parameters: The PBE0 Model. *J. Chem. Phys.* **1999**, *110* (13), 6158–6170. https://doi.org/10.1063/1.478522.

(53) Perdew, J. P.; Burke, K.; Ernzerhof, M. Generalized Gradient Approximation Made Simple [Phys. Rev. Lett. 77, 3865 (1996)]. *Phys. Rev. Lett.* **1997**, *78* (7), 1396–1396. https://doi.org/10.1103/PhysRevLett.78.1396.

(54) Dunning, T. H.; Hay, P. J. Modern Theoretical Chemistry; Plenum: New York, 1977; Vol. 3, pp 1–28.

(55) Hay, P. J.; Wadt, W. R. Ab Initio Effective Core Potentials for Molecular Calculations. Potentials for the Transition Metal Atoms Sc to Hg. *J. Chem. Phys.* **1985**, *82* (1), 270–283. https://doi.org/10.1063/1.448799.

(56) Wadt, W. R.; Hay, P. J. Ab Initio Effective Core Potentials for Molecular Calculations. Potentials for Main Group Elements Na to Bi. *J. Chem. Phys.* **1985**, *82* (1), 284–298. https://doi.org/10.1063/1.448800.

(57) Hay, P. J.; Wadt, W. R. Ab Initio Effective Core Potentials for Molecular Calculations. Potentials for K to Au Including the Outermost Core Orbitals. *J. Chem. Phys.* **1985**, *82* (1), 299–310. https://doi.org/10.1063/1.448975.

(58) Casida, M. E. *Recent Advances in Density Functional Methods: Part I*; World Scientific: Singapore, 1995; Vol. 1.

(59) Dreuw, A.; Head-Gordon, M. Single-Reference Ab Initio Methods for the Calculation of Excited States of Large Molecules. *Chem. Rev.* **2005**, *105* (11), 4009–4037. https://doi.org/10.1021/cr0505627.

(60) Stratmann, R. E.; Scuseria, G. E.; Frisch, M. J. An Efficient Implementation of Time-Dependent Density-Functional Theory for the Calculation of Excitation Energies of Large Molecules. *J. Chem. Phys.* **1998**, *109* (19), 8218–8224. https://doi.org/10.1063/1.477483.

4 LEVERAGING CATION EXCHANGE IN INP MAGIC SIZED CLUSTERS TO ACCESS COINAGE METAL PHOSPHIDE NANOCRYSTALS

Significant portions of this chapter have been published by Forrest W. Eagle, Samantha Harvey, Helen Larson, Autumn J. Abbott, Dylan Ladd, Kelsey Levine, Michael F. Toney, Daniel R. Gamelin, and Brandi M. Cossairt.
10.26434/chemrxiv-2023-khl9g, **2023**

4.1 NOTE FOR COLLABORATIVE WORK

Transient absorption spectroscopy data was collected by Dr. Samantha Harvey under the co-guidance of Professors Brandi Cossairt and Daniel Gamelin. PDF data was collected by Kelsey Levin and Dylan Ladd, working under the guidance of Professor Michael Toney at the University of Boulder, Colorado. PDF measurements were conducted at Brookhaven National Laboratory. TEM imaging was performed by Helen Larson.

4.2 INTRODUCTION

Magic sized clusters (MSCs) are atomically precise nanomaterials often found as metastable intermediates in the synthesis of nanocrystals.[1–3] Due to the atomically precise nature of these clusters, their physical, electronic, and reactivity properties can be studied without complications associated with ensemble heterogeneity. In particular, MSCs serve as a unique platform for the study of cation exchange. By understanding the mechanism and structural changes involved in cation exchange, synthetic chemists are able to rationally design new pathways to access colloidal nanomaterials that may be difficult or impossible to form by traditional bottom up nucleation and growth.[4–8] Additionally, although cation exchange in III-V nanocrystals often

requires high temperatures, cation exchange in magic sized clusters can often be performed at room temperature.[9–11] While cation exchange has been widely studied in Zn and Cd-chalcogenide MSCs,[11–17] few reports examine cation exchange in indium phosphide MSCs.[10,18] In this paper we demonstrate the cation exchange of InP magic sized clusters with coinage metals (Cu, Ag, and Au). Coinage metals are of particular interest due to the unique properties that characterize Group 11 binary compounds like phosphides and chalcogenides, including localized surface plasmon resonances (LSPRs) and enhanced catalytic activities. Given the ion mobility associated with copper ions in inorganic lattices,[19] the Cu-P products are also of interest for sequential cation exchange chemistries to access multinary and high entropy materials. Copper phosphide has been widely studied, with special interest in the NIR LSPR generated in defective $Cu_{3-x}P$ lattices.[7,20–22] Additionally, Cu_3P is notable for its efficient electrocatalysis of both the hydrogen and oxygen evolution reactions, showing near unity Faradaic efficiency during hydrogen evolution and only minor degradation after extended use.[23–26] The other coinage metal phosphides, Ag-P and Au-P, have traditionally been difficult to synthesize due to their metastability.[27,28] Although Ag-P compounds have been predicted to serve as excellent catalysts for CO_2 reduction, accessing these materials has been synthetically challenging.[29,30] Homologous Ag-As and Ag-Sb systems have been found in nature, suggesting formation of Ag-pnictogen species is possible, however.[31–33] Au_2P_3 nanostructures have been synthesized;[27,34] however, these syntheses require phosphorization of Au nanocrystals and often lead to large domains of unreacted Au. Additionally, although AuP has been predicted,[28] there has been no synthesis of this material at the nanoscale nor the bulk. A more complete understanding of the electronic and catalytic properties of Au-P compounds will require the synthesis of crystalline, single domain nanocrystals across the range of possible stoichiometries.

In this work we demonstrate room temperature cation exchange in InP magic sized clusters, leading to the formation of doped InP clusters or small nanocrystals of $Cu_{3-x}P$, $Ag_{3-x}P$, and $Au_{3-x}P$. We further show that these small nanocrystals can then grow upon heating, leading to larger nanocrystals across the coinage metal phosphide family (**Figure 4.1**). This MSC chemistry thus provides a versatile approach to the preparation, isolation, and study of coinage metal phosphide nanostructures.

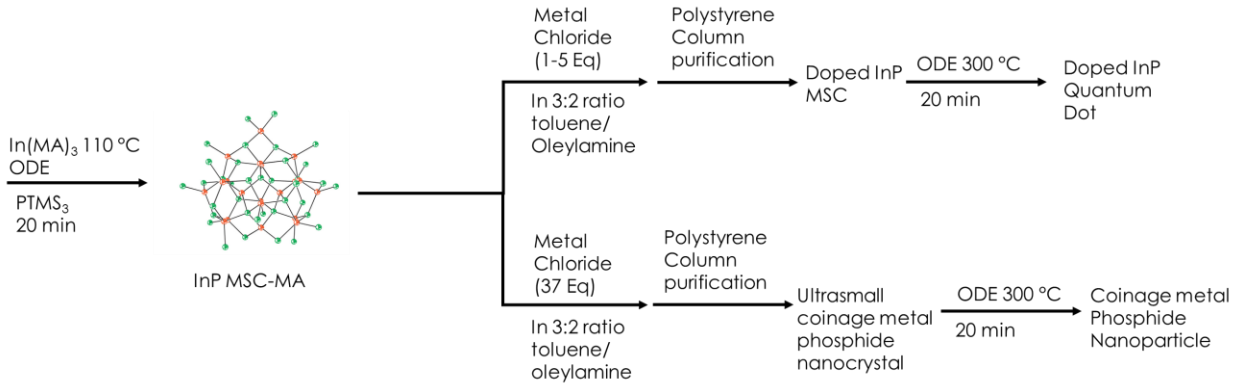

Figure 4.1. Summary of cation exchange reactions of InP MSCs with coinage metals forming either doped InP MSCs or ultrasmall coinage metal phosphide nanocrystals. After isolation, these products can be heated to form doped InP or coinage metal phosphide nanoparticles.

4.3 Results and Discussion

4.3.1 Synthesis and optical properties of doped clusters

Given the ultra-small size of MSCs, their optical properties are highly sensitive to changes in lattice structure because even small perturbations can greatly impact their electronic structure. As such, UV-Vis absorption spectroscopy can be used as a sensitive diagnostic tool to monitor changes in the cluster core. Upon adding low molar equivalents (1, 5 eq) of $CuCl_2$ solubilized in a 6:4 mixture of toluene and oleylamine to the starting $In_{37}P_{20}(O_2CC_{13}H_{27})_{51}$ cluster, we see the

growth of a low-energy tail extending into the sub-bandgap region, followed by a broadening of the InP absorption band (**Figure 4.2A**). This broadening is consistent with the absorption of other Cu-doped and Cu-based nanocrystals, including Cu-CdSe and $CuInS_2$, and is not attributed to size inhomogeneity but rather a metal to ligand (conduction band) charge transfer type transition involving copper-localized holes.[35–37] As such, we attribute this continuous broadening of the absorption spectrum to the introduction of copper into the core of the MSC as opposed to exchange with the excess surface indium carboxylate Z-type ligands.[38] Upon addition of 37 equivalents of Cu (equal to the number of indium ions of the original MSC), we see complete loss of the original absorption peak, with conversion to a broad, featureless absorption spectrum spanning the visible region. This spectrum mirrors the UV-Vis absorption of previously characterized $Cu_{3-x}P$ nanocrystals, as well as Cu_2S and Cu_2Se nanocrystals.[20,21,39,40] Furthermore, the 37Cu-MSC exhibits the growth of a new feature in the near-infrared region of its absorption spectrum upon oxidation, as seen in the inset of **Figure 4.2A**. Previous reports of Cu_2Se nanoclusters have also detailed the growth of a similar feature upon oxidation, attributed to a new plasmon resonance.[41] This new feature is centered at ~800 nm, which is higher energy than the LSPRs of $Cu_{3-x}P$ nanocrystals, and this energy could reflect a blueshift due to quantum confinement.[21,41–43]

Addition of AgCl and AuCl to the $In_{37}P_{20}$ MSCs gives similar results - low equivalents of Ag and Au lead to the same spectral broadening, followed by conversion to a broad featureless absorption spectrum upon the addition of 37 equivalents (**Figure 4.2B, C**). While no reports of nanoparticle Ag-P complexes exist, this broad absorption is similar to that found in Ag_2Se and Ag_2S nanocrystals.[44–47]

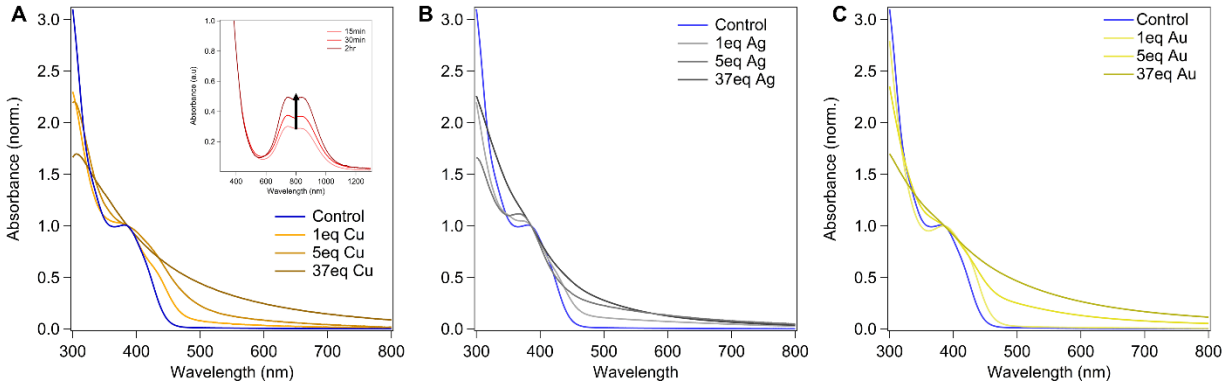

Figure 4.2. Absorption spectra of coinage metal treated $In_{37}P_{20}$ MSCs. A) Addition of 1, 5, and 37 equivalents of $CuCl_2$. Inset: absorbance spectra of clusters treated with 37 equivalents of Cu followed by exposure to oxygen for the times indicated. Note that the dip at the absorption maximum is and instrumental artifact. B) Addition of 1, 5, and 37 equivalents of AgCl. C) Addition of 1, 5, and 37 equivalents of $AuCl_3$.

We also observed similar results for $In_{37}P_{20}$ MSCs treated with CuCl and $AuCl_3$ solubilized in toluene/oleylamine mixtures, as shown in **Figure 4.3A-B**, indicating that the starting metal halide solution is likely reduced in situ by the oleylamine and that all products contain coinage metals in the +1 oxidation state. This conclusion is confirmed by comparative XPS analysis (**Figure 4.3C-D**).[48]

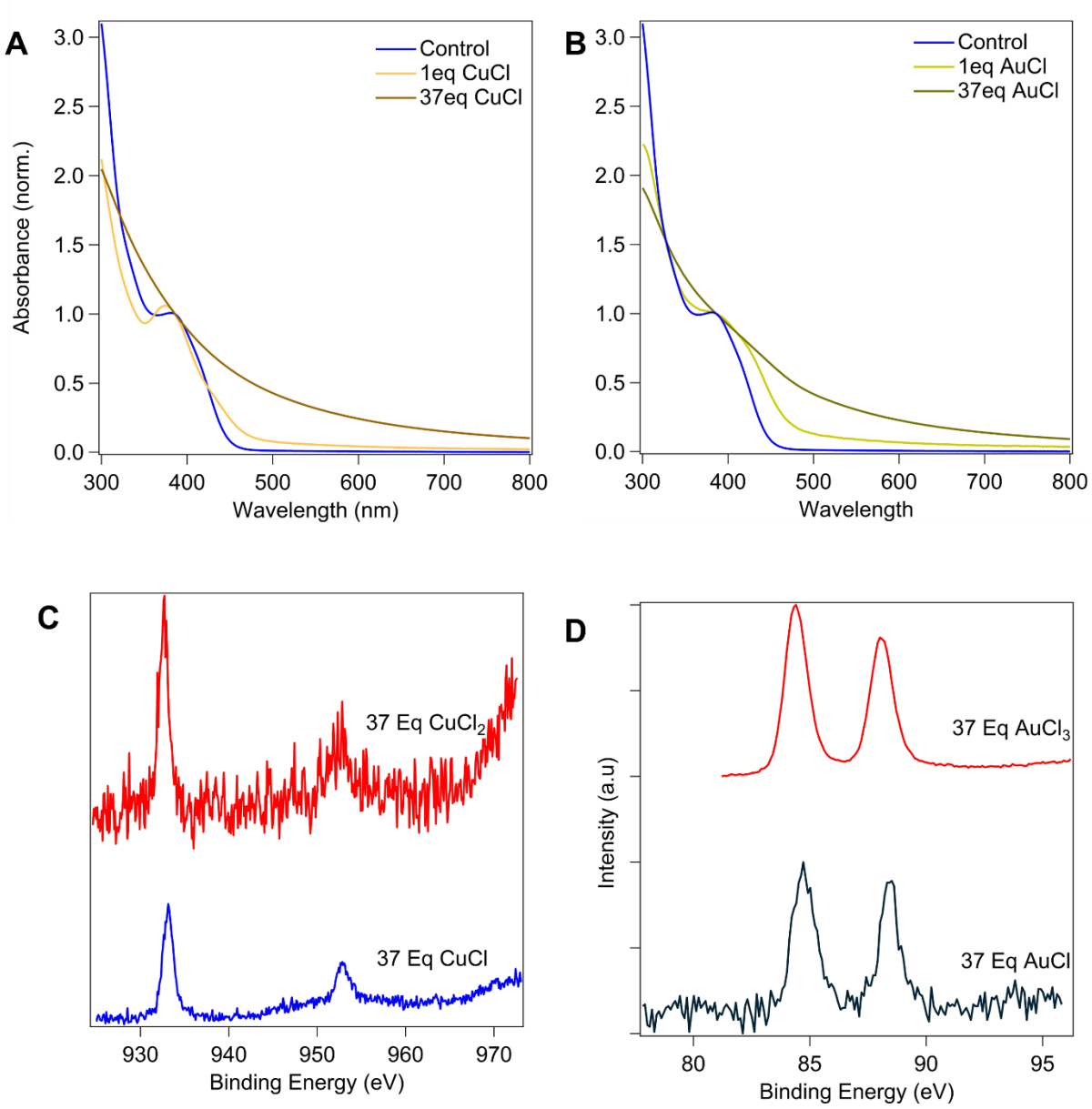

Figure 4.3. Absorption spectra of InP MSCs treated with A) CuCl and B) AuCl solutions. C) XPS of CuCl treated clusters compared to $CuCl_2$ treated clusters. D) XPS of AuCl treated clusters compared to $AuCl_3$ treated clusters.

Interestingly, upon attempting full cation exchange with coinage metal halides solubilized by tributyl phosphine, only minimal broadening in the absorbance profile is observed, suggesting

hindered cation exchange when high equivalents of coinage metal are added under these conditions (**Figure 4.4**).

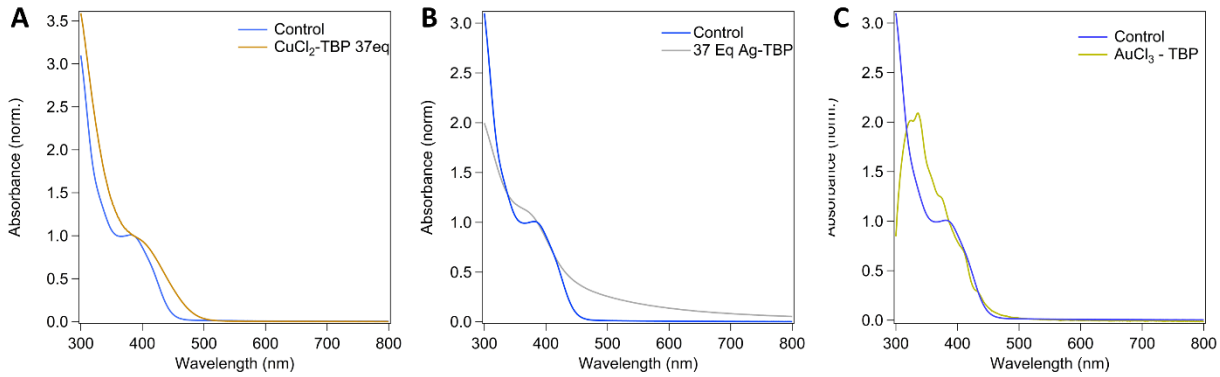

Figure 4.4. Absorption spectra of InP MSCs with addition of metal-TBP solutions. A) $CuCl_2$-TBP B) AgCl-TBP C) $AuCl_3$-TBP. Notably, the addition of Au-TBP seems to nucleate gold clusters instead of interacting with the InP MSCs with the absorbance spectrum mirroring previous reports of Au clusters.

This result suggests that the precursor identity is important, and that amines help to drive the cation exchange. Further investigation on the impact of precursor identity on the cation exchange was performed by examining the effect that the anion ligand has upon cation exchange. Upon running the same exchange reactions with CuBr and CuI we observed that the cation exchange was hindered in the case of CuBr (and CuI to a lesser extent) (**Figure 4.5**). These results indicate that the anion identity can be utilized to further tune the reactivity of these exchange reactions. Previous work has shown that the addition of metal carboxylates to InP magic sized clusters can induce cation exchange, but requires much more added cation.[10]

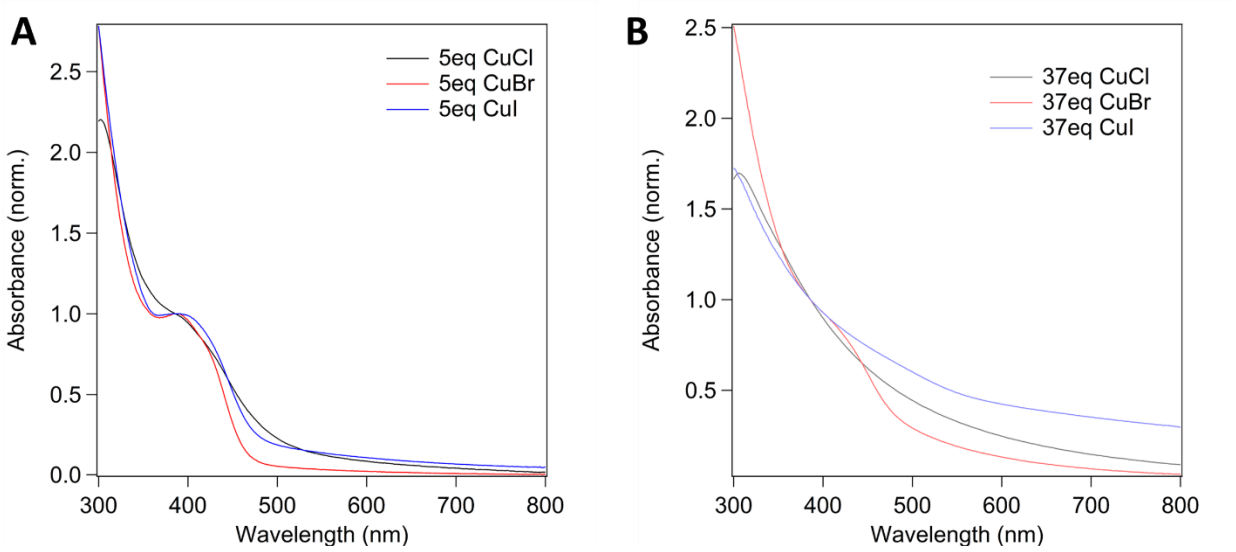

Figure 4.5. Absorption spectra of InP MSCs with addition of A) 5 eqivalents of CuX (X=Cl, Br, I), and 37 equivalents of CuX (X = Cl, Br, I).

4.3.2 Structural Characterization of doped MSCs

The initial pXRD pattern of $In_{37}P_{20}$ MSCs does not correspond to the zincblende phase of bulk InP. Instead the cluster has a strained core that can be described as having quasi-wurtzite character.[38] Upon the addition of 1 and 5 equivalents of $CuCl_2$ to the MSC, we see shifting and broadening of the diffraction peaks, indicating the original lattice becomes more disordered as more Cu ions are introduced into the core (Table S1). Upon addition of 37 equivalents, the original diffraction peaks are no longer visible and instead are replaced by two main peaks at 2Θ = 40° and 47° as seen in **Figure 4.6A**. These peaks are consistent with ultrasmall hexagonal Cu_3P nanocrystals.[61] With the addition of 1 and 5 equivalents of AgCl, we once again see the shifting and broadening of the original $In_{37}P_{20}$ MSC peaks that is characteristic of the formation of a defective lattice. Upon the addition of 37 equivalents of AgCl we see more drastic changes in the diffraction pattern, as shown in **Figure 4.6B**. While Cu-P compounds have routinely been synthesized and characterized, Ag-P compounds have not been successfully realized on the

nanoscale despite much synthetic effort, leading to little to no literature from which to draw comparisons.[29,30] Examination of the Au doped species (**Figure 4.6**C) shows much less broadening at 5 equivalents when compared to the Ag and Cu doped species – instead the growth of a new peak centered around 40° is observed – this peak corresponds with the major diffraction peak in hexagonal Au_3P.[62]

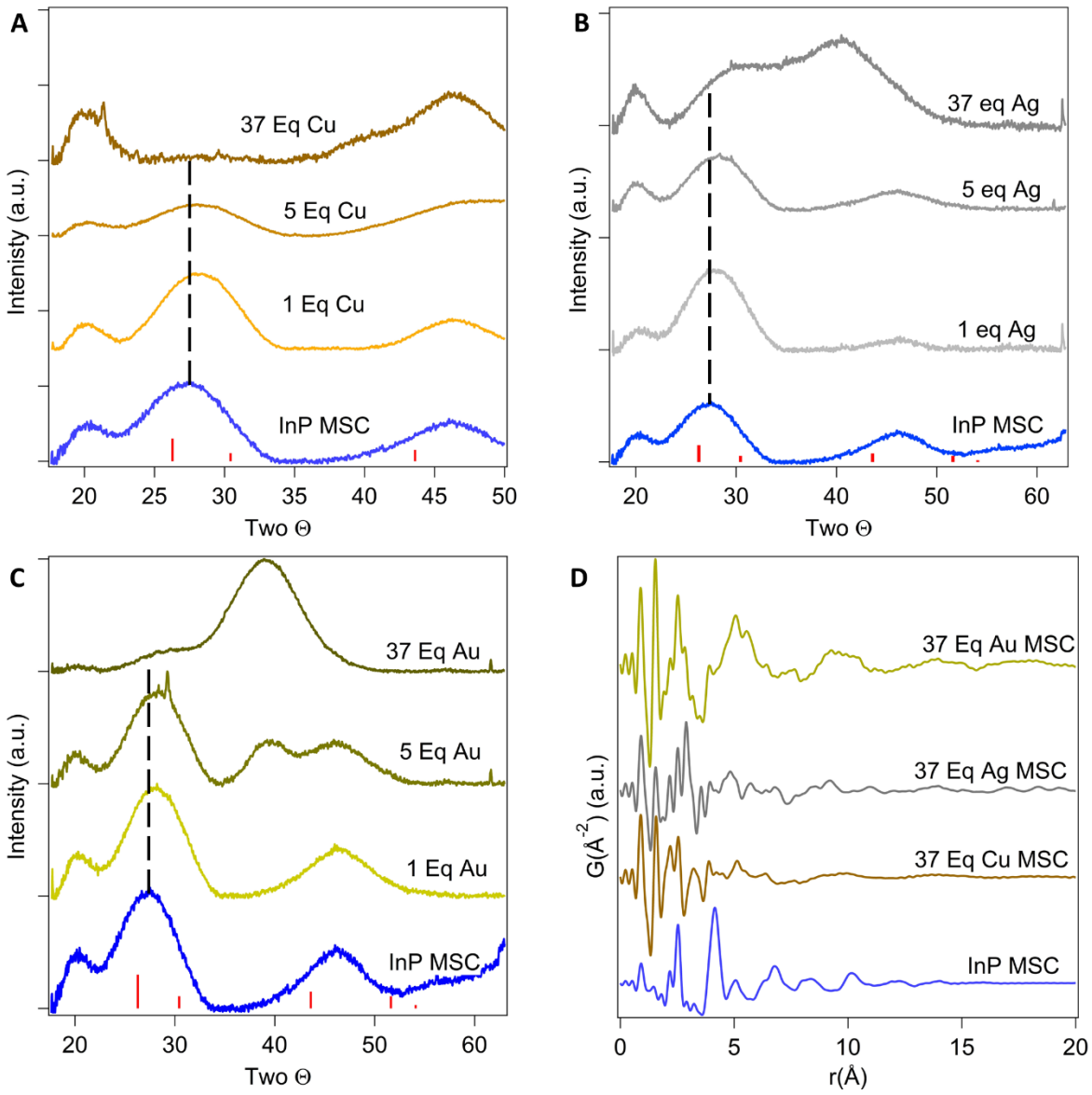

Figure 4.6. A) pXRD pattern upon addition of $CuCl_2$ to $In_{37}P_{20}$. Zinc blende InP is shown in red. B) pXRD pattern upon addition of AgCl to $In_{37}P_{20}$. Zinc blende InP is shown in red. C) pXRD

pattern upon addition of $AuCl_3$ to $In_{37}P_{20}$. Zinc blende InP is shown in red. D) PDF analysis of InP MSCs and clusters treated with 37 equivalents of coinage metal.

As higher equivalents of Au are added, this new peak becomes better defined, while the peaks attributed to InP are lost. This may suggest a highly cooperative cation exchange pathway for Au – as soon as doping reaches a critical concentration, full cation exchange is pushed to completion similar to Cu exchange in CdSe and Ag exchange in CdS.[63,64] This mirrors previous experiment showing that Ag leads to cooperative cation exchange avalanche at lower concentrations than Cu.[64] . As the size of the Au ion is larger, the InP lattice cannot as easily rearrange around the dopant, leading to structural transformation at earlier dopant concentrations. This would further agree with theoretical predictions that show the InP MSC lattice cannot rearrange favorably around larger dopants.[56,64] These broad peaks are consistent with ultrasmall nanocrystals, which was further corroborated by TEM analysis, showing that the average size of the fully cation exchanged clusters is 3 nm for the Cu_3P and 2nm for the Ag_3P and Au_3P **(Figure 4.7)**.

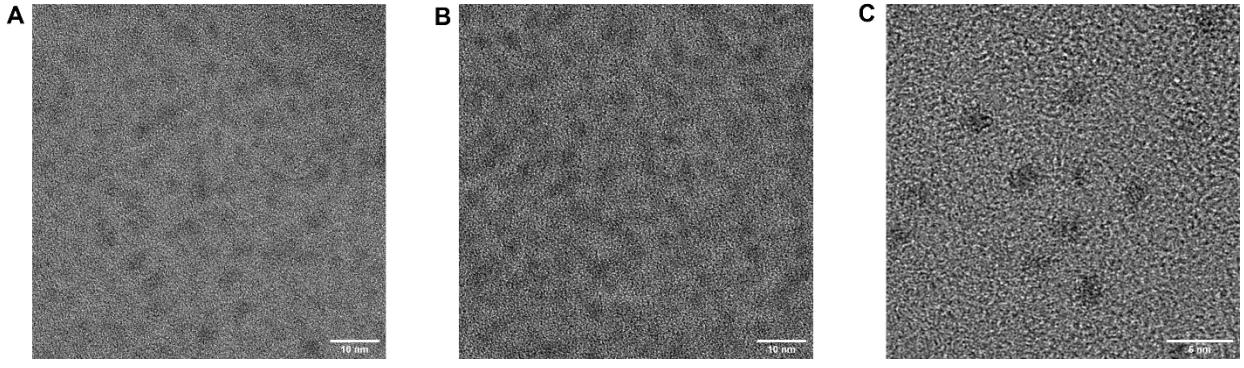

Figure 4.7. TEM analysis of InP clusters after full exchange with Cu (A), Ag (B) and Au (C).

These structural changes are further corroborated by PDF analysis of the 37 equivalent treated samples (**Figure 4.6**D). Previous work in our group has shown the sensitivity of PDF to changes to the internal lattice of InP MSCs.[2,10] Most noticeably we see the loss of the prominent peak around 4.1 Å, representative of the In-In network in the original InP lattice. While previous PDF analysis does not exist for Ag-P or Au-P complexes, we see that the internal lattice of the Cu-P cluster is similar to that of Cu_3P nanocrystals with major reflections at 2.25 and 2.61 Å corresponding to Cu-P and Cu-Cu bonds respectively.[65] Although previous PDF analysis does not exist for Ag-P or Au-P complexes, the Ag-P and Au-P clusters show new peaks around 2.9-3 Å in the Ag-P and Au-P clusters (**Figure 4.8**). We note that all three clusters also show peaks at 2.2 and 2.6 Å, and it is difficult to determine if these peaks correspond to the In-O and In-P bonds of surface bound In-carboxylate moieties or if they reflect distorted metal-metal and metal-phosphorus distances similar to those found in Cu-P. Overall, the combination of XRD, PDF, and TEM data point to the formation of unique Cu-P, Ag-P, and Au-P clusters through these cation exchange reactions.

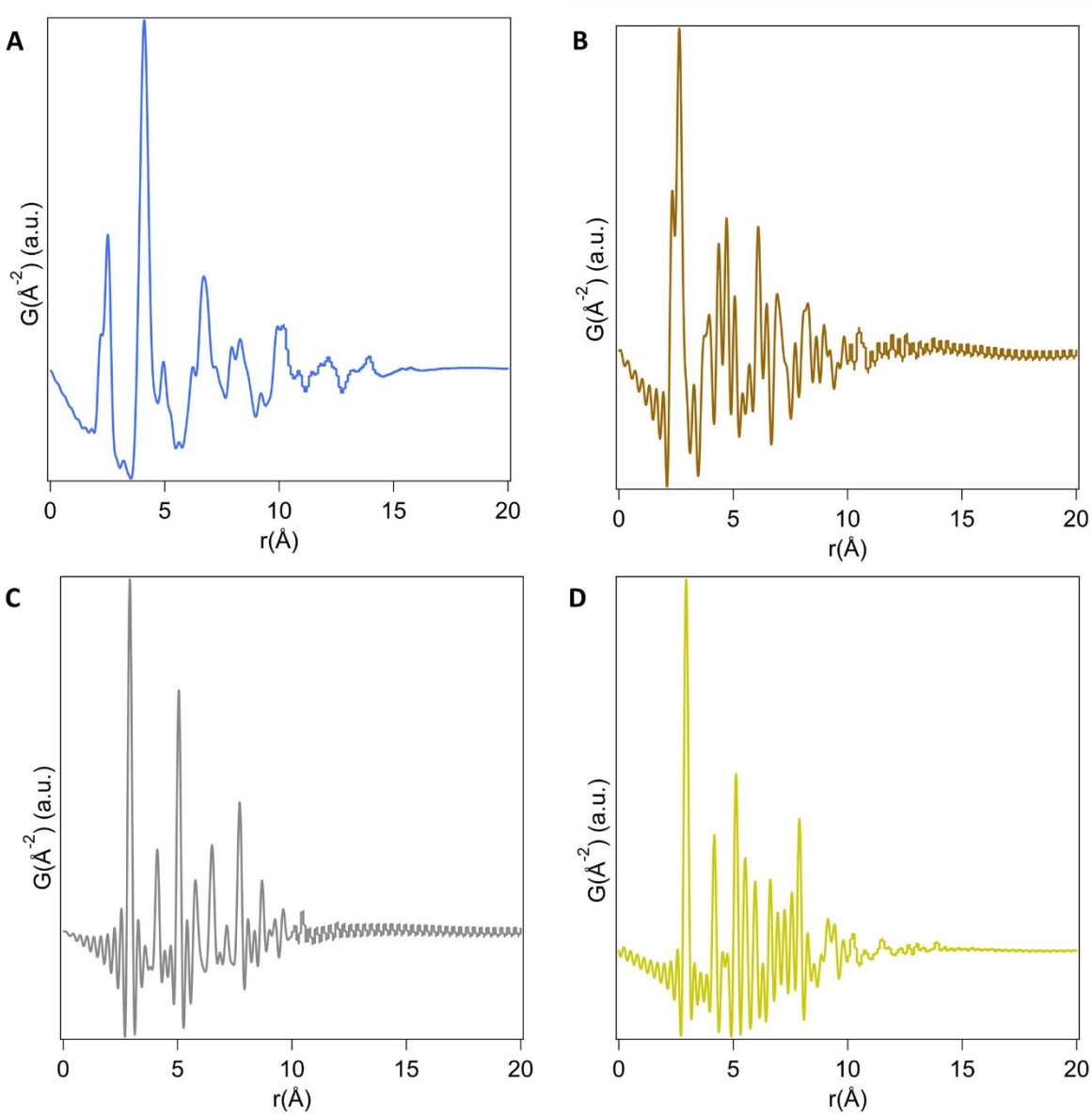

Figure 4.8. Simulated PDF of A) InP. B) Cu_3P C) Ag_3P, and D) Au_3P

To further resolve the composition and coordination environments of the coinage metal treated clusters, XPS data were collected. After addition of $CuCl_2$ to the $In_{37}P_{20}$ MSCs, we see the growth of the expected copper 2p peaks with further increased resolution upon additional equivalents as seen in **Figure 4.9A**. With increasing equivalents of added Cu, we also see a shift to lower binding energies by over 1 eV, with the $2p_{3/2}$ peak reaching 932.6 eV for the 37-equivalent sample. This value is consistent with that measured for Cu_3P.[19] The addition of AgCl

to $In_{37}P_{20}$ MSCs leads to the growth of the Ag 3d peaks as seen in **Figure 4.9B**. As Ag-P has not been successfully synthesized previously, there is no comparative XPS to examine. However, we do see the growth of silver 3d peaks as more silver is added, indicating increasing incorporation of silver into the material. Furthermore, these peaks closely correspond to the binding energy found for Ag_2S.[66] Addition of $AuCl_3$ to the $In_{37}P_{20}$ MSC once again shows an increasing Au signal with more equivalents added, as shown in **Figure 4.9C**. In the Au sample (**Figure 4.9C**), the initial binding energy of the $4f_{7/2}$ peak is 84.2 eV, which is reminiscent of Au-amine complexes.[67] As more equivalents are added, the binding energy shifts to 84.5 eV which corresponds to Au in InP,[68] before shifting to higher binding energies, suggesting greater electronic interaction between the Au and P atoms in the lattice. For reference, XPS of as-synthesized $In_{37}P_{20}$ MSCs shows In peaks characteristic of InP, centered at 444.7 eV, as shown in **Figure 4.9D**.[69]

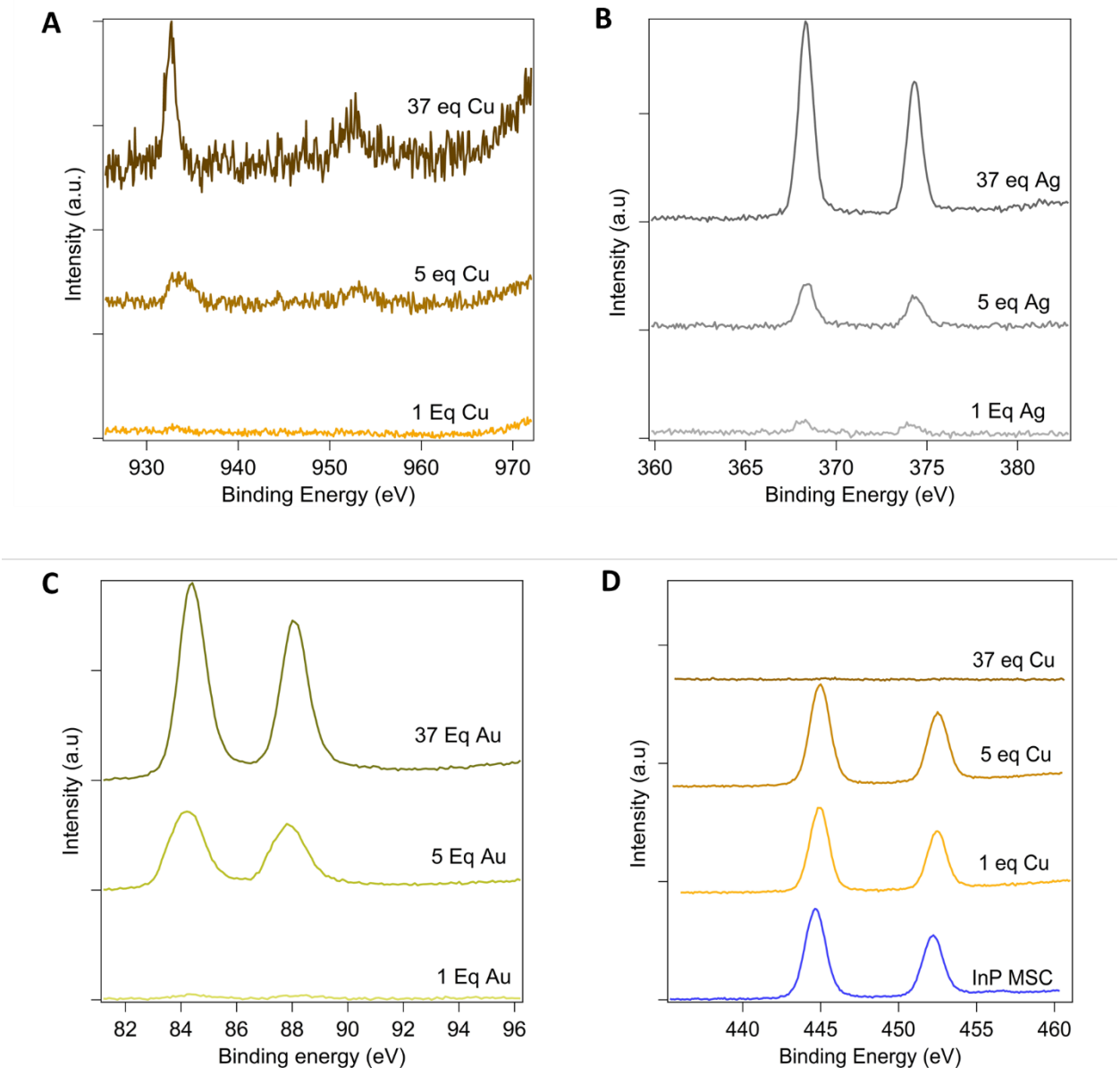

Figure 4.9. A) XPS spectra of Cu 2p peaks with addition of $CuCl_2$ to $In_{37}P_{20}$ MSCs. B) Ag 3d peaks upon addition of AgCl to $In_{37}P_{20}$ MSCs. C) Au 4f peaks with addition of $AuCl_3$ to $In_{37}P_{20}$ MSCs. D) XPS spectra of In 3d peaks upon addition of $CuCl_2$ to $In_{37}P_{20}$ MSCs.

After the introduction of dopants, the peaks begin to shift to higher binding energy, with shifts of over 1 eV, to 445.9 eV, highly reminiscent of $InCl_3$ or $In(O_2CR)_3$.[10,70] As such, we posit that the many of the In ions in these samples have been exchanged out of the cluster core and

remain instead as loosely associated molecular or surface bound species. Upon adding 37 equivalents of Au, we see complete loss of the In signal, suggesting complete cation exchange. These data correspond well with other forms of atomic elemental analysis, with ICP data showing small to no evidence of indium left in the core of the fully exchanged nanocrystals **(Table 4.1**).

Table 4.1. ICP-OES analysis of doped and undoped samples.

Sample	**In**	**P**	**Cu**	**Ag**	**Au**
InP MSC	1.9	1	-	-	-
1 Eq Cu	2	1	0.15	-	-
1 Eq Ag	1.9	1	-	0.12	-
1 Eq Au	2	1	-	-	0.16
5 Eq Cu	1.8	1	0.26	-	-
5 Eq Ag	1.6	1	-	0.3	-
5 Eq Au	1.5	1	-	-	0.6
37 Eq Cu	0.1	1	3.2	-	-
37 Eq Ag	0.3	1	-	3.1	-
37 Eq Au	0.5	1	-	-	5
37 Eq Cu Conversion	0.1	1	3.3	-	-
37 Eq Ag Conversion	0.15	1	-	2.9	-
37 Eq Au Conversion	0.1	1	-	-	4
TBP-AuCl3 (37 Eq)	1.6	1			0.2
TBP – CuCl2 (37 Eq)	1.6	1	0.3		
TBP – AgCl (37 Eq)	1.5	1		0.28	
Amine Treated Cluster	1.7	1			

4.3.3 Transient optical properties of doped and fully exchanged clusters

As previous reports have shown that the introduction of coinage metals to InP quantum dots drastically effects their charge carrier lifetimes,[36,60,61] we turned to transient absorption spectroscopy to examine if a similar phenomenon would occur with these even smaller materials. The transient absorption spectra of cation exchanged MSCs were strongly affected by increasing

molar equivalents of coinage metal cations. In lightly doped samples, a broadening that matches the change in the absorption profile is observed (**Figure 4.10**).

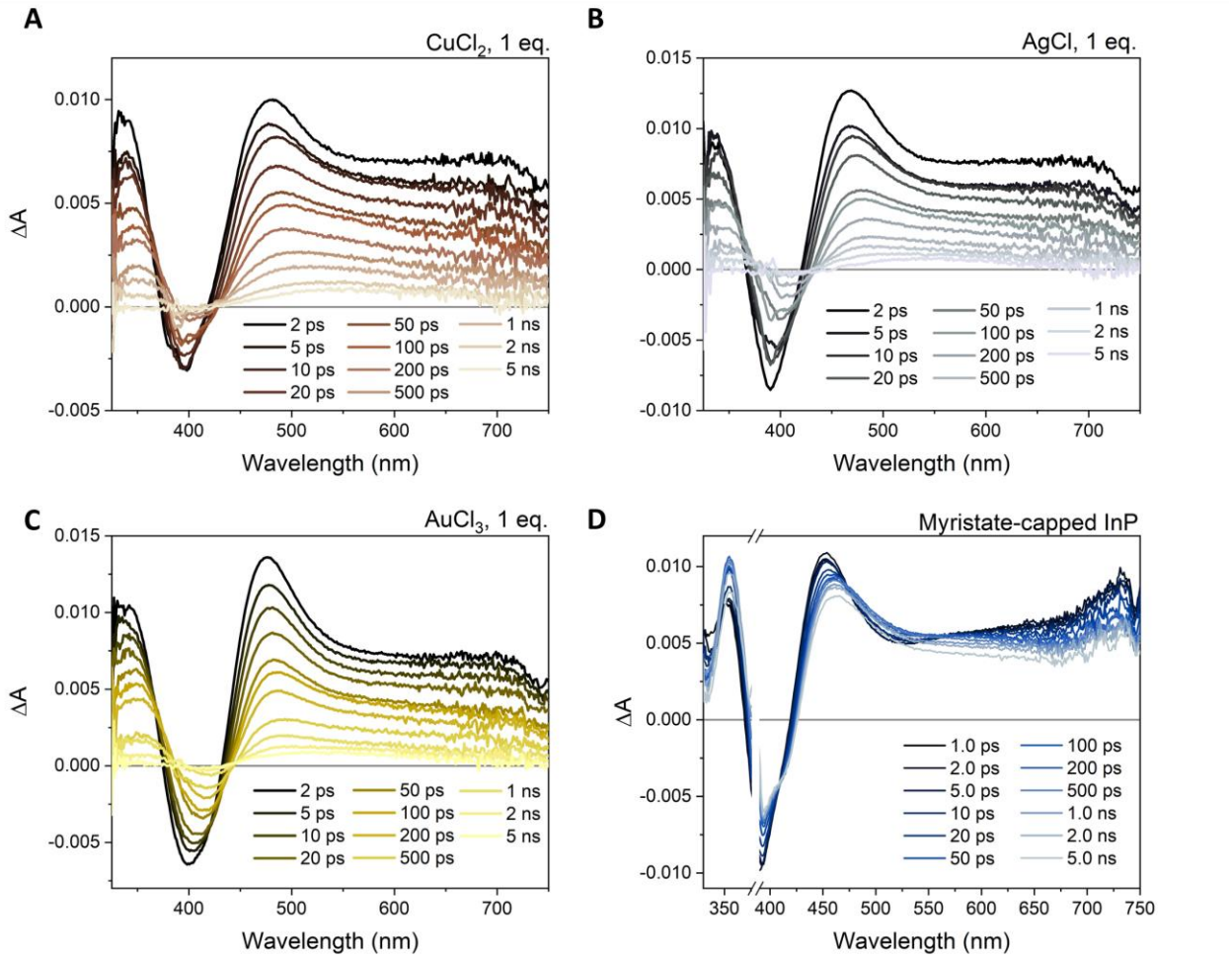

Figure 4.10. Transient absorption spectra of InP MSCs following addition of 1 equivalent of $CuCl_2$ (A), AgCl (B), and $AuCl_3$ (C). D) Transient absorption spectra of myristate capped $In_{37}P_{20}$ MSCs.

Clusters doped with a single equivalent of coinage metal show a drastic reduction in both the bleach and photoinduced absorption lifetimes, as shown in **Figure 4.11A-C,** with lifetimes for Cu, Ag, and Au doped clusters as 210, 150, and 120 ps, respectively. In contrast, the undoped clusters have lifetimes of 1550 ps, as seen in **Figure 4.11D**. This relatively long lifetime is

attributable to localization of the charge carriers in the highly strained excited state of the InP MSC, analogous to molecular species.[62,63] The drastic differences in excited state lifetimes could conceivably be attributed to the evolution of MSCs from a molecular like species with highly localized frontier orbitals to one with a much more delocalized electronic structure as structural rearrangement occurs near the surface to alleviate strain.[62] Additional transient absorption studies show that the lifetime of the same cluster treated with amine is reduced, but longer than the doped species, as shown in the kinetic data of **Figure 4.11D**.

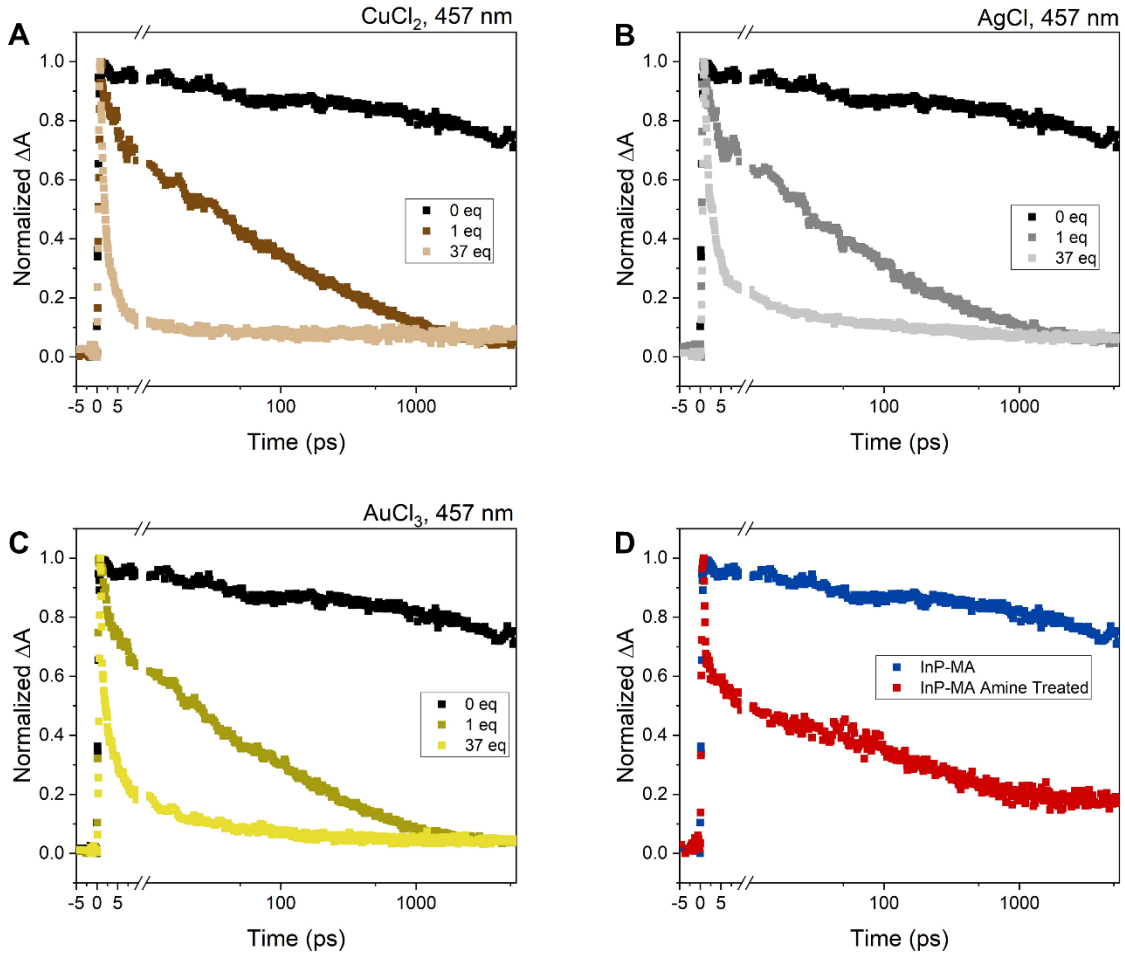

Figure 4.11. Transient absorption decay dynamics of InP MSCs following addition of 1 and 37 equivalents of $CuCl_2$ (A), AgCl (B), and $AuCl_3$ (C). D) Transient absorption kinetics of myristate capped $In_{37}P_{20}$ and amine treated cluster.

The large number of new mid-gap states introduced upon doping, evident from the broadened absorption spectra of **Figure 4.2**, are expected to facilitate rapid non-radiative recombination, thus leading to shorter lifetimes. Interestingly, our pXRD data (**Figure 4.6**) suggest that the structure of the InP MSCs is maintained at low equivalents of dopant. Instead, we posit that the addition of our dopant solution causes loss of indium carboxylate with concerted coordination of the dopant metal halide complex, followed by rearrangement of this new mixed carboxylate-halide ligand shell as the dopant migrates to the core, leading to a cluster with less highly localized frontier orbitals. This analysis is consistent with previous reports by our group detailing the liberation of indium carboxylates upon addition of amine ligands in a formal L-assisted Z-type ligand displacement reaction.[64,65] This mechanism is further supported by previous theoretical studies showing that the initial reactivity of InP increases with decreasing size and In-In separation, and that doping of aliovalent ions is more favorable following ligand removal.[53,66,67]

Upon addition of 37 equivalents of coinage metal precursor, the original bleach and photoinduced absorption profile is eliminated. Instead, the TA signal is replaced by a rapid, broad photoinduced absorption feature as seen in **Figure 4.12A-C**, indicating that the new clusters have an excited state absorption coefficient greater than the ground state absorption coefficient at these wavelengths, similar to coinage metal chalcogenides.[68–70]

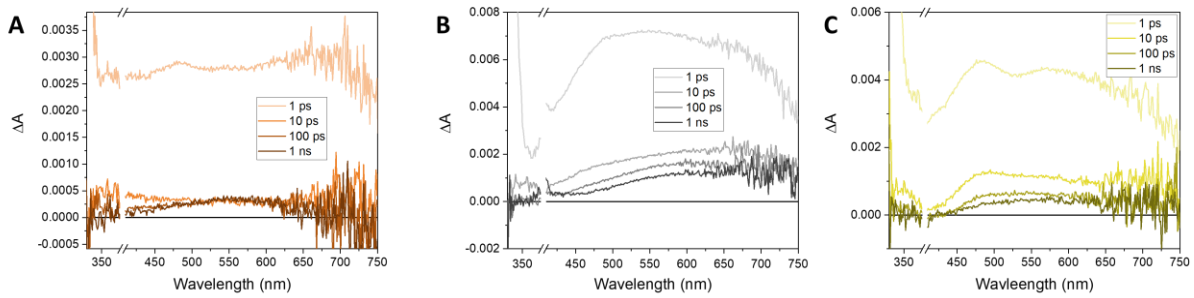

Figure 4.12. Transient absorption spectra of InP MSCs with addition of 37 equivalencies of cation. A) $CuCl_2$. B) AgCl. C) $AuCl_3$

4.3.4 Conversion reactions with doped and converted clusters

Further interest in these coinage metal-containing clusters derives from their utility as single source precursors for the formation of larger nanocrystals.[2,71–73] After conversion of the $In_{37}P_{20}$ MSCs to coinage metal phosphide clusters, we next examined if these materials could be used for the formation of larger nanocrystals. We hypothesized that a hot-injection synthesis can be used to overcome the energic barrier keeping MSCs in their metastable state and allow them to convert to larger, more stable nanocrystals. Indeed, upon injecting MSCs treated with 1 equivalent of copper into ODE heated to 300 °C, we obtain Cu^+:InP quantum dots. This can be observed in **Figure 4.13A** by the broadened absorption profile along with broad, NIR luminescence, mirroring previously reported Cu^+:InP systems.[35,36,60] Furthermore, these samples show highly similar diffraction patterns to undoped InP, suggesting that the zincblende InP lattice is retained (**Figure 4.13B**).

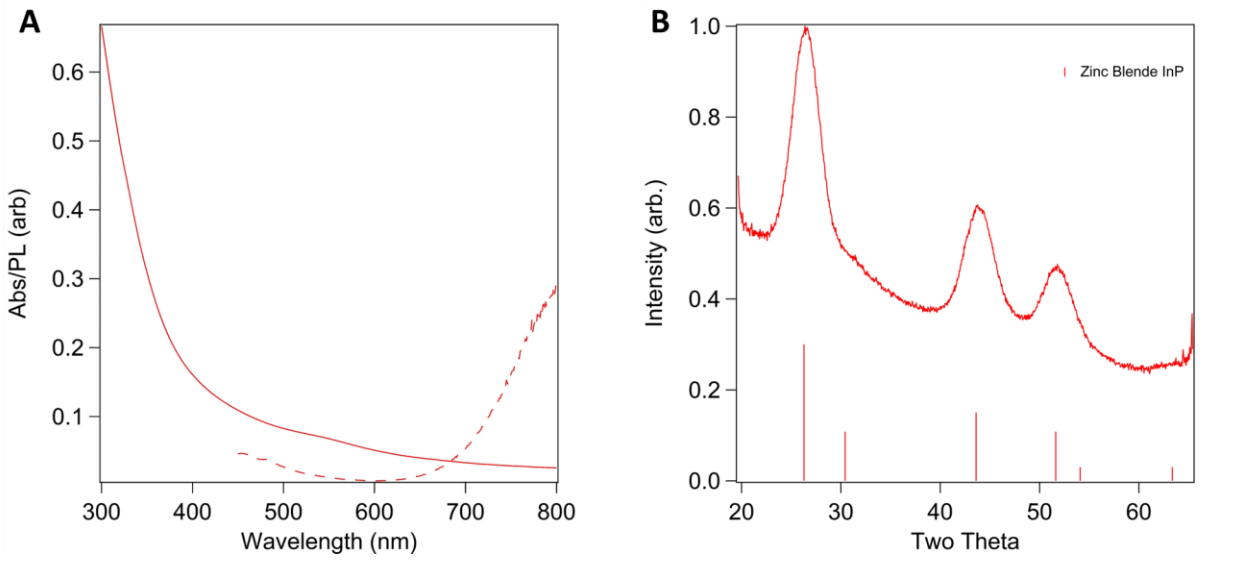

Figure 4.13. Doped InP dots formed by conversion of 1 Eq Cu-MSCs A) UV-Vis absorption and PL spectra showing broadened, redshifted emission. B) pXRD of resultant Cu^{+}:InP with InP reference.

However, using the fully cation exchanged clusters yields different products. Upon conversion of the MSCs that were treated with 37 equivalents of copper, the major product is Cu_3P nanocrystals, confirmed via pXRD analysis as shown in **Figure 4.14A**. TEM analysis (**Figure 4.14D**) shows formation of larger (12.5 ± 0.5 nm) oblong nanocrystals. Hot injection of the MSCs treated with 37 equivalents of silver leads to greater structural transformations of the cluster, with the pXRD in **Figure 4.14B** showing the formation of Ag_3P in the tetragonal phase. Excitingly, this is the first report of this material on the nanoscale to the best of our knowledge.[74] TEM analysis of these new Ag_3P nanocrystals shows an average size of 3.8 ± 0.2 nm (**Figure 4.14E**) suggesting much less growth relative to the Cu-P system. Performing a hot-injection reaction of the MSCs treated with 37 equivalents of Au with identical reaction parameters does not form nanocrystals of a new morphology but instead grows the cluster-based structure, as seen

by the peak sharpening in the pXRD (**Figure 4.14C**) and growth to 3.8 ± 0.3 nm in size as seen via TEM (**Figure 4.14F**).

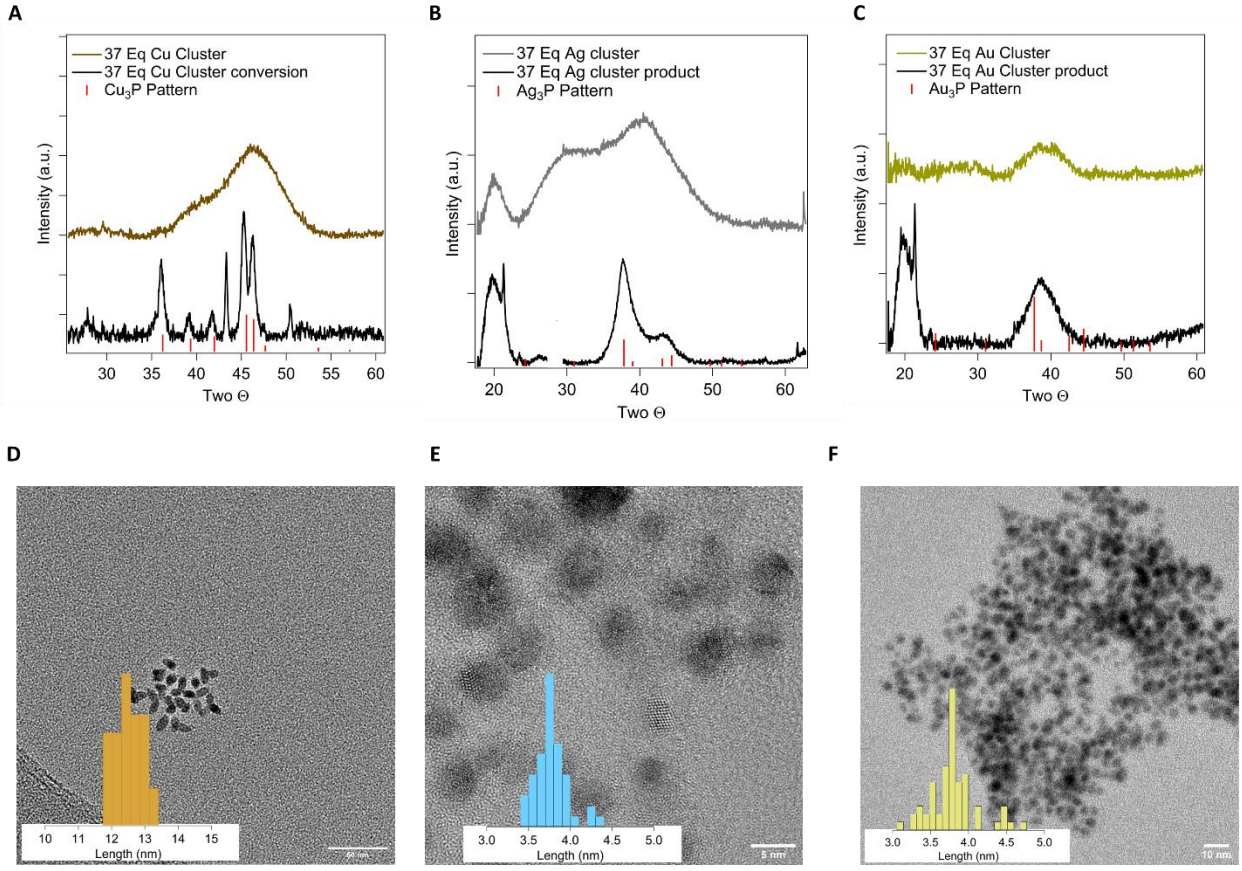

Figure 4.14. A) pXRD of Cu_3P nanocrystals resulting from the hot injection of MSCs treated with 37 equivalents of Cu. The peak at 43 corresponds to the formation of a small fraction of large Cu nanocrystals. B) pXRD of MSCs treated with 37 equivalents of Ag before and after hot injection reaction (the Si 111 peak at 28.4 has been removed from the analysis for clarity). C) pXRD of MSCs treated with 37 equivalents of Au before and after hot injection reaction. D) TEM of MSCs treated with 37 equivalents of Cu after hot injection reaction (scale bar is 50 nm) E) TEM of MSCs treated with 37 equivalents of Ag after hot injection reaction (scale bar is 5 nm). F) TEM of MSCs treated with 37 equivalents of Au after hot injection reaction (scale bar is 10 nm).

Interestingly, we do not observe LSPR features in the NIR region of the absorption spectrum (**Figure 4.15**).

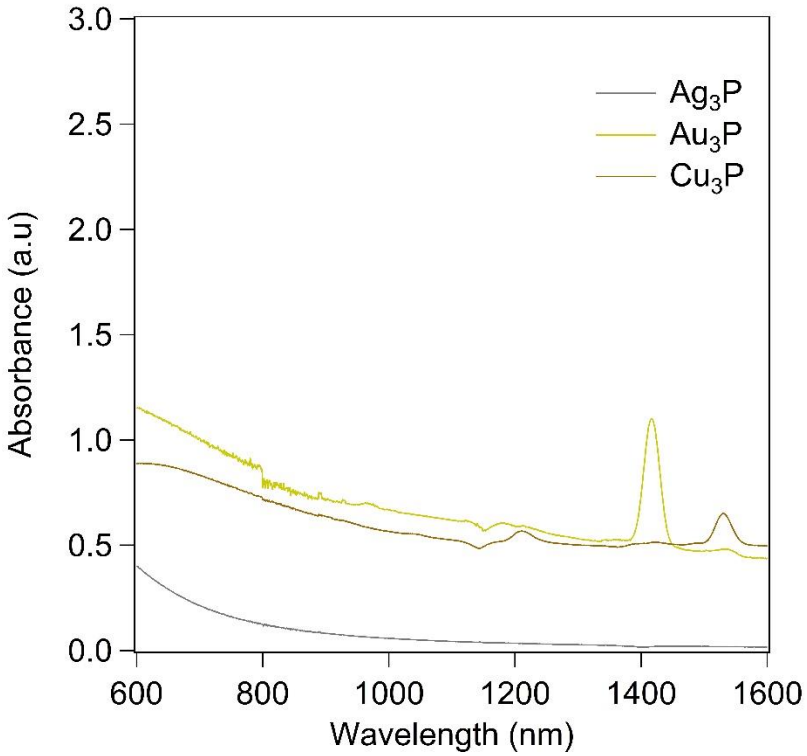

Figure 4.15. NIR absorption spectra of samples resulting from the thermolysis of InP MSCs treated with 37 equivalents of coinage metal.

4.3.5 Conclusions

We have demonstrated the room temperature conversion of $In_{37}P_{20}$ MSCs into doped InP clusters and $M_{3-x}P$ (M = Cu, Ag, Au) nanocrystals through exchange of indium using a coinage metal salt. From a combination of absorption spectroscopy and pXRD data we determined that the MSC core undergoes doping without significant structural changes upon addition of 1 to 5 equivalents of coinage metal. However, at 37 equivalents of added coinage metal, we observe the complete transformation into new metal phosphide clusters with no evidence for remaining indium in the core. Transient absorption spectroscopy of MSCs exposed to 1 equivalent of

coinage metal reactant suggests that removal of some excess surface In is required before the transformation of the inorganic core can occur, while further exchange exhibits characteristics expected in coinage metal phosphides. Hot injection reactions of these new coinage metal phosphide clusters form larger metal phosphide nanocrystals that reflect the cluster compositions. Notably, colloidal nanocrystals of Ag_3P and Au_3P have not been previously reported. This work illustrates that cation exchange can be utilized not only as a method of studying structural transformations in magic sized clusters, but also as an approach to expanding the library of magic sized clusters that serve as intermediates in the formation of a variety of nanocrystals, including metastable or otherwise difficult to form species.

4.4 Experimental Details

4.4.1 General Considerations

All glassware was dried in a 160 °C oven overnight prior to use. All reactions were run under an inert atmosphere of nitrogen using a glovebox or standard Schlenk line techniques. Indium (III) acetate (99.99%), myristic acid (99%), copper (II) chloride (≥98%), copper (I) chloride (97%), silver (I) chloride(99%), gold (III) chloride(99%), gold (I) chloride(99.9%), tributylphosphine (TBP), anhydrous acetonitrile, and anhydrous ethanol were purchased from Millipore-Sigma, stored in a nitrogen glovebox or desiccator, and used without further purification. Oleylamine and toluene were purchased from Sigma Aldrich Chemical Co., dried over CaH_2, distilled, and stored over 4 Å sieves in a nitrogen glovebox.

4.4.2 Synthesis of InP-MSCs.

InP MSCs were synthesized according to previously established procedures established by Gary et al. [2] In brief, indium acetate and myristic acid were heated at 110 °C overnight under reduced pressure. Dry toluene was added to the backfilled reaction flask the next day and 465uL of PTMS3 in 10mL of toluene was added. Cluster growth was allowed to proceed for 30 minutes. Purification was achieved via 4 successive cycles of precipitation/redissolution with toluene and acetonitrile as the solvent and antisolvent respectively.

4.4.3 Cation exchange involving InP-MSCs.

Cation exchange was carried out at room temperature in an inert atmosphere glovebox. In a typical exchange reaction, ~10mg of InP MSC was suspended in 1mL toluene and a solution of $CuCl_2$, CuCl, AgCl, $AuCl_3$, or AuCl solubilized in toluene and oleylamine (3:2 ratio) was added to the solution. These cation solutions were made at a concentration of 121mM and added in quantities between 5uL (1 eq) and 185uL (37eq) to the solution of InP MSCs and allowed to stir overnight. Cation exchanged clusters were then purified via gel permeation chromatography as described in Shen et al.[75]

4.4.4 Conversion reactions involving cation exchanged InP-MSCs.

Conversion reactions were carried out by suspending 10 mg of cation exchanged clusters in 1 mL ODE, after which this solution was injected into a solution of 5 mL ODE heated to 300 °C. This reaction was allowed to proceed for 30 min at 300 °C. After the reaction was cooled it was brought into an inert atmosphere glovebox and purified using 3 successive cycles of precipitation/dissolution with toluene/ethanol as the solvent/antisolvent.

4.4.5 Characterization techniques

UV-Vis absorption spectroscopy was carried out upon a Agilent Carry 5000 spectrophotometer. X-ray photoelectron spectroscopy (XPS) was conducted on a Kratos AXIS Ultra DLD located in the University of Washington Molecular Analysis Facility. The samples were drop-cast onto a silicon wafer from toluene in a N2 glovebox. Pass energy for survey spectra (to calculate composition) was 150 eV. Data point spacing was 1.0 eV per step for survey spectra and 0.4 eV per step for detailed spectra. Pass energy for high-resolution spectra was 50 eV, with a data point spacing of 0.065 eV. CasaXPS data analysis software was used to fit high resolution spectra. Transient Absorption measurements were performed using an HELIOS unit from Ultrafast Systems at the University of Washington's Molecular Analysis Facility. The pump wavelength was 365nm and the power was measured as 100-200μW through a 200μm pinhole. The probe white light was generated via the use of a sapphire crystal. Transmission electron microscopy (TEM) images were collected on an FEI Tecnai G2 F20 microscope at 200 kV in the University of Washington Molecular Analysis Facility. TEM samples were prepared by spotting 5 μL of a dilute solution of QDs dispersed in toluene onto an ultrathin carbon on holey carbon support film purchased from Ted Pella. Powder x-ray diffraction data was collected on a Bruker D8 Discover diffractometer with Cu anode microfocus x-ray source and Pilatus 100k large-area 2D detector. Samples were prepared by dissolving or suspending the sample in a minimal amount of toluene and repeatedly dropcasting 3 μL of the solution onto a Si wafer to build up a thick film or layer of sample. The beam for the measurement was collimated to a 1 mm beam diameter. Collection times were 360 seconds per step (5.5° step size). Raw diffraction data was processed using Bruker DIFFRAC.EVA software. For PDF analysis, MSC samples were first dried in an inert nitrogen atmosphere glovebox and sealed in quartz capillaries. X-ray total scattering data

were collected on NSLS-II beamline 28-ID-1 at Brookhaven National Laboratory. Sample scans consisted of 300 1-second exposures using 74.5 keV incident beam energy. Background subtraction and transmission correction were applied to each scan. Sample transmission ranging from 67-84% was measured using a silicon photodiode with an impedance amplifying circuit.

.

4.5 REFERENCES

(1) Cunningham, P. D.; Coropceanu, I.; Mulloy, K.; Cho, W.; Talapin, D. V. Quantized Reaction Pathways for Solution Synthesis of Colloidal ZnSe Nanostructures: A Connection between Clusters, Nanowires, and Two-Dimensional Nanoplatelets. *ACS Nano* **2020**, *14* (4), 3847–3857. https://doi.org/10.1021/acsnano.9b09051.

(2) Gary, D. C.; Terban, M. W.; Billinge, S. J. L.; Cossairt, B. M. Two-Step Nucleation and Growth of InP Quantum Dots via Magic-Sized Cluster Intermediates. *Chem. Mater.* **2015**, *27* (4), 1432–1441. https://doi.org/10.1021/acs.chemmater.5b00286.

(3) Friedfeld, M. R.; Stein, J. L.; Cossairt, B. M. Main-Group-Semiconductor Cluster Molecules as Synthetic Intermediates to Nanostructures. *Inorganic Chemistry* **2017**, *56* (15), 8689–8697. https://doi.org/10.1021/acs.inorgchem.7b00291.

(4) Fenton, J. L.; Steimle, B. C.; Schaak, R. E. Tunable Intraparticle Frameworks for Creating Complex Heterostructured Nanoparticle Libraries. *Science* **2018**, *360* (6388), 513–517. https://doi.org/10.1126/science.aar5597.

(5) Steimle, B. C.; Fenton, J. L.; Schaak, R. E. Rational Construction of a Scalable Heterostructured Nanorod Megalibrary. *Science* **2020**, *367* (6476), 418–424. https://doi.org/10.1126/science.aaz1172.

(6) Stone, D.; Koley, S.; Remennik, S.; Asor, L.; Panfil, Y. E.; Naor, T.; Banin, U. Luminescent Anisotropic Wurtzite InP Nanocrystals. *Nano Lett.* **2021**, *21* (23), 10032–10039. https://doi.org/10.1021/acs.nanolett.1c03719.

(7) De Trizio, L.; Gaspari, R.; Bertoni, G.; Kriegel, I.; Moretti, L.; Scotognella, F.; Maserati, L.; Zhang, Y.; Messina, G. C.; Prato, M.; Marras, S.; Cavalli, A.; Manna, L. $Cu_{3-x}P$ Nanocrystals as a Material Platform for Near-Infrared Plasmonics and Cation Exchange Reactions. *Chemistry of Materials* **2015**, *27* (3), 1120–1128. https://doi.org/10.1021/cm5044792.

(8) Beberwyck, B. J.; Alivisatos, A. P. Ion Exchange Synthesis of III–V Nanocrystals. *J. Am. Chem. Soc.* **2012**, *134* (49), 19977–19980. https://doi.org/10.1021/ja309416c.

(9) White, S. L.; Banerjee, P.; Chakraborty, I.; Jain, P. K. Ion Exchange Transformation of Magic-Sized Clusters. *Chem. Mater.* **2016**, *28* (22), 8391–8398. https://doi.org/10.1021/acs.chemmater.6b03882.

(10) Stein, J. L.; Steimle, M. I.; Terban, M. W.; Petrone, A.; Billinge, S. J. L.; Li, X.; Cossairt, B. M. Cation Exchange Induced Transformation of InP Magic-Sized Clusters. *Chem. Mater.* **2017**, *29* (18), 7984–7992. https://doi.org/10.1021/acs.chemmater.7b03075.

(11) He, L.; Luan, C.; Liu, S.; Chen, M.; Rowell, N.; Wang, Z.; Li, Y.; Zhang, C.; Lu, J.; Zhang, M.; Liang, B.; Yu, K. Transformations of Magic-Size Clusters via Precursor Compound Cation Exchange at Room Temperature. *J. Am. Chem. Soc.* **2022**, *144* (41), 19060–19069. https://doi.org/10.1021/jacs.2c07972.

(12) Muckel, F.; Yang, J.; Lorenz, S.; Baek, W.; Chang, H.; Hyeon, T.; Bacher, G.; Fainblat, R. Digital Doping in Magic-Sized CdSe Clusters. *ACS Nano* **2016**, *10* (7), 7135–7141. https://doi.org/10.1021/acsnano.6b03348.

(13) Yang, J.; Fainblat, R.; Kwon, S. G.; Muckel, F.; Yu, J. H.; Terlinden, H.; Kim, B. H.; Iavarone, D.; Choi, M. K.; Kim, I. Y.; Park, I.; Hong, H.-K.; Lee, J.; Son, J. S.; Lee, Z.; Kang, K.; Hwang, S.-J.; Bacher, G.; Hyeon, T. Route to the Smallest Doped Semiconductor: Mn2+-Doped (CdSe)13 Clusters. *J. Am. Chem. Soc.* **2015**, *137* (40), 12776–12779. https://doi.org/10.1021/jacs.5b07888.

(14) Pittala, S.; Mortelliti, M. J.; Kato, F.; Kittilstved, K. R. Substitution of Co2+ Ions into CdS-Based Molecular Clusters. *Chem. Commun.* **2015**, *51* (96), 17096–17099. https://doi.org/10.1039/C5CC06138E.

(15) Eilers, J.; Groeneveld, E.; de Mello Donegá, C.; Meijerink, A. Optical Properties of Mn-Doped ZnTe Magic Size Nanocrystals. *J. Phys. Chem. Lett.* **2012**, *3* (12), 1663–1667. https://doi.org/10.1021/jz300300g.

(16) Fainblat, R.; Barrows, C. J.; Gamelin, D. R. Single Magnetic Impurities in Colloidal Quantum Dots and Magic-Size Clusters. *Chem. Mater.* **2017**, *29* (19), 8023–8036. https://doi.org/10.1021/acs.chemmater.7b03195.

(17) Lin, J.; Zhang, Q.; Wang, L.; Liu, X.; Yan, W.; Wu, T.; Bu, X.; Feng, P. Atomically Precise Doping of Monomanganese Ion into Coreless Supertetrahedral Chalcogenide Nanocluster Inducing Unusual Red Shift in Mn2+ Emission. *J. Am. Chem. Soc.* **2014**, *136* (12), 4769–4779. https://doi.org/10.1021/ja501288x.

(18) Friedfeld, M. R.; Stein, J. L.; Johnson, D. A.; Park, N.; Henry, N. A.; Enright, M. J.; Mocatta, D.; Cossairt, B. M. Effects of Zn2+ and Ga3+ Doping on the Quantum Yield of Cluster-Derived InP Quantum Dots. *J. Chem. Phys.* **2019**, *151* (19), 194702. https://doi.org/10.1063/1.5126971.

(19) Rivest, J. B.; Jain, P. K. Cation Exchange on the Nanoscale: An Emerging Technique for New Material Synthesis, Device Fabrication, and Chemical Sensing. *Chem. Soc. Rev.* **2012**, *42* (1), 89–96. https://doi.org/10.1039/C2CS35241A.

(20) Manna, G.; Bose, R.; Pradhan, N. Semiconducting and Plasmonic Copper Phosphide Platelets. *Angewandte Chemie International Edition* **2013**, *52* (26), 6762–6766. https://doi.org/10.1002/anie.201210277.

(21) Rachkov, A. G.; Schimpf, A. M. Colloidal Synthesis of Tunable Copper Phosphide Nanocrystals. *Chem. Mater.* **2021**, *33* (4), 1394–1406. https://doi.org/10.1021/acs.chemmater.0c04460.

(22) Bertoni, G.; Ramasse, Q.; Brescia, R.; De Trizio, L.; De Donato, F.; Manna, L. Direct Quantification of Cu Vacancies and Spatial Localization of Surface Plasmon Resonances in Copper Phosphide Nanocrystals. *ACS Materials Lett.* **2019**, *1* (6), 665–670. https://doi.org/10.1021/acsmaterialslett.9b00412.

(23) Tian, J.; Liu, Q.; Cheng, N.; Asiri, A. M.; Sun, X. Self-Supported Cu3P Nanowire Arrays as an Integrated High-Performance Three-Dimensional Cathode for Generating Hydrogen from Water. *Angewandte Chemie International Edition* **2014**, *53* (36), 9577–9581. https://doi.org/10.1002/anie.201403842.

(24) Zhou, X.; Zhou, X.; Liu, L.; Chen, H.; Hu, X.; Qian, J.; Huang, D.; Zhang, B.; Tang, J. Self-Supported Cu_3P Nanowire Electrode as an Efficient Electrocatalyst for the Oxygen Evolution Reaction. *RSC Adv.* **2021**, *11* (54), 34137–34143. https://doi.org/10.1039/D1RA05526G.

(25) Laursen, A. B.; Calvinho, K. U. D.; Goetjen, T. A.; Yap, K. M. K.; Hwang, S.; Yang, H.; Garfunkel, E.; Dismukes, G. C. CO2 Electro-Reduction on Cu3P: Role of Cu(I) Oxidation State and Surface Facet Structure in C1-Formate Production and H2 Selectivity. *Electrochimica Acta* **2021**, *391*, 138889. https://doi.org/10.1016/j.electacta.2021.138889.

(26) Downes, C. A.; Libretto, N. J.; Harman-Ware, A. E.; Happs, R. M.; Ruddy, D. A.; Baddour, F. G.; Ferrell III, J. R.; Habas, S. E.; Schaidle, J. A. Electrocatalytic CO2 Reduction over Cu3P Nanoparticles Generated via a Molecular Precursor Route. *ACS Appl. Energy Mater.* **2020**, *3* (11), 10435–10446. https://doi.org/10.1021/acsaem.0c01360.

(27) Carenco, S.; Florea, I.; Ersen, O.; Boissière, C.; Mézailles, N.; Sanchez, C. Towards Nanoscaled Gold Phosphides: Surface Passivation and Growth of Composite Nanostructures. *New J. Chem.* **2013**, *37* (4), 1231–1237. https://doi.org/10.1039/C3NJ41037D.

(28) Okamoto, H.; Massalski, T. B. The Au−P (Gold-Phosphorus) System. *Bulletin of Alloy Phase Diagrams* **1984**, *5* (5), 490–491. https://doi.org/10.1007/BF02872903.

(29) Sweeney, C. M.; Stamm, K. L.; Brock, S. L. On the Feasibility of Phosphide Generation from Phosphate Reduction: The Case of Rh, Ir, and Ag. *Journal of Alloys and Compounds* **2008**, *448* (1), 122–127. https://doi.org/10.1016/j.jallcom.2006.10.035.

(30) Li, H.; Wen, P.; Itanze, D. S.; Hood, Z. D.; Ma, X.; Kim, M.; Adhikari, S.; Lu, C.; Dun, C.; Chi, M.; Qiu, Y.; Geyer, S. M. RETRACTED ARTICLE: Colloidal Silver Diphosphide (AgP2) Nanocrystals as Low Overpotential Catalysts for CO2 Reduction to Tunable Syngas. *Nat Commun* **2019**, *10* (1), 5724. https://doi.org/10.1038/s41467-019-13388-8.

(31) Vaughey, J. T.; Fransson, L.; Swinger, H. A.; Edström, K.; Thackeray, M. M. Alternative Anode Materials for Lithium-Ion Batteries: A Study of Ag3Sb. *Journal of Power Sources* **2003**, *119–121*, 64–68. https://doi.org/10.1016/S0378-7753(03)00126-5.

(32) Ag (Silver) Binary Alloy Phase Diagrams. **2016**. https://doi.org/10.31399/asm.hb.v03.a0006143.

(33) Cipriani, C.; Corazza, M.; Mazzetti, G. Reinvestigation of Natural Silver Antimonides. *ejm* **1997**, *8* (6), 1347–1350. https://doi.org/10.1127/ejm/8/6/1347.

(34) Henkes, A. E.; Vasquez, Y.; Schaak, R. E. Converting Metals into Phosphides: A General Strategy for the Synthesis of Metal Phosphide Nanocrystals. *J. Am. Chem. Soc.* **2007**, *129* (7), 1896–1897. https://doi.org/10.1021/ja068502l.

(35) Knowles, K. E.; Hartstein, K. H.; Kilburn, T. B.; Marchioro, A.; Nelson, H. D.; Whitham, P. J.; Gamelin, D. R. Luminescent Colloidal Semiconductor Nanocrystals Containing Copper: Synthesis, Photophysics, and Applications. *Chem. Rev.* **2016**, *116* (18), 10820–10851. https://doi.org/10.1021/acs.chemrev.6b00048.

(36) Knowles, K. E.; Nelson, H. D.; Kilburn, T. B.; Gamelin, D. R. *Singlet–Triplet Splittings in the Luminescent Excited States of Colloidal Cu+:CdSe, Cu+:InP, and CuInS2 Nanocrystals: Charge-Transfer Configurations and Self-Trapped Excitons*. https://doi.org/10.1021/jacs.5b08547.

(37) Nelson, H. D.; Li, X.; Gamelin, D. R. Computational Studies of the Electronic Structures of Copper-Doped CdSe Nanocrystals: Oxidation States, Jahn–Teller Distortions, Vibronic Bandshapes, and Singlet–Triplet Splittings. *J. Phys. Chem. C* **2016**, *120* (10), 5714–5723. https://doi.org/10.1021/acs.jpcc.5b11319.

(38) Gary, D. C.; Flowers, S. E.; Kaminsky, W.; Petrone, A.; Li, X.; Cossairt, B. M. Single-Crystal and Electronic Structure of a 1.3 Nm Indium Phosphide Nanocluster. *J. Am. Chem. Soc.* **2016**, *138* (5), 1510–1513. https://doi.org/10.1021/jacs.5b13214.

(39) Bhuse, V. M.; Hankare, P. P.; Garadkar, K. M.; Khomane, A. S. A Simple, Convenient, Low Temperature Route to Grow Polycrystalline Copper Selenide Thin Films. *Materials Chemistry and Physics* **2003**, *80* (1), 82–88. https://doi.org/10.1016/S0254-0584(02)00306-1.

(40) Liu, Y.; Liu, M.; Swihart, M. T. Plasmonic Copper Sulfide-Based Materials: A Brief Introduction to Their Synthesis, Doping, Alloying, and Applications. *J. Phys. Chem. C* **2017**, *121* (25), 13435–13447. https://doi.org/10.1021/acs.jpcc.7b00894.

(41) White, S. L.; Banerjee, P.; Jain, P. K. Liquid-like Cationic Sub-Lattice in Copper Selenide Clusters. *Nat Commun* **2017**, *8* (1), 14514. https://doi.org/10.1038/ncomms14514.

(42) Liu, Z.; Zhong, Y.; Shafei, I.; Jeong, S.; Wang, L.; Nguyen, H. T.; Sun, C.-J.; Li, T.; Chen, J.; Chen, L.; Losovyj, Y.; Gao, X.; Ma, W.; Ye, X. Broadband Tunable Mid-Infrared Plasmon Resonances in Cadmium Oxide Nanocrystals Induced by Size-Dependent Nonstoichiometry. *Nano Lett.* **2020**, *20* (4), 2821–2828. https://doi.org/10.1021/acs.nanolett.0c00542.

(43) Schimpf, A. M.; Thakkar, N.; Gunthardt, C. E.; Masiello, D. J.; Gamelin, D. R. Charge-Tunable Quantum Plasmons in Colloidal Semiconductor Nanocrystals. *ACS Nano* **2014**, *8* (1), 1065–1072. https://doi.org/10.1021/nn406126u.

(44) Jharimune, S.; Sathe, A. A.; Rioux, R. M. Thermochemical Measurements of Cation Exchange in CdSe Nanocrystals Using Isothermal Titration Calorimetry. *Nano Lett.* **2018**, *18* (11), 6795–6803. https://doi.org/10.1021/acs.nanolett.8b02661.

(45) Hafiz, S. B.; Scimeca, M. R.; Zhao, P.; Paredes, I. J.; Sahu, A.; Ko, D.-K. Silver Selenide Colloidal Quantum Dots for Mid-Wavelength Infrared Photodetection. *ACS Appl. Nano Mater.* **2019**, *2* (3), 1631–1636. https://doi.org/10.1021/acsanm.9b00069.

(46) León-Velázquez, M. S.; Irizarry, R.; Castro-Rosario, M. E. Nucleation and Growth of Silver Sulfide Nanoparticles. *J. Phys. Chem. C* **2010**, *114* (13), 5839–5849. https://doi.org/10.1021/jp911238a.

(47) Akamatsu, K.; Takei, S.; Mizuhata, M.; Kajinami, A.; Deki, S.; Takeoka, S.; Fujii, M.; Hayashi, S.; Yamamoto, K. Preparation and Characterization of Polymer Thin Films Containing Silver and Silver Sulfide Nanoparticles. *Thin Solid Films* **2000**, *359* (1), 55–60. https://doi.org/10.1016/S0040-6090(99)00684-7.

(48) Mourdikoudis, S.; Liz-Marzán, L. M. Oleylamine in Nanoparticle Synthesis. *Chem. Mater.* **2013**, *25* (9), 1465–1476. https://doi.org/10.1021/cm4000476.

(49) Mundy, M. E.; Eagle, F. W.; Hughes, K. E.; Gamelin, D. R.; Cossairt, B. M. Synthesis and Spectroscopy of Emissive, Surface-Modified, Copper-Doped Indium Phosphide Nanocrystals. *ACS Materials Lett.* **2020**, *2* (6), 576–581. https://doi.org/10.1021/acsmaterialslett.0c00112.

(50) Eagle, F. W.; Harvey, S.; Beck, R.; Li, X.; Gamelin, D. R.; Cossairt, B. M. Enhanced Charge Transfer from Coinage Metal Doped InP Quantum Dots. *ACS Nanosci. Au* **2023**. https://doi.org/10.1021/acsnanoscienceau.3c00029.

(51) Kwon, Y.; Oh, J.; Lee, E.; Lee, S. H.; Agnes, A.; Bang, G.; Kim, J.; Kim, D.; Kim, S. Evolution from Unimolecular to Colloidal-Quantum-Dot-like Character in Chlorine or Zinc Incorporated InP Magic Size Clusters. *Nat Commun* **2020**, *11* (1), 3127. https://doi.org/10.1038/s41467-020-16855-9.

(52) Okuda, Y.; Tsurumaki, E.; Oh, J.; Sung, J.; Kim, D.; Osuka, A. A Directly Fused Subporphyrin Dimer with a Wavelike Structure. *Angewandte Chemie International Edition* **2016**, *55* (32), 9212–9215. https://doi.org/10.1002/anie.201603759.

(53) Gary, D. C.; Petrone, A.; Li, X.; Cossairt, B. M. Investigating the Role of Amine in InP Nanocrystal Synthesis: Destabilizing Cluster Intermediates by Z-Type Ligand Displacement. *Chem. Commun.* **2016**, *53* (1), 161–164. https://doi.org/10.1039/C6CC07952K.

(54) Anderson, N. C.; Hendricks, M. P.; Choi, J. J.; Owen, J. S. Ligand Exchange and the Stoichiometry of Metal Chalcogenide Nanocrystals: Spectroscopic Observation of Facile Metal-Carboxylate Displacement and Binding. *J. Am. Chem. Soc.* **2013**, *135* (49), 18536–18548. https://doi.org/10.1021/ja4086758.

(55) Zhao, Q.; Kulik, H. J. Electronic Structure Origins of Surface-Dependent Growth in III–V Quantum Dots. *Chem. Mater.* **2018**, *30* (20), 7154–7165. https://doi.org/10.1021/acs.chemmater.8b03125.

(56) Taylor, M. G.; Kulik, H. J. Mapping the Origins of Surface- and Chemistry-Dependent Doping Trends in III–V Quantum Dots with Density Functional Theory. *Chem. Mater.* **2021**, *33* (17), 7113–7123. https://doi.org/10.1021/acs.chemmater.1c02556.

(57) Shim, D.; Kang, J. Enhanced Reactivity of Magic-Sized Inorganic Clusters by Engineering the Surface Ligand Networks. *Chem. Mater.* **2023**, *35* (2), 700–708. https://doi.org/10.1021/acs.chemmater.2c03394.

(58) Zhang, F.; Chen, K.; Jiang, X.; Wang, Y.; Ge, Y.; Wu, L.; Xu, S.; Bao, Q.; Zhang, H. Nonlinear Optical Absorption and Ultrafast Carrier Dynamics of Copper Antimony Sulfide Semiconductor Nanocrystals. *J. Mater. Chem. C* **2018**, *6* (33), 8977–8983. https://doi.org/10.1039/C8TC01606B.

(59) Shi, G.; He, C.; Li, Y.; Zou, R.; Zhang, X.; Wang, Y.; Yang, K.; Song, Y.; Wang, C. H. Excited-State Nonlinearity Measurements of $ZnPcBr_4$/DMSO. *J. Opt. Soc. Am. B, JOSAB* **2009**, *26* (4), 754–761. https://doi.org/10.1364/JOSAB.26.000754.

(60) Kriegel, I.; Jiang, C.; Rodríguez-Fernández, J.; Schaller, R. D.; Talapin, D. V.; da Como, E.; Feldmann, J. Tuning the Excitonic and Plasmonic Properties of Copper Chalcogenide Nanocrystals. *J. Am. Chem. Soc.* **2012**, *134* (3), 1583–1590. https://doi.org/10.1021/ja207798q.

(61) *Materials Data on Cu3P by Materials Project*; mp-7463; Lawrence Berkeley National Lab. (LBNL), Berkeley, CA (United States). LBNL Materials Project, 2020. https://doi.org/10.17188/1288438.

(62) *Materials Data on PAu3 by Materials Project*; mp-1186369; Lawrence Berkeley National Lab. (LBNL), Berkeley, CA (United States). LBNL Materials Project, 2020. https://doi.org/10.17188/1695217.

(63) White, S. L.; Smith, J. G.; Behl, M.; Jain, P. K. Co-Operativity in a Nanocrystalline Solid-State Transition. *Nat Commun* **2013**, *4* (1), 2933. https://doi.org/10.1038/ncomms3933.

(64) Yao, Y.; Lynch, R.; Robinson, R. D. Mass Spectroscopy Study of the Intermediate Magic-Size Cluster Species during Cooperative Cation Exchange. *The Journal of Chemical Physics* **2023**, *159* (1), 014704. https://doi.org/10.1063/5.0151904.

(65) Zhang, X.; Kim, D.; Guo, X.; Zhu, Y.; Lee, L. Y. S. Impacts of Boron Doping on the Atomic Structure, Stability, and Photocatalytic Activity of Cu3P Nanocrystals. *Applied Catalysis B: Environmental* **2021**, *298*, 120515. https://doi.org/10.1016/j.apcatb.2021.120515.

(66) Chowdari, B. V. R.; Mok, K. F.; Xie, J. M.; Gopalakrishnan, R. Spectroscopic and Electrical Studies of Silver Sulfophosphate Glasses. *Journal of Non-Crystalline Solids* **1993**, *160* (1), 73–81. https://doi.org/10.1016/0022-3093(93)90286-7.

(67) Kitagawa, H.; Kojima, N.; Nakajima, T. Studies of Mixed-Valence States in Three-Dimensional Halogen-Bridged Gold Compounds, Cs2AuIAuIIIX6, (X = Cl, Br or I). Part 2. X-Ray Photoelectron Spectroscopic Study. *J. Chem. Soc., Dalton Trans.* **1991**, No. 11, 3121–3125. https://doi.org/10.1039/DT9910003121.

(68) Wang, X.; Fei, Y.; Li, W.; Yi, L.; Feng, B.; Pan, Y.; Hu, W.; Li, C. M. Gold-Incorporated Cobalt Phosphide Nanoparticles on Nitrogen-Doped Carbon for Enhanced Hydrogen Evolution Electrocatalysis. *ACS Appl. Mater. Interfaces* **2020**, *12* (14), 16548–16556. https://doi.org/10.1021/acsami.0c02076.

(69) Tao, Y.; Yelon, A.; Sacher, E.; Lu, Z. H.; Graham, M. J. S-passivated InP (100)-(1×1) Surface Prepared by a Wet Chemical Process. *Appl. Phys. Lett.* **1992**, *60* (21), 2669–2671. https://doi.org/10.1063/1.106890.

(70) Freeland, B. H.; Habeeb, J. J.; Tuck, D. G. Coordination Compounds of Indium. Part XXXIII. X-Ray Photoelectron Spectroscopy of Neutral and Anionic Indium Halide Species. *Can. J. Chem.* **1977**, *55* (9), 1527–1532. https://doi.org/10.1139/v77-213.

(71) Wang, Y.; Zhang, Y.; Wang, F.; Giblin, D. E.; Hoy, J.; Rohrs, H. W.; Loomis, R. A.; Buhro, W. E. The Magic-Size Nanocluster (CdSe)34 as a Low-Temperature Nucleant for Cadmium Selenide Nanocrystals; Room-Temperature Growth of Crystalline Quantum Platelets. *Chem. Mater.* **2014**, *26* (7), 2233–2243. https://doi.org/10.1021/cm404068e.

(72) Cumberland, S. L.; Hanif, K. M.; Javier, A.; Khitrov, G. A.; Strouse, G. F.; Woessner, S. M.; Yun, C. S. Inorganic Clusters as Single-Source Precursors for Preparation of CdSe, ZnSe, and CdSe/ZnS Nanomaterials. *Chem. Mater.* **2002**, *14* (4), 1576–1584. https://doi.org/10.1021/cm010709k.

(73) Li, L.; Zhang, J.; Zhang, M.; Rowell, N.; Zhang, C.; Wang, S.; Lu, J.; Fan, H.; Huang, W.; Chen, X.; Yu, K. Fragmentation of Magic-Size Cluster Precursor Compounds into Ultrasmall CdS Quantum Dots with Enhanced Particle Yield at Low Temperatures. *Angewandte Chemie* **2020**, *132* (29), 12111–12119. https://doi.org/10.1002/ange.202001608.

(74) *Materials Data on Ag3P by Materials Project*; mp-985295; Lawrence Berkeley National Lab. (LBNL), Berkeley, CA (United States). LBNL Materials Project, 2020. https://doi.org/10.17188/1272829.

(75) Shen, Y.; Roberge, A.; Tan, R.; Gee, M. Y.; Gary, D. C.; Huang, Y.; Blom, D. A.; Benicewicz, B. C.; Cossairt, B. M.; Greytak, A. B. Gel Permeation Chromatography as a Multifunctional Processor for Nanocrystal Purification and On-Column Ligand Exchange Chemistry. *Chem. Sci.* **2016**, *7* (9), 5671–5679. https://doi.org/10.1039/C6SC01301E.

VITA

Forrest Eagle was born in 1994 to Penny Benavidez and Hunter Eagle.

After high school, Forrest headed to Durango, Colorado where he attended Fort Lewis College from 2013-2017. Research at Fort Lewis College, Forrest studied with Professor Michael Grubb, exploring ways to show the similarities between quantum mechanics and large scale phenomena using sound.

As a graduate student, Forrest had the pleasure of presenting his work at multiple conferences, including: ACS National Meeting, MRS Meeting, and multiple UW-MRSEC meetings. Outside of lab, Forrest enjoys spending time with his wife and dog hiking and backpacking around the great state of Washington. He also enjoys playing board games and finding delicious breweries throughout the Seattle area.

Forrest is the first in his family to receive a PhD.